

OPTICAL REMOTE SENSING FOR MONITORING EVOLUTION OF ABLATION
SEASON MOUNTAIN SNOW COVER

by

Derrick J. Lampkin

Copyright © Derrick Julius Lampkin 2005

A Dissertation Submitted to the Faculty of
DEPARTMENT OF GEOGRAPHY AND REGIONAL DEVELOPMENT

In Partial Fulfillment of the Requirements
For the Degree of

DOCTOR OF PHILOSOPHY

In the Graduate College
THE UNIVERSITY OF ARIZONA

2005

THE UNIVERSITY OF ARIZONA
GRADUATE COLLEGE

As members of the Dissertation Committee, we certify that we have read the dissertation prepared by Derrick J. Lampkin

entitled OPTICAL REMOTE SENSING FOR MONITORING EVOLUTION OF ABLATION SEASON MOUNTAIN SNOW COVER

and recommend that it be accepted as fulfilling the dissertation requirement for the degree of: Doctor of Philosophy

Stephen R. Yool _____ Date: April 15, 2005

Andrew C. Comrie _____ Date: April 15, 2005

Anne Nolin _____ Date: April 15, 2005

Stuart E. Marsh _____ Date: April 15, 2005

Final approval and acceptance of this dissertation is contingent upon the candidate's submission of the final copies of the dissertation to the Graduate College.

I hereby certify that I have read this dissertation prepared under my direction and recommend that it be accepted as fulfilling the dissertation requirement.

Stephen R. Yool _____ April 15, 2005
Dissertation Director: Date

STATEMENT BY AUTHOR

This dissertation has been submitted in partial fulfillment of requirements for an advanced degree at the University of Arizona and is deposited in the University Library to be made available to borrowers under rules of the Library.

Brief quotations from this dissertation are allowable without special permission, provided that accurate acknowledgement of source is made. Requests for permission for extended quotation from or reproduction of this manuscript in whole or in part may be granted by the copyright holder.

SIGNED: Derrick J. Lampkin

ACKNOWLEDGEMENTS

The *Taittiriya Upanishad* (verse 3) asks what is education and replies that it is teacher speaking to the disciple seated by his side, wisdom between, discourse connecting them. This characterizes my relationship with my advisor Steve Yool, who I admire as a scholar and a human being. I would like to thank my entire dissertation committee as well. Their wisdom, knowledge and guidance were instrumental in not only the production of this work, but in the scholar I have become. I would like to specifically acknowledge Dr. Anne Nolin for her contribution. Her time, guidance, and unselfish willingness to share knowledge were vital. I'd like to thank Dr. Kurt Thome for his willingness to serve as a model mentor as well as his unselfish support. Hopefully, our dialogues have resulted in an increase in brain mass (and intelligence)! Additionally, I want to recognize Dr. Stuart Marsh and Dr. Comrie for their kindness and guidance.

I would like to extend my deepest gratitude to my family. My mother and grandmother, whose love and faith carried me through the rough seas. My love and thanks to Karen and Spencer McBroom. Spencer you were the best father anyone could ever desire. Karen, your love and dedication kept me balanced. Thanks to Dr. Kathy Powers (and Family), for your love and support over the years, which has been a light and crucial to reaching my goals. Her conviction, heart, and spirit are truly extraordinary. I'd like to extend a heartfelt thanks to Mike Malcomb, Ian Blount, Debbie Ng, Marty Gooden, and Jamil Hassan. Their friendship, love, and support over these long years have been invaluable and kept me focused and determined. Thanks to Dr. Katherine Tate and Larry Williamson for their support. A special thanks to Dr. Bisher Imam, whose steadfast support and friendship served a critical role in my career development. He is more than a mentor, but a brother as well. Thanks to Dr. Steven (Foz) Fassnacht for access to his wonderful, vast, and peculiar intellect. Dr. Kenneth Jezek is deserving of my gratitude for his efforts early in my career. Thanks to Dr. Robert (Bert) Davis, for his insightful input, Dr. Kelly Elder for his time and support, Rick Forster for his guidance, and Dr. Alfredo Huete. A special thanks goes to Dr. Jeff Dozier for his intellectual input and for doing some kick-ass work in alpine snow remote sensing. A special thanks goes to Gabriel Lopez for putting up with my demands. Thanks to Ceretha McKenzie, Ray Brice, Andree Jacobsen, and Jim Broermann for their technical support and friendship. A special thanks to Kevin (Scooter) Dressler, and Noah Molotch for their friendship and support. My knowledge of field snow hydrology was greatly enhanced by Noah. My faith in humanity was rekindled by my friendship with Scooter. Thanks to Dr. Chris Cattrall for your time, friendship, late night talks, and deep talks over lunch at the Frogg. I'd like to thank Sean Helfrich, Eve Halper, and Dawn Wilson. Lastly, I'd like to thank Dr. Roger Bales, and Soroosh Sorooshian, and Dr. Ming Ying Wei for their guidance. This research was supported by NASA under the Earth System Science Fellowship (ESS) grant NGT5. Additional thanks to the Department of Geography and Regional Development as well as the NASA Southwest Regional Earth Science Applications Center, (NASA NAG13-99005), NASA grants NAG5-8503 and NAG-3006 (Subcontract 300623).

DEDICATION

“Such is the temple, the royal temple, which encloses the places where the whole is taught in the part, and the particular in the whole...” This quotation regarding the ancient Egyptian concept of the university personifies the profound nature of such institutions. This work is dedicated to these places, which are committed to the pursuit of knowledge and truth; essential and intrinsic characteristics of the Creator.

TABLE OF CONTENTS

LIST OF FIGURES.....	8
LIST OF TABLES.....	9
ABSTRACT	10
I. INTRODUCTION	12
1.1 Research Problem and Context.....	12
1.2 Justification for Remote Sensing Technology to Monitor Mountain Snow Melt.....	18
II. THEORETICAL BASIS FOR USE OF SURFACE OPTICAL AND THERMAL PROPERTIES FOR TRACKING MOUNTAIN SNOW MELT.....	26
2.1 Surface Optical and Thermal Properties of Snow and the Snowmelt Process.....	26
2.2 Snow Surface Optical Properties and Energy Balance Process during Melting.....	30
III. DISSERTATION FORMAT.....	34
IV. PRESENT STUDY.....	35
4.1 Requirements for Characterizing Snow Pack Melt Dynamics using Remotely- Sensed Data.....	35
4.2 Numerical Simulations of MODIS Sensitivity Potential for Assessing Near Surface Mountain Snow Melt.....	37
4.3 Monitoring Mountain Snow Pack Evolution Using Near Surface Optical and Thermal Properties.....	38
4.4 Tracking Phases of Coupling between Snow Surface Optical and Thermal Properties with Melt Discharge during the Ablation Season.....	40
V. REFERENCES.....	44
APPENDIX A – Requirements for Characterizing Snow Pack Melt Dynamics using Remotely-Sensed Data.....	50
Abstract.....	52
Introduction.....	54
Ground and Model based Methods for Assessing Snowmelt.....	60
Satellite Systems for Monitoring Snowmelt.....	62
Theoretical Basis for NSMI.....	71
References.....	79

TABLE OF CONTENTS - *Continued*

APPENDIX B - Numerical Simulations of MODIS Sensitivity Potential for Assessing Near Surface Mountain Snow Melt	86
Glossary of Symbols.....	88
Abstract.....	89
Introduction.....	90
Background.....	91
Theory and Model.....	95
Methods.....	99
Results and Discussion.....	105
Conclusions and Recommendations.....	121
Acknowledgements.....	122
References.....	123
APPENDIX C - Monitoring Mountain Snow Pack Evolution Using Near Surface Optical and Thermal Properties	128
Abstract.....	130
Introduction.....	132
Background.....	134
Theory and Model.....	137
Methods.....	147
Results and Discussion.....	151
Conclusions and Recommendations.....	159
Acknowledgements.....	160
References.....	161
APPENDIX D – Tracking Phases of Coupling between Snow Surface Optical and Thermal Properties with Melt Discharge during the Ablation Season.....	165
Abstract.....	167
Introduction.....	169
Snowmelt Process and Surface Albedo.....	170
Data and Methods.....	171
Results.....	182
Discussion.....	203
Summary and Recommendations.....	211
Acknowledgements.....	212
References.....	213
Appendix A: Location of Ground Spectra Samples.....	218
Appendix B: Stratigraphy Plates.....	224

LIST OF FIGURES

Figure 1: Projected changes in stream flow timing as a function of snowmelt discharge timing for the end of the 21 st century (2080-2099).....	13
Figure 2: Linear trends in snow water equivalent (SWE) on April 1 over study period from 1950-2000.....	15
Figure 3: Theoretical near surface moisture index (NSMI) feature space for tracking snow pack evolution during the melt season using surface temperature and an optical-derived index sensitive to snow grain radius.....	24
Figure 4: Graphic illustrating two field methods used in this analysis, emphasizing the trade-off between snow surface spectral information and temporal information.....	41

LIST OF TABLES

Table I. Primary Requirements for Successful Application of NSMI Approach.....	23
---	----

ABSTRACT

The investigations contained in this body of work detail a viable proof-of-concept model for monitoring seasonal snow pack propensity for melt release based on time-variant snow surface optical and thermal properties. The model has been called the Near Surface Moisture Index- (Snow) (NSMI). The NSMI was developed based on time-variant snow surface optical and thermal properties. This research achieved three primary objectives: 1).development of theoretical foundation and surface moisture sensitive algorithm used to track both surface melt and pack discharge potential; 2.) time-dependent phases of coupling and decoupling between snow surface properties and melt discharge were characterized through analysis of long-term surface and sub-surface state variables; 3.) and sensitivity of optical satellite systems specifically, *EOS TERRA-MODIS*, to melting were was examined through radiative transfer simulations. Simulated at-sensor radiance was produced for various grain size changes to determine MODIS capacity to track melt onset. MODIS wavelengths greater than 667nm were sensitive to large changes in grain sizes, particularly bands with coarse spatial resolution (1000m). Longer wavelengths showed greater sensitivity to small changes in smaller grains than to small changes in larger grains. Shorter wavelengths at 500m spatial resolution appeared less effective overall for monitoring changes in grain size. NMSI feature space using Normalized Difference Snow Index (NDSI) on the abscissa and brightness temperature (T_b) on the ordinate was simulated. Simulated NDSI as a function of grain radius saturated approximately around 400-450 μ m. ASTER derived NSMI demonstrated behavior consistent with simulations with deviations due to topography, vegetation, and regional heterogeneity. We examined NSMI performance during an entire melt season through

tracking phases of coupling between snow surface properties and propensity for melt using two ground-base approaches; one with higher snow surface spectral information and low temporal resolution, the other with high temporal resolution and coarse spectral information. Phases of decoupling exhibited within ground-based time varying simulated NSMI were regulated by the temporal resolution specified to construct the feature space. Coarser temporal intervals on surface optical/thermal variables correlated the NSMI feature space various components of surface radiative variability. Coarser temporal optical and thermal resolution will tend to reduce variability within the NSMI feature space due to specific snowfall events.

1. INTRODUCTION

1.1 Research Problem and Context

Variability within the cryosphere, particularly under potentially rapid changes in the climate system, has important implications for terrestrial system response to anthropogenic forcing. Generally, snow cover is a critical factor in the earth's climatic energy and hydrologic budget. In many regions, it may play an influential role in determining the magnitude of any human-induced climatic change (Robinson, 1995). More specifically, variability in seasonal snow cover as a component of the cryosphere has important implications for not only climate system response but water resources vital to humans. Seasonal snow cover comprises approximately 30% of the Earth's land surface, while 10% is perennial cover by glaciers (Dozier, 1989). This distribution can be radically reconfigured if rapid changes in the climate system begin to manifest.

Specifically for snowmelt dominated rivers in the North American West, spring and summer runoff is the largest contribution to annual flow, comprising 50-80% of the total, and is in danger of significant shifts in timing (Dettinger and Cayan, 1995; Cayan et al., 2001; Stewart et al., 2004). A majority of rivers in western North America have exhibited trends toward earlier snowmelt timing during the last half century (1948-2000) (Stewart et al., 2004). The trend towards earlier melt is most prevalent in the Pacific Northwest, Rocky Mountain, Canadian, and Alaskan regions. The changes are driven primarily by broad scale warming trends and regional scale moistening (northwestern North America) and drying (southwestern North America), with temperature increases as

more dominant than the volume of precipitation (Stewart et al., 2004). Projections for snowmelt timing at the end of the 21st century indicate very dramatic changes relative to the 1948-2000 time interval where shifts of 30 to 40 days are predicted for the Pacific Northwest, Sierra Nevada, and Rocky Mountain basins (figure 1) (Stewart et al., 2004).

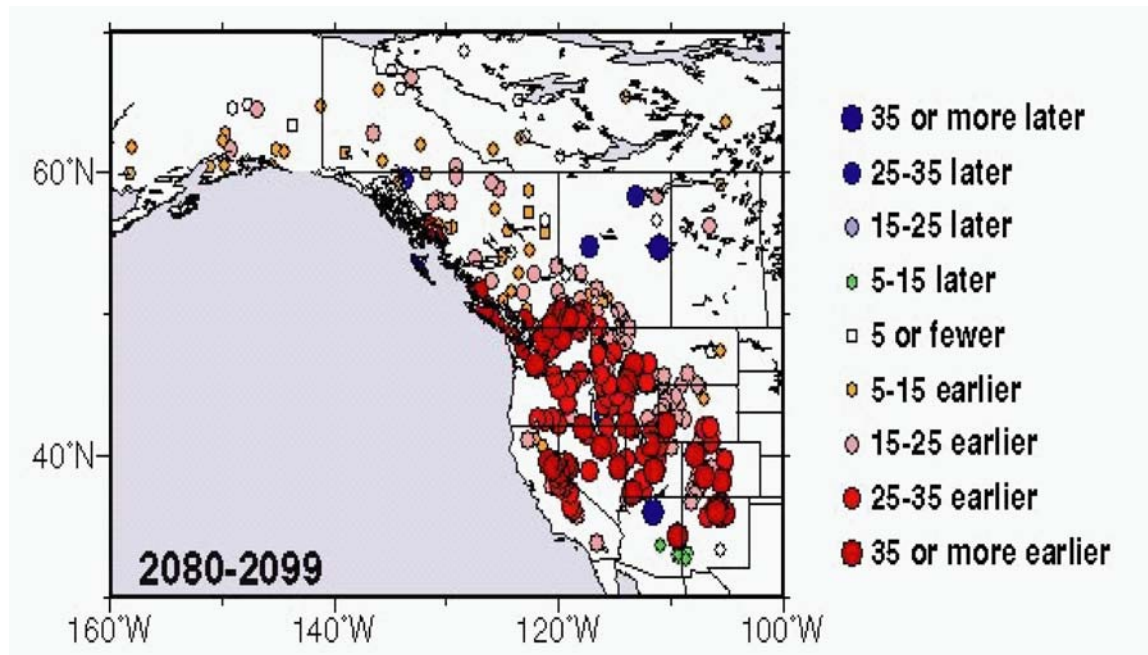


Figure 1: Projected changes in stream flow timing as a function of snowmelt discharge timing for the end of the 21st century (2080-2099). Values indicate difference in timing between (2080-2099) and (1951-1980). Figure was taken from Stewart et al., 2004.

Decreasing trends in snow cover across the western US were substantiated further by Mote (2003), through examination of ground-based measurements of snow water equivalent (SWE) at historical snow course sites from 1950-2000. Figure 2 illustrates large decreasing linear trends in SWE during this time interval across much of the western US, with larger decreases occurring in the Pacific Northwest, upper Sierra

Nevada, and Upper Rocky Mountains. Mote (2003) focused in the Pacific Northwest and has surmised that increases in temperature play a substantial role in SWE trends, but that variations in the role precipitation plays is also a function of elevation.

Large scale atmosphere processes are known to be influence the extent of snow cover, amount of accumulated water, and timing of melt throughout the Western US.

Atmospheric processes control in the condition of the snowpack through two primary factors; Precipitation and Temperature. Both are linked in their impact on snow cover characteristics as it varies temporally and spatially. The magnitude of their effects can vary dramatically as a function of regional heterogeneity expressed through provincial differences in topography, climatology, and location (latitude). In particular, for most regions in the Western US, anomalous snow accumulation is affected most by fluctuation in

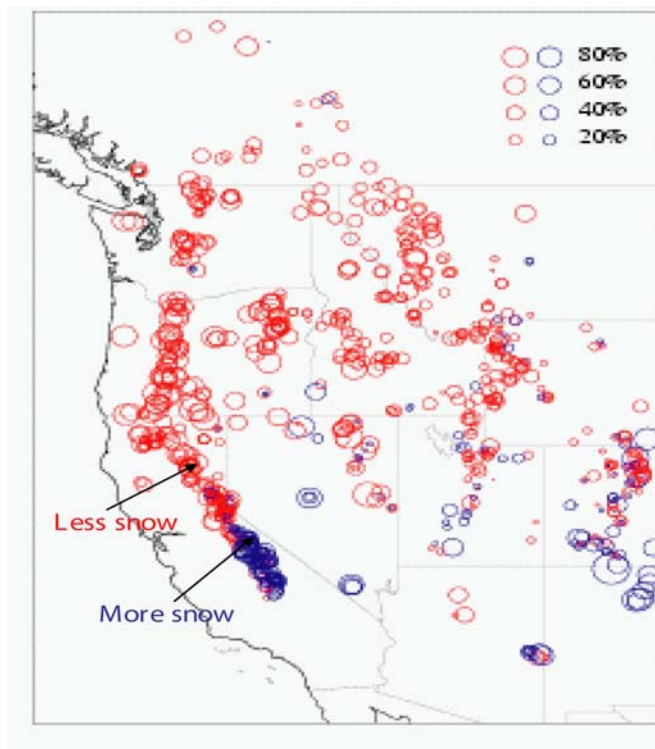


Figure 2: Linear trends in snow water equivalent (SWE) on April 1 over study period from 1950-2000. Negative trends are shown as red circles and positive in blue. The magnitude of trend is indicated by the area of the circle (Mote, 2003).

precipitation-winter and early spring precipitation anomalies extend over broad regional scales. Conversely, the regional impact of temperature is weak, but can vary depending on topography and season (Cayan, 1996). Temperature effects operate both during and after snow deposition: Temperature mediates the partition of snow versus rain that falls and can determine the amount of snow that is melted after deposition (Cayan, 1996). The relative importance of precipitation and temperature on snow cover is heavily contingent by elevation. The impact of the temperature signal at higher elevations is reduced, except during the spring when the mean temperature is warmer. This is not the case in regions characterized by lower elevations. In these zones, temperature is especially influential, particularly near the snowline. It seems that at higher elevations, more precipitation is

partitioned into snow and can accumulate. The amount of accumulation in these regions becomes more a function of precipitation than temperature. At lower elevations, temperature can become more influential since there is greater variability in precipitation partitioning between snow and rain. This is particularly evident in the coastal Pacific Northwest (Cascades of Oregon and Washington, where snow course elevations are generally lower than 2200m, the amount of April 1 snowpack is strongly influenced by winter and spring temperatures but is not so dependent upon precipitation (Cayan, 1996). Serreze et al., (1999) used data from the SNOTEL network to examine SWE variability across the Western US from 1963 through 1996. Subjective regions were delineated, partly based on Cayan (1996). Monthly precipitation for the Pacific Northwest peaks in November and decreases thereafter. Autumn temperatures are well above freezing, implying that early-season snowfall events tend to be offset by melt events and particularly, in October precipitation often falls as rain, delaying the seasonal rise in SWE (Serreze et al., 1999). Decreasing snow course trends in the Rockies indicate strong correlation with precipitation, where temperature is less important (Mote, 2003). Generally, the influence of temperature on the timing of snowmelt appears to vary as a function of latitude, where northern basins are more resistant to temperature fluctuations, because they are relatively cooler than southern basins that hover nearer the freezing point (Stewart et al., 2004).

Regional trends in snowmelt timing based on previous research are compelling, but lack comprehensive characterization of changes as a function of scale. Mote (2003) highlights this point by enumerating other factors that influence interpretation of inter-

annual correlations between SWE and climate trends, such as changes in land cover, wind speed and direction, topography, and even air pollution (affecting lowland precipitation more than high elevation mountain precipitation). These factors are indicative of the importance of scale. A more spatially coherent assessment of snow pack melt timing could shed light on whether or not observed changes in SWE (derived from snow course or automated SNOTel instruments) are indicative of global warming or natural (local) variability. It is essential that accurate information on the temporal and **spatial** dimensions of snow cover be available (Robinson, 1995). Advances in the capabilities of satellite remote sensing platforms in their ability to resolve greater spatial detail and discrimination between various land cover features, makes them well suited for the extraction and monitoring of snow cover conditions, particularly improved spatial characterization of snow melt onset, magnitude, and duration.

In most alpine terrain dominated by snow cover, a transition occurs between winter accumulation and spring melt season. During this transition period, the nature of snow cover changes and snowmelt runoff begins. Increased energy input to the snow surface and consequently availability of melt water initiate these changes. As liquid water enters the snowpack, processes collectively known as ripening, aging or melt metamorphism ensue (Kattelmann and Dozier, 1999). This process includes grain growth and rounding, ice-layer formation, warming of the snow to the melting temperature, densification, capillary retention of liquid water and creation of a flow network (Kattelmann and Dozier, 1999). This process characterizes the ‘evolution’ or ‘state’ of the snowpack in this analysis. This investigation is concerned with determining

if moderate scale remote sensing systems can be used to track the spatial and temporal variation of mountain snow pack evolution under the rubric of regional climate variability.

1.2 Justification for Remote Sensing Technology to Monitor Mountain Snow Melt

There are a number of methods for the acquisition of snow cover information. These methods include the use of field-based approaches, such as snow course traverses, point measurements derived from manual data collection to automated facilities such as snow telemetry (SNOTel) stations. Monitoring of the snowmelt process and the release of water from an alpine snow pack, specifically, requires tracking several factors that characterize changes in the energy balance or heat budget of a snow pack. Ground-based data derived from point measured automated meteorological instruments are widely used in the computation of snowmelt from a watershed either using a physical energy balance or index approach. A physical energy balance technique requires information on radiation energy, sensible and latent heat, energy transferred through rainfall over snow and heat conduction from ground to the snow pack as input into models that simulate the melt process through well understood physics. Snowmelt modeling techniques can be very useful but are limited in representation of spatially distributed melt dynamics across large basins. Models require ground-based measurements as input derived from automated meteorological stations that do not sufficiently capture the greater spatially variability of the melt process in heavily heterogeneous, rugged terrain. Explicit treatment of scale effects in spatially distributed snowmelt models also poses significant

limitations as well. The use of ground-based measurements suffers from a myriad number of limitations. Usually ground measurements have to be interpolated in order to produce spatially distributed information. The interpolation process introduces serious errors. These errors are a result of the failure to adequately capture the spatial variability of a particular variable.

Remote acquisition of snow properties has been employed over the last 50 years, spanning the use of high altitude land photography to aircraft and satellite systems. In the last 25 years, the use of space based remote sensors for acquiring snow cover information has been widely employed. Remote sensing technology offers improved distributed hydrologic information across a range of scales over remote regions that are inaccessible or where gauging stations are sparse or nonexistent (Solberg et. al., 1997). The continuous spatial and temporal acquisition of satellite data spanning the solar reflective visible (0.4-0.7 μ m), Near Infrared (NIR) (0.7-1.3 μ m), Shortwave Infrared (SWIR) (1.3-3 μ m), thermal infrared (3-14 μ m) and microwave (0.3-300 GHz) (active and passive systems) regions of the electromagnetic spectrum, to monitor snow cover properties has been successfully demonstrated (Dozier, 1989; Nolin and Dozier, 2000; Kuittinen, 1992; Solberg et. al., 1997; Koskinen et. al., 1999; Piesbergen et. al., 1995; Nagler et. al., 1998 and many others). In the microwave region of the electromagnetic spectrum during the melt process, active systems register attenuation of radar return when snow is wet because of the impact liquid water has on incident microwave energy. The presence of liquid water increases the imaginary part of the dielectric constant for snow cover (Ulaby et. al, 1982). This response is due to increase microwave energy absorption, which effectively reduces the radar backscatter signal (Ulaby et. al., 1982). This makes active

radar useful for monitoring snowmelt. The use of any particular remote sensing system for monitoring mountain snow melt dynamics requires considering relative advantages and disadvantages based on radiometric, spatial, and temporal resolutions as well as data volume provided by systems operating in the various segments of the EM spectrum. Passive and active microwave systems provide significant sensitivity to the onset of surface melt as well as the capacity for all-weather acquisitions. Capabilities provided by microwave systems provide complete un-obscured spatial coverage day and night. The spatial resolution of active systems such as synthetic aperture radar (SAR) systems such as ERS-1/2 (30m) and RADARSAT (10-100m) are sufficiently high for monitoring mountain snow melt. Temporal resolutions (repeat acquisition time intervals) for active systems can be as coarse as 24 days, increasing the likelihood of under sampling significant melt events. Active microwave systems possess adequate radiometric sensitivity to melt onset, and also provide high temporal resolution data (daily) during cloudy days, day or not. The primary disadvantage of passive systems is their coarse spatial resolution, which can be as coarse as $\sim 25\text{km}^2$ for the Special Sensor Microwave Imager (SSM/I) and as low as 10 km^2 for AQUA AMSR-E. Such coarse spatial resolutions make these systems well suited for large-scale basin studies (Schultz and Engman, 2000). Additionally, heterogeneity of surface features and snow cover properties within the passive microwave footprint results in a mixed signature, which is ultimately represented by a single brightness temperature that is a weighted areal average of surface emission from each surface type (Schultz and Engman, 2000).

Satellite systems operating in the solar reflective and thermal regions of the electromagnetic spectrum offer significant advantages for tracking mountain snow melt

dynamics. These systems span a wide range in spatial resolutions from sub-meter to tens of kilometers. Sensors with bands in the shortwave infrared region are very sensitive to the onset of snow surface melt. The temporal resolutions of these systems can be very high, with some collecting repeat measurements multiple times daily (with multiple redundant systems operating simultaneously such as the NOAA-N series platforms carrying the Advanced Very High Resolution Radiometer (AVHRR)). Solar reflective and thermal systems suffer from the influence of sub-pixel heterogeneity, but the relative higher spatial resolutions such systems operate over can tend to reduce the degree of within-pixel variability, which makes possible the application of algorithms designed to resolve sub-pixel constituents through spectral un-mixing routines.

Moderate resolution sensors (spatial resolutions between 250m and 8km) collecting in the solar reflective and thermal regions of the EM spectrum have been in operation since the early 1980s providing global products at spatial resolutions between 250m to 8km. The Advanced Very High Resolution radiometer (AVHRR), part of the NOAA series platforms, has provided a vital record of the earth surface dynamics during this period (Townshend and Justice, 2002). The launch of the Earth Observing System (EOS) Moderate Resolution Imaging Radiometer (MODIS) aboard the TERRA and AQUA platforms has served the land remote sensing community since 2000 and 2002, respectively. The future Visible and Infrared Imaging Suite (VIIRS) aboard the National Polar-orbiting Operational Satellite System (NPOESS) and the forthcoming NPOESS Preparatory Program (NPP) will provide improved capabilities for land surface satellite remote sensing as a critical and advanced follow-up to the AVHRR and MODIS satellite systems (Townshend and Justice, 2002). The emergence of the VIIRS system, which will

most resemble the capabilities of the MODIS system, will take place in stages with commensurate morning (9:30am) and afternoon (13:30pm) equatorial crossing time (ECT) (ascending node) as the AVHRR and MODIS systems, which current operate at 10:30am and 13:30pm ECT. The use of integrated satellite data records from these three systems (AVHRR, MODIS, and VIIRS) would provide a wealth of information about snow dynamics spanning from the early-late 1980s through the life of the VIIRS systems projected to operate aboard the final NPOESS system through 2012. This approximate 25-30 year satellite record could provide great insight into the annual and inter-annual variability of snow cover properties. The potential for surprising insights and new revelations about the spatial variability of snow cover properties can certainly be useful today and on an annual basis to users such as watershed managers and climate forecast scientists. In the long-term, the mining of such a data records for monitoring snow cover properties could really be the beginning of our understanding of long-term changes in snow dominated, alpine systems.

The investigations contained in this body of work detail a viable proof-of-concept model for monitoring seasonal snow pack propensity for melt release based on time-variant snow surface optical and thermal properties. The model has been called the Near Surface Moisture Index- (Snow) (NSMI) and is based on the surface moisture index (SMI), developed by Nemani et al. (1993). NSMI provides an estimate of relative wetness of features within a remotely sensed image. Figure 3 illustrates a conceptual NSMI feature space, when populated with time-variant measures of optical and thermal snow surface properties, theoretically maps the snow pack in transition from isothermal conditions through vigorous melt production periods of the ablation season. A relatively

dry snow pack occupies the lower right corner of the optical/thermal feature space, corresponding to relatively high NDSI values and low surface temperatures. This region is dynamic and should in theory change as the snow pack evolves through the warming phase to a period when the pack becomes isothermal and begins to release melt water.

Several important considerations must be addressed to render such an approach robust enough for operation application to data derived from an extensive time series of moderate resolution sensors (Table I).

Table I. Primary Requirements for Successful Application of NSMI Approach

Snow surface optical and thermal information should index the internal energy state of the snow pack as the system receives energy and produce melt
Snow surface characteristics should be highly coupled to the internal state of the snow pack during the entire ablation season
Moderate scale optical/thermal satellite systems should be sensitive enough to changes in at-satellite signals associated with changes in snow surface reflectance due to changes in snow pack energy balance associated with melt production and discharge
Adequate treatment of mix pixel problem through use of sub-pixel snow cover extent as initial requirement for application of NSMI
Reduction of spectral contribution of alpine vegetation to total at-sensor signal from heterogeneous snow dominated terrain

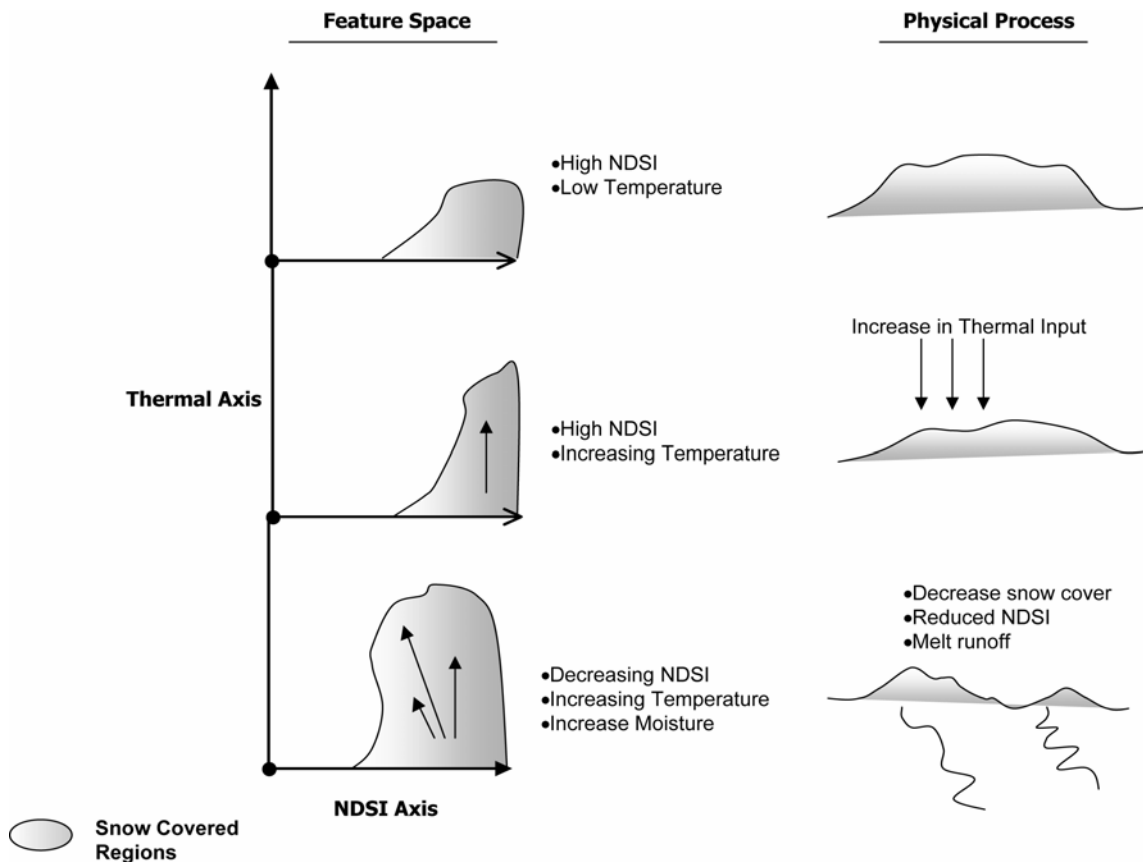


Figure 3: Theoretical near surface moisture index (NSMI) feature space for tracking snow pack evolution during the melt season using surface temperature and an optical-derived index sensitive to snow grain radius.

Core requirements were addressed in this dissertation through the following work; 1.) development of theoretical foundation and surface moisture sensitive algorithm from snow surface optical/thermal information to track both surface melt and pack discharge potential; 2.) investigate time-dependent phases of coupling and decoupling between snow surface properties and melt discharge through analysis of long-term surface and sub-surface state variables collected from an automated system during an entire melt season; and 3.) examine sensitivity of optical satellite systems specifically, *EOS TERRA-MODIS*, to melting were examined through radiative transfer simulations of snow

surface reflectance as a function of changes in snow grain size, associated with critical surface and sub-surface changes indicative of an evolving snow pack.

II. THEORETICAL BASIS FOR USE OF SURFACE OPTICAL AND THERMAL PROPERTIES FOR TRACKING MOUNTAIN SNOW MELT

2.1 *Surface Optical and Thermal Properties of Snow and the Snowmelt Process*

The albedo of snow, which affects snow pack energy balance, is a function of grain-size. The distribution of liquid water discharged from snow, which impacts the hydrology, is a function of the amount of melting (Green et al., 2002). Previous work has demonstrated that snow spectral reflectance is a strong function of grain-size and could be modeled from the optical properties of ice (Bohren and Barkstrom, 1974; Wiscombe and Warren, 1980; Warren, 1982; Dozier, 1989; Nolin and Dozier, 1993, Nolin and Dozier, 2000; Painter et al., 2003). The optical (wavelengths (λ)) spanning the solar reflective visible (0.4-0.7 μm), Near Infrared (NIR) (0.7-1.3 μm), Shortwave Infrared (SWIR) (1.3-3 μm) properties of snow depend on the bulk optical characteristics and the geometry of the ice grains, liquid water inclusions, and solid and soluble impurities (Dozier, 1989). More specifically, in the visible and NIR regions of the electromagnetic spectrum (EM), the bulk radiative properties of ice and water are similar, so the reflectance and transmittance of the snow pack depend on wavelength variations of the refractive index of ice, grain radius distribution, depth, density, and the size and amount of impurities, whose refractive indices are significantly different from those of ice and water. The presence of liquid water in pore space between snow grains enhances energy transfer between grains, accelerating grain growth (Colbeck, 1982) and greatly

influencing snow reflectance. This affect is more pronounced in the NIR regions of the EM spectrum, primarily as a function of microstructural changes (Dozier, 1989). The complex refractive index of ice (ϵ), given by:

$$\epsilon + i \epsilon'' \quad [1]$$

where:

ϵ = real part of the refractive index

ϵ'' = imaginary part of refractive index

is the most important optical property of ice, which governs spectral variation in reflectance of snow in the visible, NIR, and SWIR regions of the EM spectrum.

Specifically, the absorption coefficient (κ_i), which is related to the imaginary component of the refractive index of ice by:

$$\kappa_i = 4\pi\epsilon''/\lambda \quad [2]$$

increases substantially for λ between 0.4 to 2.5 μm . Such an increase causes snow reflectance to substantially decrease as λ increases, indicative of greater absorption. The

melt process is characterized by a substantial decline in snow reflectance. This process is accompanied by the production of melt and an increase in liquid water occupying ice pore spaces, yet it is not the presence of liquid water directly that produces the resultant decrease in reflectance. This decrease is primarily a function of an increase in the effective grain size, resulting from two- to four grain clusters that form during melt, which optically behave as a single large grain (Dozier, 1989). In wet snow with high liquid water content, smaller particles are at lower temperatures, and heat flow from large grains causes their melting and entrainment into larger particles (Colbeck, 1982). As grain radius increases (which can range from $\sim 50\mu\text{m}$ for new snow to $1\text{mm}+$ for old melting snow) an incident photon will have a high probability of being scattered when it transverses an air-ice interface, but a greater chance of absorption while passing through the ice grain. An increase in grain size causes an increase in the path length that must be traveled through the ice grain between scattering opportunities (Warren, 1982). The extended photon path length increases the amount of energy absorbed, resulting in a decline in reflectance.

Thermal radiation ($3.5\text{-}50\mu\text{m}$) is absorbed and emitted by the atmosphere without appreciable scattering (Marks and Dozier, 1992). Thermal remote sensing platforms operate over a more restricted range in the EM spectrum, with many systems operating in the atmospheric window between 8 and $14\mu\text{m}$. Snow cover melt dynamics in the thermal region of the EM spectrum are a function of incident radiation as well as surface longwave emission. The onset of melt is representative of a continuum within the snowpack. The pack is better characterized as an evolving medium, which initially

manifest microstructural changes indicative of metamorphic transitions. Surface and near surface segments of the snow pack are the primary interface through which energy enters the pack to drive these structural changes. Energy input in the form of solar radiation (addressed in the previous discussion) and thermal input derived from large diurnal variations in temperature are responsible for initial near surface changes. (Colbeck, 1989) examined the relative importance of solar insolation and diurnal temperature variation in the onset of rapidly crystal growth near the snow surface. Simulations in this analysis indicate that from the surface down to approximately 0.25m, grain growth would increase with increasing radiation input, but this process is pronounced due to strong diurnal air temperature fluctuations. These two processes induce strong temperature gradients within the uppermost regions of the snow pack, driving vapour flow and constructive grain metamorphism. Colbeck (1989) assumes that these two processes are more intense for high altitude snow cover at low latitudes with the most vigorous growth occurring within the upper 0.1m of the pack. Thermal exitance is a function of snow surface skin temperature and emissivity (Marks and Dozier, 1992). Dozier and Warren (1982) determine that thermal infrared emission does not depend on grain size, density, liquid water content, and impurities, but primarily on the viewing geometry. Snow highly approximates the behaviour of a blackbody with emissivities ranging between 0.985-0.990 and is relatively invariant to wavelength in the 8-14 μ m interval (Dozier and Warren, 1992). Marks et al. (1992) illustrated in the Sierra Nevada that near surface snow temperature tends to follow air temperature as a result of the surface layer establishing thermal equilibrium with the near surface atmosphere. Satellite derived surface temperatures can be useful in tracking changes in surface conditions that are

correlated with internal melt production. The use of snow surface reflectance alone would not suffice in this endeavour, primarily because substantial decreases in reflectance are not solely due grain enlargement resulting from melt onset. Impurities and litter on the snow surface can cause substantial reductions in reflectance (Warren, 1982). Snow surface temperature information coupled with optical information would assist in narrowing those surface conditions most indicative of an increase in energy input and melt production. Interestingly, a small amount of surface impurities has the most effect on reflectance mainly in visible wavelengths ($\lambda < 1\mu\text{m}$) (Warren, 1982). A decline in reflectance means an increase in absorption, therefore the presence of surface impurities may accelerate the melt process.

2.2 Snow Surface Optical Properties and Energy Balance Process during Melting

The energy balance equation is used to quantify snowmelt and applied to a control volume of snow, allows the fluxes of energy penetrating the snow surface and retained by the volume to be expressed as changes in internal energy (Shook and Gray, 1997).

Generally, the energy balance of a snow pack is expressed as

$$\Delta Q = S_{\text{net}} + H + L_v E + G + M \quad [3]$$

where ΔQ is change in snow pack energy, S_{net} , H , $L_v E$, G , and M are net radiation,

turbulent sensible, turbulent latent, conductive, and advective energy fluxes. When the pack is in temperature equilibrium ($\Delta Q = 0$) the resulting negative energy balance will cool the snow pack, increasing its cold content (the amount of energy required to bring it to 0°C).

$$C_c = -C_i \int \rho_s T dz \quad [4]$$

where ρ_s , C_i , T are density, specific heat of ice, and layer temperature respectively and integrated over depth (dz). Conversely, a positive energy balance will warm the snow pack. Energy input to the snow pack is initially partitioned into overcoming the ‘cold content’. Once the snow pack has become isothermal, additional energy goes towards solid to liquid phase change (positive ΔQ) and melt is produced. Melt conditions of an isothermal snow pack can be influenced by air temperatures above 0°C, which could produce precipitation input to the pack as rain adding energy through latent heat transfer. During periods of active melting net radiation and convective ($H + L_v E$) serve as dominant energy sources for melt production. Given the temperature of the pack changes little during this period, large changes in the internal state of the pack are mitigated by latent rather than sensible heat input ($L_v E$ rather than H) (Oke, 1987). If the air above the snow pack is warmer than the snow surface, the vapour pressure is higher in the air promoting an air-to surface vapour pressure gradient. The resultant downward turbulent flux of moisture and condensation would add energy to the snow surface given the latent heat of vaporization released during condensation (at 0°C) is 7.5 times higher than latent heat of fusion required for melting water (Oke, 1987). The primary source of energy during melt is net radiation. The net radiation term (S_{net}) in (1) can be decomposed into

the following shortwave (K) and longwave (L) flux components:

$$S_{\text{net}} = K\downarrow - K\uparrow + L\downarrow - L\uparrow = K_{\text{net}} + L_{\text{net}} \quad [5]$$

where the arrows denote incoming (\downarrow) and outgoing (\uparrow) energy (Oke, 1987). Given the significant contribution solar irradiance makes to the snowmelt process, snow pack reflectance and absorption characteristics, as a function of wavelength (λ), can influence the amount of solar radiation partitioned into energy for melt production. Incident photons that are not reflected from the snow pack will be absorbed in ice grains and converted to heat. Since the thermal diffusivity of snow is low, this heat energy will be retained at depth (Dozier et al, 1989). Asymmetry can occur between radiative cooling and appears to have warmed more rapidly than it cooled (Nolin, 1993). This process can result in subsurface heating and has been characterized as the “solid-state greenhouse effect”. Matson and Brown (1989) as well as Nolin (1993) have examined this phenomenon, which results from both rapid absorption of shortwave energy at depth with relatively little loss in energy through longwave (thermal) emission only from the surface of the snow pack. More energy is retained at depth resulting in the onset of melt near the surface although surface air temperatures may not exceed 0° C (Dozier et al., 1989). Energy available to drive this process is that not reflected (but absorbed) expressed as (Oke, 1987):

$$K_{\text{net}} = K\downarrow (1-\alpha) \quad [6]$$

where variation in surface albedo (α) can influence the amount of energy entering the pack for melt. Once the pack has become isothermal, additional energy, primarily controlled by this radiative process goes directly towards the production of melt. This process starts in the upper part of the pack and proceeds downward, initially producing intermittent melt. This melt infiltrates deeper into the pack and refreezes, adding latent heat to the pack at depth. As the melt season continues, this process becomes more pronounced, producing preferential flow paths for melt to exit the snow pack (Wakahama, 1965).

This dynamic link between surface radiative conditions and the pack's propensity for melt production and release is the primary mechanism the algorithm proposed in this analysis attempts to leverage.

III. DISSERTATION FORMAT

Two papers in this dissertation were peer-reviewed and published in special issues of *Geocarto International* and *Hydrological Processes*. The *Geocarto International* manuscript was included in the Association of American Geographer's Centennial issue. The *Hydrological Processes* manuscript appeared in a special issue dedicated to selected works presented in cryosphere monitoring poster and oral presentations at the Fall 2004 American Geophysical Union Conference. The first paper was structured as a review paper and is in preparation for submission to *Progress in Physical Geography*. The fourth paper in the dissertation was not published but is scheduled for submission to *Journal of Geophysical Research*. Both published manuscripts were co-authored with my advisor, Dr. Stephen Yool. Individuals who provided substantive input and support were recognized through acknowledgements. My contribution to these works involved analysis, data processing, simulations, computer programming, and field work. Improvements in the quality of the analysis, as well as organization of the paper were made through suggestion provided by my advisor, committee, as well as reviewers.

IV. PRESENT STUDY

The methods, results and conclusions of this study are presented in the papers appended to this dissertation. The following are the most important findings in these papers.

4.1 Requirements for Characterizing Snow Pack Melt Dynamics using Remotely-Sensed Data

Variability within the cryosphere has important implications for terrestrial system response to anthropogenic forcing. More specifically, variability in seasonal snow cover as a component of the cryosphere has important implications for not only climate system response but water resources vital to humans. A thorough understanding of various characteristics about alpine snow cover, such as density, depth, accumulation, and temporal variation in extent, are vital to the effective management of these resources. There are a number of methods for the acquisition of snow cover information. These methods include the use of field-based approaches, such as snow course traverses; point measurements derived from manual data collection to automated facilities such as snow telemetry (SNOTel) stations. The use of ground-based measurements suffers from a myriad number of limitations. Remote sensing technology offers the capacity to circumvent these limitations through improved distributed information across a range of scales over remote regions that are inaccessible or where gauging stations are sparse or nonexistent. Satellite systems operating in the solar reflective and thermal regions of the

electromagnetic spectrum over significant advantages for tracking mountain snow melt dynamics. These systems span a wide range in spatial resolutions from sub-meter to tens of kilometers. Sensors with bands in the shortwave infrared region are very sensitive to the onset of snow surface melt. A technique using snow surface optical and thermal information applied to moderate scale remote sensing systems have been proposed to map the spatial and temporal variability of snowmelt dynamics in mountain environments. Several important considerations must be addressed to render such an approach robust enough for operation application to data derived from an extensive time series of moderate resolution sensors. The core issues are:

- Can snow surface optical and thermal information really index the internal energy state of the snow pack as the system receives energy and produce melt?
- How well coupled are snow surface characteristics to the internal state of the snow pack during the entire ablation season?
- How sensitive are optical systems in tracking surface signals associated with snow pack melt discharge?

Addressing these issues formed the foundation of work to establish the Near Surface Moisture Index (NSMI) approach.

4.2 *Numerical Simulations of MODIS Sensitivity Potential for Assessing Near Surface Mountain Snow Melt*

Variations in amount of near surface snow melt produce changes in snow grain size. We evaluated Moderate Resolution Imaging Spectroradiometer (MODIS) visible and near-infrared band for monitoring snow pack ripeness using a Mie scattering model, coupled with a simple approach for computing directional hemispherical reflectance (albedo or total flux leaving surface divided by total irradiance). Results suggest MODIS visible and near-infrared bands may have the potential to detect changes in grain size as an indicator of mountain snow pack evolution during the melt season. Modeled at-sensor radiance was produced for grain size changes ranging from $10\mu\text{m}$ to $1000\mu\text{m}$.

Differences in simulated at-sensor radiance as a function of grain size, solar zenith angle, surface slope, and amount of diffuse irradiance were compared to band specific noise equivalent radiance (NEAL) thresholds. MODIS wavelengths greater than 667nm may be sensitive to large changes in grain sizes, particularly those bands with coarse spatial resolution (1000m). Longer wavelengths showed greater sensitivity to small changes in smaller grains than to small changes in larger grains. Shorter wavelengths with small fine spatial resolution (500m) appear less effective overall for monitoring changes in grain size. Variation in solar zenith angle has a greater impact on changes in larger grains (100-1000 μm) than smaller (10-100 μm). The overall magnitude of difference in modeled at-sensor radiance demonstrates that the affect of diffuse irradiance may not be substantial. Surface slope does not appreciably affect changes in model at-sensor

radiances for various grain sizes. This may not be true given the model does not account for snow BRDF.

4.3 Monitoring Mountain Snow Pack Evolution

Using Near Surface Optical and Thermal Properties

A Near Surface Moisture Index (NSMI), which models relative moisture through construction of a feature space using visible band and a thermal band was developed to track the evolution of spring snow melt potentially from MODIS. A simple analytical radiative transfer model for computing directional hemispherical reflectance and emissivity derived from the delta-Eddington approximation to the equation of radiative transfer was used to produce the NSMI. Modeled reflectance and emissivity, as a function of grain size, were used to produce the NMSI feature space constructed from the Normalized Difference Snow Index (NDSI) on the abscissa and brightness temperature (T_b) on the ordinate. As grain size increases, the dynamic range or sensitivity of NDSI is reduced, with saturation occurring approximately around 400-450 μm grain radius. T_b for various grain sizes at fixed kinetic temperatures between 245, and 273 Kelvin and NDSI as a function of grain size were used to construct simulated NSMI. Cold Land Processes Experiment (CLPX) field measurements of surface wetness, surface/near surface grain size, average pack temperature and surface temperature for late February and March in Fraser, Colorado were correlated with measured NSMI using a March 4, 2002 scene from Advanced Spaceborne Thermal Emission and Reflection Radiometer (ASTER) as validation of simulated NSMI. Ground-based measurements indicate significant changes

in snow surface properties, representing a warming pack across three ISA's from February to March. Similar behaviors are reflected in changes in average pack temperatures. Surface and average pack temperatures in March were warmer for all three sites, with the St. Louis ISA having the warmest temperatures, near 0° C. ASTER measured reflectance and surface brightness temperature (T_b) were sampled from each ISA and used to construct an NMSI. Lower elevation ISA (St. Louis Creek) demonstrated higher mean T_b and lower mean NDSI while the higher elevation ISA (Alpine) showed higher mean NDSI and lower mean T_b. ASTER derived NSMI demonstrated behavior consistent with simulations with deviations due to topography, vegetation, and regional heterogeneity.

4.4 *Tracking Phases of Coupling between Snow Surface Optical and Thermal Properties with Melt Discharge during the Ablation Season*

The potential for using optical satellites to track the evolution of alpine snow packs and monitor the timing of melt release is contingent on the strength of the relationship between near surface optical and thermal characteristics and the 'state' of the snow pack throughout the ablation season. Due to the difficulties in collecting continuous information about the relationship between surface optical/thermal dynamics with pack melt discharge during and entire melt season, tracking phases of coupling between snow surface properties and propensity for melt was examined through two ground-based approaches; one with higher snow surface spectral information and low temporal resolution, the other with high temporal resolution and coarse spectral information (Figure 4). A high resolution field spectrometer was used to collect snow surface spectral signatures as well as excavated snow pits at two sites (Berthoud Pass SNOTel Site and Robber's Roost Trailhead) near the Forest Service Fraser Experimental Research station in Fraser, Colorado during the period between March 22, 2004 and March 26, 2004. Archived data from the Mammoth Mountain Cooperative Snow Study Site (MMCS) in the eastern Sierra Nevada of California, spanning from April 1, 2002 through July 1, 2002, were used for its high temporal resolution throughout the 2002 ablation season. Data collected from the Fraser site and those derived from the MMCS data set were separated by space and time, but should be considered as a single observation in the attempt to monitor the snowmelt process. The logistics of

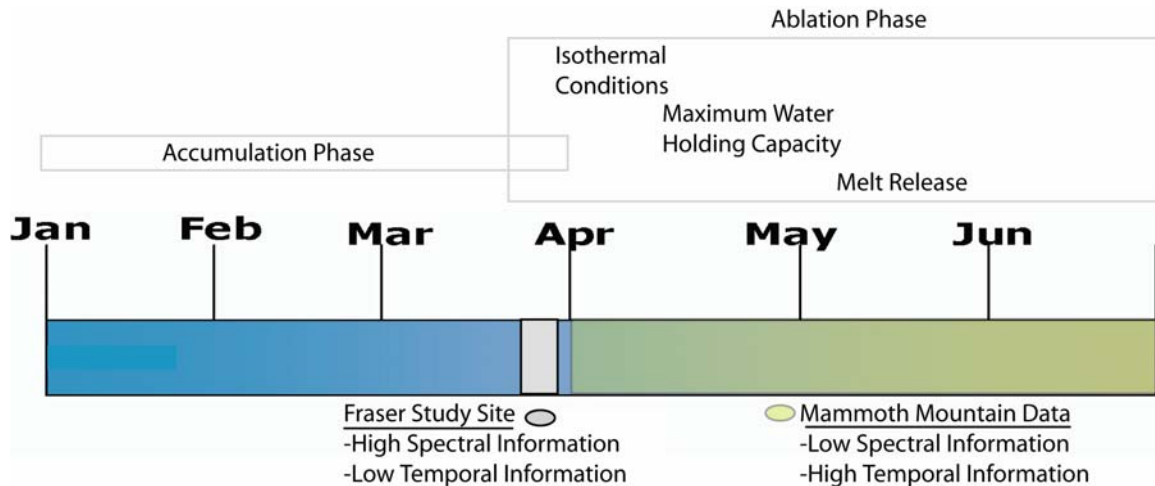


Figure 4: Graphic illustrating two field methods used in this analysis, emphasizing the trade-off between snow surface spectral information and temporal information.

Acquiring high spectral and stratigraphic resolution on daily time scale (at the Fraser data was collected) was not possible. MMCS data set provided a much longer temporal record, but at a cost. There was a substantial loss in spectral and stratigraphic detail, requiring the use of coarse snow surface albedo, and surface temperature to act as surrogates. Additionally, average pack temperature derived from the MMCS database was used as a surrogate of overall internal state of the snow pack. Ground-based snow surface spectra were acquired at two sites near Fraser, Colorado. Several spectra were acquired at each site per day. Average spectra were computed in addition to root mean square error for each daily acquisition. March 22nd and 25th demonstrate higher visible/NIR reflectance than the 23rd and 26th. The magnitude in visible/NIR reflectance as a function of time was not chronological. SWIR reflectances at S1 illustrate higher values on March 25 and similarly lower values for the remaining days. Site 2 (S2) generally displays characteristic spectra. Visible/NIR behaviour at S2 was more

complicated than at S1. Shorter wavelength ($\sim 400\text{nm}$) visible reflectance on March 22nd demonstrates the highest reflectance followed by the 26th, 25th, and 23rd. There was an inversion in reflectance at 446nm where March 26th and 25th values increase as wavelength increase. SWIR spectra demonstrate high values on March 25 followed by the 26th, 22nd, and 23rd (primarily around the 1030nm absorption feature). Longer wavelength spectra ($> 1500\text{nm}$) display characteristic low values with little distinction among spectra as a function of day. Stratigraphic data derived from snow pits excavated at each site per day, during the analysis period, demonstrates very dynamic conditions. Pits indicated well stratified packs with increasing presence of melt related structures appearing as the week advanced. Preferential flow path structures such as flow tubes and ice knobs were present. Excavated pits indicated packs that had fully reached isothermal conditions early in the week. Surface temperature, temperature at fixed depths, incoming and outgoing shortwave radiation ($0.285\text{-}2.8\mu\text{m}$), snow depth, and snow pack melt discharge were downloaded from the MMCS archive. These variables were downloaded for the ablation season of 2002 starting from April 1 to examine long-term coupling between surface characteristics and melt propensity. Time series analysis indicates periods of temporal coupling between surface albedo, discharge, and surface temperature and discharge. Increases in melt discharge were associated with decreases in albedo and increases in surface temperature. Cross-correlation analysis between albedo and discharge indicates lagged correlations that appear cyclic in nature. Cross-correlation strength between these two variables was strongest at (-1) day lag and was negative. Therefore, albedo leads in time over melt discharge. A similar result occurred in cross-correlation analysis between surface temperature and discharge. The difference in

surface temperature was positively correlated with discharge and lagged at (-1) day, indicating discharge response following a change in surface temperature. A time-dependent NSMI derived from the MMCS ground data, using albedo directly as a proxy for a snow grain size index and surface temperature. This time-dependent NSMI demonstrates a trajectory of the snow pack through optical/thermal feature space. As the ablation season advanced, points in the simulated NSMI tracked towards low albedo and increasing surface temperature. Several days did not follow this trajectory and were correlated with increases in snow depth, and decreases in surface temperature indicative of new snow fall events. These periods coincided with decreased coupling between the surface and melt discharge events. . Phases of decoupling exhibited within the MMCS-simulated NSMI were regulated by the temporal resolution (aggregation interval) specified to construct the feature space. Adjustments to the aggregation interval allow the NSMI feature space to be calibrated to various components of surface radiative variability. Greater aggregation (coarser temporal optical and thermal resolution) will tend to shift NSMI feature space correlation to melt discharge from specific snowfall events to inter-seasonal trends. Results from this work indicate that surface optical and thermal properties can be used within the NSMI framework to track occurrences of melt discharge throughout the entire melt season.

V. REFERENCES

Bohren, C.F., and B. R. Barkstrom. 1974. Theory of the optical properties of snow.

Journal of Geophysical Research, Volume 79, No. 30, 4527-4535.

Cayan, D.R. 1996. Interannual climate variability and snowpack in Western US. *Journal of Climate*, Volume 9, 928-951.

Cayan, D.R., S.A. Kammerdiener, M.D. Dettinger, J.M. Caprio, and D.H. Peterson. 2001. Changes in the onset of spring in the Western United States. *Bull. Amer. Meteorol. Soc.*, Volume 82, 399-415.

Colbeck, S.C. 1982. An overview of seasonal snow metamorphism. *Review of Geophysics and Space Physics*, Volume 20., No. 1, pp45-61.

Colbeck, S.C. 1989. Snow-crystal growth with varying surface temperatures and radiation penetration. *J. Glaciol.*, Volume 35, no. 119, pp 23-29.

Dettinger, M.D. and Cayan, D.R. 1995. Large-scale atmospheric forcing of recent trends toward early snowmelt runoff in California. *Journal of Climate*, Volume 8, 606-623.

Dozier, J. 1989. Spectral signature of alpine snow cover from the Landsat Thematic Mapper. *Remote Sens. Environ.*, 28, 9-22.

Dozier, J., and S.G. Warren. 1982. Effect of view angle on the infrared brightness temperature of snow. *Water Resources Research*, Volume 18, No. 5, 1424-1434.

Dozier, J., R.E. Davis, and A. Nolin. 1989. reflectance and transmittance of snow at high spectral resolution, in IGARSS '89, *Quantitative remote sensing: an economic tool for the Nineties*, Vancouver, Canada, 662-664, IGARSS '89 12th Canadian Symposium on Remote Sensing, No 89Ch2768-0.

Green, R.O., R.D. Roberts, and T. Painter. 2002. Spectral snow-reflectance models for grain-size and liquid water fraction in melting snow for the solar-reflected spectrum. *Annals of Glaciology*, Volume 34, 71-73.

Kattelman, R., and J. Dozier. 1999. Observations of snowpack ripening in the Sierra Nevada, California, USA. *Journal of Glaciology*, Volume 45, No. 151, 409-416.

Koskinen, J., S. Metsamaki, J. Grandell, S. Janne, L. Matikainen, and M. Hallikainen. 1999. Snow monitoring using radar and optical satellite data. *Remote Sens. Environ.*, vol (69), pp16-29.

Kuittinen, R. 1992. *Remote sensing for hydrology progress and prospects*, WMO Operational Hydrology Report, No 36, WMO-No. 773, WMO. Geneva, Switzerland.

Marks, D., and J. Dozier. 1992. Climate and energy exchange at the snow surface in the alpine region of the Sierra Nevada 2. Snow cover energy balance. *Water Resources Research*, Volume 28, No. 11, 3043-3054.

Marks, D., J. Dozier, and R.E. Davis. 1992. Climate and energy exchange at the snow surface in the alpine region of the Sierra Nevada 1. Meteorological measurements and monitoring. *Water Resources Research*. Volume 28, No. 11, 3029-3042.

Matson, D.L., and R.H. Brown. 1989. Solid-state greenhouses and their implications for icy satellites. *Icarus*, Volume 77, 67-81.

Mote, P.W. 2003. Trends in snow water equivalent in the Pacific Northwest and their climatic causes. *Geophysical Research Letters*, Volume 30, No. 12.
doi:10.1029/2003GL017258.

Nagler, T. and H. Rott. 1998. SAR tools for snowmelt modeling in the project HydAlp. In Proceedings of IEEE International Geoscience and Remote Sensing Symposium (IGARSS'98) Symposium, Seattle, WA, IEEE, New York.

Nemani, R. L. Pierce, S. Running, and S. Goward. 1993. Developing satellite-derived estimates of surface moisture status. *Journal of Applied Meteorology*. Volume 32, pp548-557.

Nolin, A., and J. Dozier. 1993. Estimating snow grain size using AVIRIS data. *Remote Sens. Environ.*, Volume 44, 231-238.

Nolin, A., and J. Dozier. 2000. A hyperspectral method for remote sensing of grain size of snow. *Remote Sens. Environ.*, Volume 74, 207-216.

Oke, T.R. 1987. *Boundary layer climates* 2nd edition. Routledge.

Painter, T.H., J. Dozier, D.A. Roberts, R.E. Davis, and R.O. Green. 2003. Retrieval of subpixel snow-covered area and grain size from imaging spectrometer data. *Remote Sens. Environ.*, Volume 85, 64-77.

Piesbergen, J., F. Holecz, and H. Haefner. 1995. Snow cover monitoring using multitemporal ERS-1 SAR data. In *Proceedings of IEEE International Geoscience and Remote Sensing Symposium (IGARSS'95)*, Florence, Italy, IEEE, New York, pp. 1750-1752.

Robinson, D.A. 1995. Decadal variations of snow cover in *Natural Climate Variability on Decade-to-Century Time Scales*, National Research Council, National Academy Press, Washington, DC, 60-66.

Schultz, G.A., E.T. Engman. 2000. *Remote Sensing in hydrology and water management*. Springer.

Serreze, M.C., M.P. Clark, and R.L. Armstrong. 1999. Characteristics of the western united states snowpack from snowpack telemetry (SNOTEL) data. *Water Resources Research*, Volume 35, No. 7, 2145-2160.

Shook, K., and D.M. Gray. 1997. Snowmelt resulting from advection. *Hydrological Processes*, Volume 11, 1725-1736.

Solberg, R. D. Hiltbrunner, J. Koskinen, T. Gunneriussen, K. Rautianen, M. Hallikainen. 1997. *Snow algorithms and products, SNOWTOOLS WP410*, Norwegian Computing Center, Report 924, Oslo, Norway, 112.

Stewart, I.T., D.R. Cayan, and M.D. Dettinger. 2004. Changes in snowmelt runoff timing in Western North America under a 'business as usual' climate change scenario. *Climate Change*, volume 62, 217-232.

Townshend, J.R.G., and C.O. Justice. 2002. Towards operational monitoring of terrestrial systems by moderate-resolution remote sensing. *Remote Sens. Environ.*, Volume 83, 351-359.

Ulaby, F.T., R.K. Moore, and A.K. Fung. 1982. *Microwave remote sensing: active and passive volume II, radar remote sensing and surface scattering and emission theory*. Addison-Wesley Publishing Company.

Wakahama, G. 1965. Metamorphisms of wet snow. *Low Temp. Sci., Ser. A*, Volume 23, 51-66.

Warren, S.G.1982. Optical properties of snow. *Rev Geophys. Space Phys.* 20:67-89.

Wiscombe, W.J., and Warren, S.G.1981. A model for the spectral albedo of snow I: Pure snow. *J. Atmos. Sci.*, 37:2712-2733.

Appendix A

**Requirements for Characterizing Snow Pack Melt Dynamics using Remotely-Sensed
Data**

REQUIREMENTS FOR CHARACTERIZING SNOW PACK MELT DYNAMICS
USING REMOTELY-SENSED DATA

D.J. Lampkin¹

¹Department of Geography, Pennsylvania State University, University Park, PA, USA

(unpublished)

ABSTRACT

Variability within the cryosphere has important implications for terrestrial system response to anthropogenic forcing. More specifically, variability in seasonal snow cover as a component of the cryosphere has important implications for not only climate system response but water resources vital to humans. A thorough understanding of various characteristics about alpine snow cover, such as density, depth, accumulation, and temporal variation in extent, are vital to the effective management of these resources. There are a number of methods for the acquisition of snow cover information. These methods include the use of field based approaches, such as snow course traverses, point measurements derived from manual data collection to automated facilities such as snow telemetry (SNOTel) stations. The use of ground based measurements suffers from a myriad number of limitations. Remote sensing technology offers the capacity to circumvent these limitations through improved distributed information across a range of scales over remote regions that are inaccessible or where gauging stations are sparse or nonexistent. Satellite systems operating in the solar reflective and thermal regions of the electromagnetic spectrum offer significant advantages for tracking mountain snow melt dynamics. These systems span a wide range in spatial resolutions from sub-meter to tens of kilometers. Sensors with bands in the shortwave infrared region are very sensitive to the onset of snow surface melt. A technique using snow surface optical and thermal information applied to moderate scale remote sensing systems have been proposed to map the spatial and temporal variability of snowmelt dynamics in mountain environments. Several important considerations must be addressed to render such an approach robust enough for operation application to data derived from an extensive time series of moderate resolution sensors. The core issues are:

- Can snow surface optical and thermal information really index the internal energy state of the snow pack as the system receives energy and produce melt?
- How well coupled are snow surface characteristics to the internal state of the snow pack during the entire ablation season?
- How sensitive are optical systems in tracking surface signals associated with snow pack melt discharge?

These issues form the foundation of work to establish the Near Surface Moisture Index (NSMI) approach.

1. INTRODUCTION

1.1 Research Problem and Context

Variability within the cryosphere, particularly under potentially rapid changes in the climate system, has important implications for terrestrial system response to anthropogenic forcing. Generally, snow cover is a critical factor in the earth's climatic energy and hydrologic budget. Snow cover may in many regions play an influential role in determining the magnitude of any human-induced climatic change (Robinson, 1995). More specifically, variability in seasonal snow cover as a component of the cryosphere has important implications for not only climate system response but also water resources vital to humans. Seasonal snow cover comprises approximately 30% of the Earth's land surface, while 10% is perennial cover by glaciers (Dozier, 1989). This distribution can be radically reconfigured if rapid changes in the climate system begin to manifest.

Specifically for snowmelt dominated rivers in the North American West, spring and summer runoff is the largest contribution to annual flow, comprising 50-80% of the total and is in danger of significant shifts in snowmelt timing and runoff (Dettinger and Cayan, 1995; Cayan et al., 2001; Stewart et al., 2004). A majority of rivers in western North America have exhibited trends toward earlier snowmelt timing during the half century (1948-2000) (Stewart et al., 2004). The trend towards earlier melt is most prevalent in the Pacific Northwest, Rocky Mountain, Canadian, and Alaskan regions. The changes are driven primarily by broad-scale warming trends and regional scale moistening (northwestern North America) and drying (southwestern North America),

with temperature increases as more dominant than the volume of precipitation (Stewart et al., 2004). Projections for snowmelt timing at the end of the 21st century indicate very dramatic changes relative to the 1948-2000 time interval where shifts of 30 to 40 days are predicted for the Pacific Northwest, Sierra Nevada, and Rocky Mountain basins (figure 1) (Stewart et al., 2004).

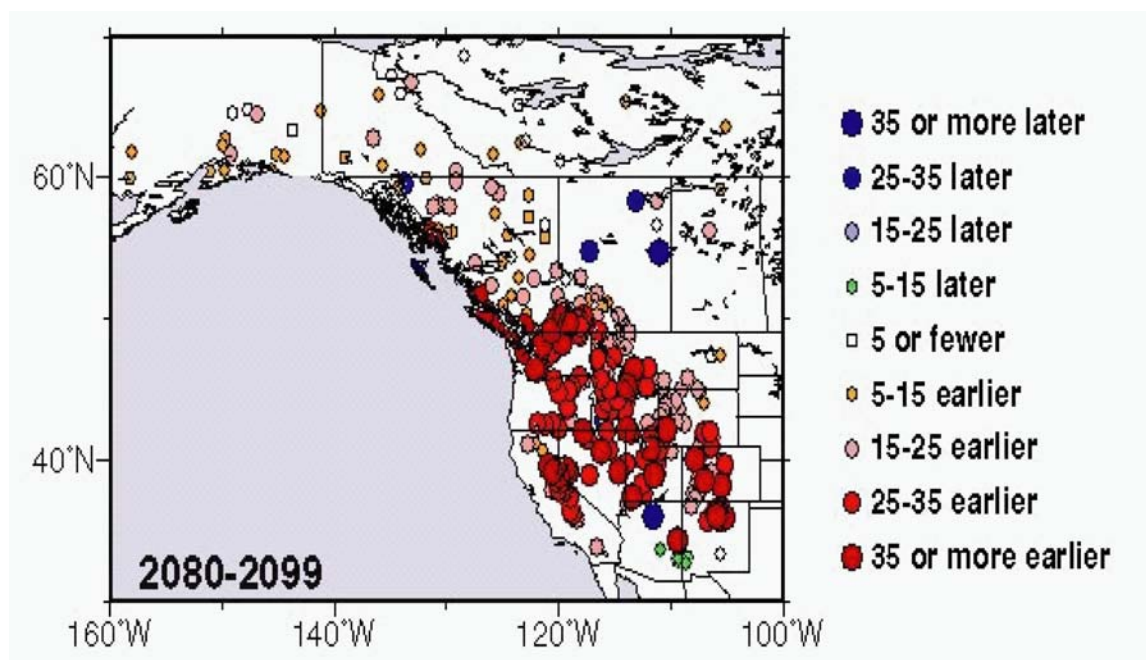


Figure 1: Projected changes in stream flow timing as a function of snowmelt discharge timing for the end of the 21st century (2080-2099). Values indicate difference in timing between (2080-2099) and (1951-1980). Figure was taken from Stewart et al., 2004.

Decreasing trends in snow cover across the western US were substantiated further substantiated by Mote (2003), through examination of ground-based measurements of snow water equivalent (SWE) at historical snow course sites from 1950-2000. Figure 2 illustrates large decreasing linear trends in SWE during this time interval across much of the western US, with larger decreases occurring in the Pacific Northwest, upper Sierra Nevada, and Upper Rocky Mountains. Mote (2003) focused in the Pacific Northwest and has surmised that increases in temperature play a substantial role in SWE trends, but that variations in the role precipitation plays is also a function of elevation.

Large scale atmosphere processes are known to influence the extent of snow cover, amount of accumulated water, and timing of melt throughout the Western US. Atmospheric processes manifest control in the condition of the snowpack through two primary factors; Precipitation and Temperature. Both are linked in their impact on snow cover characteristics as it varies temporally and spatially. The magnitude of their effects can vary dramatically as a function of regional heterogeneity expressed through provincial differences in topography, climatology, and location (latitude). In particular, for most regions in the Western US, anomalous snow accumulation is affected most by fluctuation in

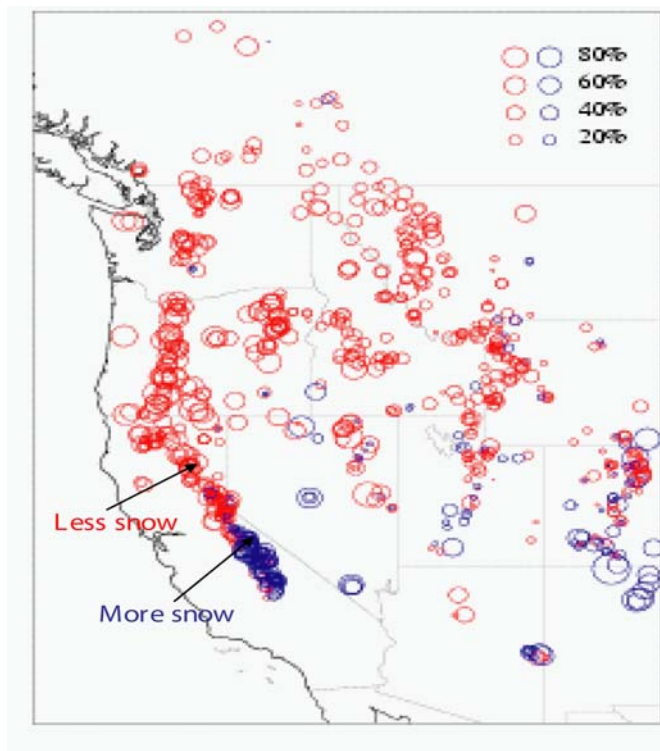


Figure 2: Linear trends in snow water equivalent (SWE) on April 1 over study period from 1950-2000. Negative trends are shown as red circles and positive in blue. The magnitude of trend is indicated by the area of the circle (Mote, 2003).

precipitation-winter and early spring precipitation anomalies extend over broad regional scales. Conversely, the regional impact of temperature is weak, but can vary depending on topography and season (Cayan, 1996). Temperature effects operate both during and after snow deposition: temperature mediates the partition of snow versus rain that falls and can determine the amount of snow that is melted after deposition (Cayan, 1996). The relative importance of precipitation and temperature on snow cover is heavily contingent by elevation. The impact of the temperature signal at higher elevations is reduced, except during the spring when the mean temperature is warmer. This is not the case in regions characterized by lower elevations. In these zones, temperature is especially influential, particularly near the snowline. It seems that at higher elevations, more precipitation is

partitioned into snow and can accumulate. The amount of accumulation in these regions becomes more a function of precipitation than temperature. At lower elevations, temperature can become more influential since there is greater variability in precipitation partitioning between snow and rain. This is particularly evident in the coastal Pacific Northwest (Cascades of Oregon and Washington, where snow course elevations are generally lower than 2200m, the amount of April 1 snowpack is strongly influenced by winter and spring temperatures but is not so dependent upon precipitation (Cayan, 1996). Serreze et al., (1999) used data from the SNOTel network to examine SWE variability across the Western US from 1963 through 1996. Subjective regions were delineated, partly based on Cayan (1996). Monthly precipitation for the Pacific Northwest peaks in November and decreases thereafter. Autumn temperatures are well above freezing, implying that early-season snowfall events tend to be offset by melt events and particularly, in October precipitation often falls as rain, delaying the seasonal rise in SWE (Serreze et al., 1999). Decreasing snow course trends in the Rockies indicate strong correlation with precipitation, where temperature is less important (Mote, 2003). Generally, the influence of temperature on the timing of snowmelt appears to vary as a function of latitude, where northern basins are more resistant to temperature fluctuations, because they are relatively cooler than southern basins that hover nearer the freezing point (Stewart et al., 2004).

Regional trends in snowmelt timing based on previous research are compelling, but lack comprehensive characterization of changes as a function of scale. Mote (2003) highlights this point by enumerating other factors that influence interpretation of inter-

annual correlations between SWE and climate trends, such as changes in land cover, wind speed and direction, topography, and even air pollution (affecting lowland precipitation more than high elevation mountain precipitation). These factors are indicative of the importance of scale. A more spatially coherent assessment of snow pack melt timing could shed light on whether or not observed changes in SWE (derived from snow course or automated SNOTel instruments) are indicative of global warming or natural (local) variability. It is essential that accurate information on the temporal and **spatial** dimensions of snow cover be available (Robinson, 1995). Advances in the capabilities of satellite remote sensing platforms in their ability to resolve greater spatial detail and discrimination between various land cover features, makes them well suited for the extraction and monitoring of snow cover conditions, particularly improved spatial characterization of snow melt onset, magnitude, and duration.

In most alpine terrain dominated by snow cover, a transition occurs between winter accumulation and spring melt season. During this transition period, the nature of snow cover changes and snowmelt runoff begins. Increased energy input to the snow surface and consequently availability of meltwater initiate these changes. As liquid water enters the snowpack, processes collectively known as ripening, aging or melt metamorphism ensue (Kattelman and Dozier, 1999). This process includes grain growth and rounding, ice-layer formation, warming of the snow to the melting temperature, densification, capillary retention of liquid water, and creation of a flow network (Kattelman and Dozier, 1999). This process characterizes the ‘evolution’ or ‘state’ of the snowpack in this analysis. This investigation is concerned with improved

observations of the spatial and temporal variability of mountain snow pack evolution under the larger rubric of global change and specifically regional climate variability in the Western US.

2. GROUND AND MODEL BASED METHODS FOR ASSESSING SNOWMELT

A thorough understanding of various characteristics about alpine snow cover, such as density, depth, accumulation, and temporal variation in extent, are vital to the effective management of these resources. There are a number of methods for the acquisition of snow cover information. These methods include the use of field-based approaches, such as snow course traverses, point measurements derived from manual data collection to automated facilities such as snow telemetry (SNOTel) stations. Monitoring of the snowmelt process and the release of water from an alpine snow pack, specifically, requires tracking several factors that characterize changes in the energy balance or heat budget of a snow pack. Ground-based data derived from point measured automated meteorological instruments are widely used in the computation of snowmelt from a watershed either using a physical energy balance or index approach. A physical energy balance technique requires information on radiation energy, sensible and latent heat, energy transferred through rainfall over snow and heat conduction from ground to the snow pack as input into models that simulate the melt process through well understood physics. Index methods utilize several variables in an empirical expression to estimate snow-cover energy exchange (Singh and Singh, 2000). Air temperature as well as net radiation, wind speed, vapor pressure, and solar radiation are all used in the index

approach. The degree-day approach in particular is most widely used and consists of summing the hourly surface temperatures at a meteorological station and dividing by 24. A reference temperature of 0° Celsius is commonly used. This reference is based on the assumption that most snowmelt results directly from the transfer of heat from the air in excess of 0° C (Singh and Singh, 2000). Snowmelt is derived from air temperature expressed in degree-days is commonly given by the following expression:

$$M = D_f (T_i - T_b) \quad [1]$$

Where:

M=depth of meltwater (mm) produced in a unit time interval.

D_f =the degree-day factor (mm degree C⁻¹).

T_i =index air temperature (degree C).

T_b =the reference temperature (usually 0° C).

Several physical-based energy balance models are used to simulate the snowmelt process. A comprehensive survey of 42 snow models was conducted by Yang (2001). The survey included several widely used models for various applications. Most models use precipitation, air temperature, wind speed, humidity, downward solar radiation and downward longwave radiation for snow surface energy and water budget computations (Yang, 2001). A number of models included in the surveys as well as others vary in their level of complexity. Some are single-layer models depicting the snow pack as a single, homogeneous, vertical layer with bulk properties, while other models are more complex with greater consideration for multi-layer mass, and energy exchanges. A primary

difference among models is how the calculation of the energy to melt snow is considered as well as the representation of internal processes within the snow (Koivusalo et al., 2001). Simple physical-based energy balance schemes using a single-layer representation of snow can successfully simulate the dominant snow processes, such as snowmelt and major energy fluxes. However, these simple schemes may become deficient when comparing the results against measurements of liquid water content and the thermal state of the snow (Koivusalo et al., 2001). Koivusalo and Heikinheimo (1999) conducted a comparison between a single-layer snow model Utah Energy Balance Snow Accumulation and Melt Model (UEB) and the multi-layer SNTHERM.89 model. The comparison revealed that both models yield successful mass balance calculations in terms of snow water equivalent and melt water discharge from the pack. Differences were found in the calculation of snow albedo and snow surface temperature, which altered the estimates of net radiation and turbulent heat fluxes, respectively.

3. SATELLITE SYSTEMS FOR MONITORING SNOWMELT

Many geographic studies require researchers to ask two important questions: the first is how large an area should be covered to appropriately examine a geographic phenomenon, or at what scale and resolution should the study be conducted. The second question is whether or not the results of the study at one scale can be interpolated to other scales (Cutter et al., 2002). We know that answering such questions has implications for understanding the processes under investigation. Depending upon the observation scale, processes that appear homogeneous at a small scale may become heterogeneous at a large scale, and parameters and factors that are important at one scale may become trivial at

another (Cao and Lam, 1997). Point vs. Area based measurements regarding the snowmelt process; require that we consider the implications in using either of these methods to optimally capture basin-scale snowmelt dynamics. Snowmelt modeling approaches previously discussed have proven to be very useful but are limited in representation of spatially distributed melt dynamics across large basins. The models require ground-based measurements as input derived from automated meteorological stations that do not sufficiently capture the greater spatial variability of the melt process in heavily heterogeneous, rugged terrain. Explicit treatment of scale effects in spatially distributed snowmelt models also poses significant limitations as well. The use of ground-based measurements suffers from a myriad number of limitations. Usually ground measurements have to be interpolated in order to produce spatially distributed information. The interpolation process introduces serious errors. These errors are a result of the failure to adequately capture the spatial variability of a particular variable. Molotch has explicitly addressed this problem and Bales (2005) in regards to the degree of spatial representation of SNOTel derived snow water equivalence (SWE) measurements. Molotch and Bales (2005) results indicate that SNOTel site locations are not representative of physiographic variables known to control snow distribution (i.e. elevation, slope, and incident solar radiation). Additionally, the acquisition of important hydrologic variables is difficult to acquire in the field (Koskinen et. al, 1999). Remote acquisition of snow properties has been employed over the last 50 years, spanning the use of high altitude land photography to aircraft and satellite systems. In the last 25 years, the use of space based remote sensors for acquiring snow cover information has been widely employed. Remote sensing technology offers improved distributed hydrologic

information across a range of scales over remote regions that are inaccessible or where gauging stations are sparse or nonexistent (Solberg et. al., 1997). The continuous spatial and temporal acquisition of satellite data spanning the solar reflective visible (0.4-0.7 μm), Near Infrared (NIR) (0.7-1.3 μm), Shortwave Infrared (SWIR) (1.3-3 μm), thermal infrared (3-14 μm) and microwave (0.3-300 GHz) (active and passive systems) regions of the electromagnetic spectrum, to monitor snow cover properties has been successfully demonstrated (Dozier, 1989; Nolin and Dozier, 2000; Kuittinen, 1992; Solberg et. al., 1997; Koskinen et. al., 1999; Piesbergen et. al., 1995; Nagler et. al., 1998 and many others). In the microwave region of the electromagnetic spectrum during the melt process, active systems register attenuation of radar return when snow is wet because of the impact liquid water has on incident microwave energy. The presence of liquid water increases the imaginary part of the dielectric constant for snow cover (Ulaby et. al, 1982). This response is due to increase microwave energy absorption, which effectively reduces the radar backscatter signal (Ulaby et. al., 1982). This makes active radar useful for monitoring snowmelt. For passive systems, when snow becomes increasingly wet (an increase in liquid water within the snow pack pore spaces), brightness temperatures exhibit a marked increase resulting from increased absorption enhancing surface scattering, decreasing volume-scattering, and increasing the emissivity of the snow surface (Mote et al., 1993).

The use of any particular remote sensing system for monitoring mountain snow melt dynamics requires considering relative advantages and disadvantages based on radiometric, spatial, and temporal resolutions as well as data volume provided by systems

operating in the various segments of the EM spectrum. Passive and active microwave systems provide significant sensitivity to the onset of surface melt as well as the capacity for all-weather acquisitions. Capabilities provided by microwave systems provide complete un-obscured spatial coverage day and night. The spatial resolution of active systems such as synthetic aperture radar (SAR) systems such as ERS-1/2 (30m) and RADARSAT (10-100m) are sufficiently high for monitoring mountain snow melt. Temporal resolutions (repeat acquisition time intervals) for active systems can be as coarse as 24 days, increasing the likelihood of under sampling significant melt events. Active microwave systems possess adequate radiometric sensitivity to melt onset, and also provide high temporal resolution data (daily) during cloudy days, day or not. The primary disadvantage of passive systems is their coarse spatial resolution, which can be as coarse as $\sim 25\text{km}^2$ for the Special Sensor Microwave Imager (SSM/I) and as low as 10km^2 for AQUA AMSR-E. Such coarse spatial resolutions make these systems well suited for large scale basin studies (Schultz and Engman, 2000). Additionally, heterogeneity of surface features and snow cover properties within the passive microwave footprint results in a mixed signature, which is ultimately represented by a single brightness temperature that is a weighted areal average of surface emission from each surface type (Schultz and Engman, 2000).

Satellite systems operating in the solar reflective and thermal regions of the electromagnetic spectrum offer significant advantages for tracking mountain snow melt dynamics. These systems span a wide range in spatial resolutions from sub-meter to tens of kilometers. Sensors with bands in the shortwave infrared region are very sensitive to the onset of snow surface melt. The temporal resolutions of these systems can be very

high, with some collecting repeat measurements multiple times daily (with multiple redundant systems operating simultaneously such as the NOAA-N series platforms carrying the Advanced Very High Resolution Radiometer (AVHRR)). Solar reflective and thermal systems suffer from the influence of sub-pixel heterogeneity, but the relative higher spatial resolutions such systems operate over can tend to reduce the degree of within-pixel variability, which makes possible the application of algorithms designed to resolve sub-pixel constituents through spectral un-mixing routines.

Moderate resolution sensors (spatial resolutions between 250m and 8km) collecting in the solar reflective and thermal regions of the EM spectrum have been in operation since the early 1980s providing global products at spatial resolutions between 250m to 8km. The Advanced Very High Resolution radiometer (AVHRR), part of the NOAA series platforms, has provided a vital record of the earth surface dynamics during this period (Townshend and Justice, 2002). The launch of the Earth Observing System (EOS) Moderate Resolution Imaging Radiometer (MODIS) aboard the TERRA and AQUA platforms has served the land remote sensing community since 2000 and 2002, respectively. The future Visible and Infrared Imaging Suite (VIIRS) aboard the National Polar-orbiting Operational Satellite System (NPOESS) and the forthcoming NPOESS Preparatory Program (NPP) will provide improved capabilities for land surface satellite remote sensing as a critical and advanced follow-up to the AVHRR and MODIS satellite systems (Townshend and Justice, 2002). The emergence of the VIIRS system, which will most resemble the capabilities of the MODIS system, will take place in stages with commensurate morning (9:30am) and afternoon (13:30pm) equatorial crossing time (ECT) (ascending node) as the AVHRR and MODIS systems, which current operate at

10:30am and 13:30pm ECT. The use of integrated satellite data records from these three systems (AVHRR, MODIS, and VIIRS) would provide a wealth of information about snow dynamics spanning from the early-late 1980s through the life of the VIIRS systems projected to operate aboard the final NPOESS system through 2012. This approximate 25-30 year satellite record could provide great insight into the annual and inter-annual variability of snow cover properties. The potential for surprising insights and new revelations about the spatial variability of snow cover properties can certainly be useful today and on an annual basis to users such as watershed managers and climate forecast scientists. In the long-term, the mining of such a data records for monitoring snow cover properties could really be the beginning of our understanding of long-term changes in snow dominated, alpine systems.

A viable approach for monitoring seasonal snow pack propensity for melt release could be based on time-variant snow surface optical and thermal properties. Lampkin and Yool (2005) explored this issue. Our model intends to track snow pack propensity for melt discharge using surface optical and thermal properties based on a similar approach used in vegetation remote sensing to track vegetation moisture content. The model has been called the Near Surface Moisture Index- (Snow) (NSMI) and is based on the surface moisture index (SMI), developed by Nemani et al. (1993). NSMI provides an estimate of relative wetness of features within a remotely sensed image. Figure 3 illustrates a conceptual NSMI feature space, when populated with time-variant measures of optical and thermal snow surface properties, theoretically maps the snow pack in

transition from isothermal conditions through vigorous melt production periods of the ablation season. Several important considerations must be addressed to render such an approach robust enough for operation application to data derived from an extensive time series of moderate resolution sensors (Table I).

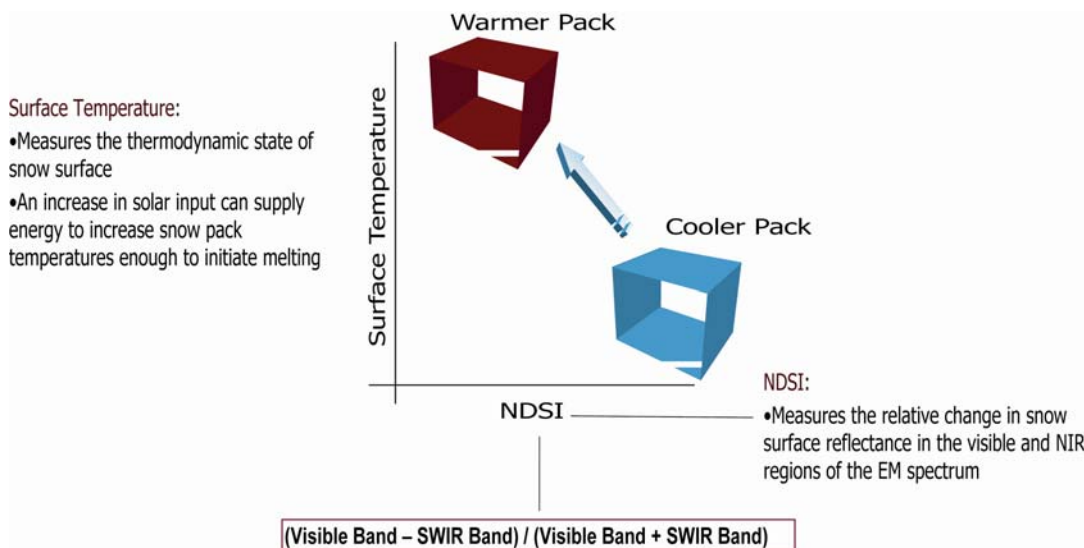


Figure 3: Theoretical near surface moisture index (NSMI) feature space for tracking snow pack evolution during the melt season using surface temperature and an optical-derived index sensitive to snow grain radius.

Table I. Primary Requirements for Successful Application of NSMI Approach

Snow surface optical and thermal information should index the internal energy state of the snow pack as the system receives energy and produce melt
Snow surface characteristics should be highly coupled to the internal state of the snow pack during the entire ablation season
Moderate scale optical/thermal satellite systems should be sensitive enough to changes in at-satellite signals associated with changes in snow surface reflectance due to changes in snow pack energy balance associated with melt production and discharge
Adequate treatment of mix pixel problem through use of sub-pixel snow cover extent as initial requirement for application of NSMI
Reduction of spectral contribution of alpine vegetation to total at-sensor signal from heterogeneous snow dominated terrain

Some of these requirements were addressed through the following research by Lampkin and Yool (2005) in a special issue of *Hydrological Processes*, a forthcoming manuscript in *Journal of Geophysical Research* and the last by Lampkin and Yool (2005) in a special issue of *Geocarto*; 1.) development of theoretical foundation and surface moisture sensitive algorithm developed from snow surface optical/thermal information used to track both surface melt and pack discharge potential; 2.) investigate time-dependent phases of coupling and decoupling between snow surface properties and melt discharge through analysis of long-term surface and sub-surface state variables collected from an automated system during an entire melt season; and 3.) examine sensitivity of optical satellite systems specifically, *EOS TERRA-MODIS*, through radiative transfer simulations of snow surface reflectance as a function of changes in snow grain size, associated with critical surface and sub-surface changes indicative of an evolving snow

pack. Work by Nolin et al. (1993) demonstrated the earliest effort to use spectral mixture analysis for subpixel snow cover mapping. Rosenthal and Dozier (1996) have demonstrated the use of a decision tree algorithm for the determination of sub pixel snow covered area from Landsat Thematic Mapper and AVHRR data over the Sacramento and San Joaquin River Basins in California. The NASA Southwest Regional Earth Science Applications Center (RESAC) has applied an adjusted version of the decision tree algorithm to map in near-real time and historical sub-pixel SCA using AVHRR over the Colorado River Basin from 1995 through 2002 (Bales et al., in preparation). Painter et al. (2003) have developed a spectral mixture approach for mapping subpixel snow cover and grain size from imaging spectrometer data. This algorithm is currently being transitioned to the EOS TERRA and AQUA Moderate Resolution Imaging Spectroradiometer (MODIS) (personal communication, Painter). Future work to reduce the spectral contribution of the vegetation signal to total upwelling energy in a complex snow-vegetation landscape will be address through application of a forced-invariance approach used by Crippen and Blom (2001). Crippen and Blom (2001) used this approach for unveiling the geology of vegetation dominated landscapes.

4. THEORETICAL BASIS FOR NSMI

4.1 *Surface Optical and Thermal Properties of Snow and the Snowmelt Process*

The albedo of snow, which affects snow pack energy balance, is a function of grain-size. The distribution of liquid water discharged from snow, which impacts the hydrology, is a function of the amount of melting (Green et al., 2002). Previous work has demonstrated that snow spectral reflectance is a strong function of grain-size and could be modeled from the optical properties of ice (Bohren and Barkstrom, 1974; Wiscombe and Warren, 1980; Warren, 1982; Dozier, 1989; Nolin and Dozier, 1993, Nolin and Dozier, 2000; Painter et al., 2003). The optical (wavelengths (λ) spanning the solar reflective visible (0.4-0.7 μm), Near Infrared (NIR) (0.7-1.3 μm), Shortwave Infrared (SWIR) (1.3-3 μm)) properties of snow depend on the bulk optical characteristics and the geometry of the ice grains, liquid water inclusions, and solid and soluble impurities (Dozier, 1989). More specifically, in the visible and NIR regions of the electromagnetic spectrum (EM), the bulk radiative properties of ice and water are similar, so the reflectance and transmittance of the snow pack depend on wavelength variations of the refractive index of ice, grain radius distribution, depth, density, and the size and amount of impurities, whose refractive indices are significantly different from those of ice and water. The presence of liquid water in pore space between snow grains enhances energy transfer between grains, accelerating grain growth (Colbeck, 1982) and greatly influencing snow reflectance. This affect is more pronounced in the NIR regions of the

EM spectrum, primarily as a function of microstructural changes (Dozier, 1989). The complex refractive index of ice (ε), given by:

$$\varepsilon + i \varepsilon'' \quad [1]$$

where:

ε = real part of the refractive index

ε'' = imaginary part of refractive index

is the most important optical property of ice, which governs spectral variation in reflectance of snow in the visible, NIR, and SWIR regions of the EM spectrum.

Specifically, the absorption coefficient (κ_i), which is related to the imaginary component of the refractive index of ice by:

$$\kappa_i = 4\pi\varepsilon''/\lambda \quad [2]$$

increases substantially in magnitude for λ between 0.4 to 2.5 μm . Such an increase causes snow reflectance to substantially decrease as λ increases, indicative of greater absorption.

The melt process is characterized by a substantial decline in snow reflectance. This

process is accompanied by the production of melt and an increase in liquid water occupying ice pore spaces, yet it is not the presence of liquid water directly that produces the resultant decrease in reflectance. This decrease is primarily a function of an increase in the effective grain size, resulting from two- to four grain clusters that form during melt, which optically behave as a single large grain (Dozier, 1989). In wet snow with high liquid water content, smaller particles are at lower temperatures, and heat flow from large grains causes their melting and entrainment into larger particles (Colbeck, 1982). As grain radius increases (which can range from $\sim 50\mu\text{m}$ for new snow to $1\text{mm}+$ for old melting snow) an incident photon will have a high probability of being scattered when it transverses an air-ice interface, but a greater chance of absorption while passing through the ice grain. An increase in grain size causes an increase in the path length that must be traveled through the ice grain between scattering opportunities (Warren, 1982). The extended photon path length increases the amount of energy absorbed, resulting in a decline in reflectance.

Thermal radiation ($3.5\text{-}50\mu\text{m}$) is absorbed and emitted by the atmosphere without appreciable scattering (Marks and Dozier, 1992). Thermal remote sensing platforms operate over a more restricted range in the EM spectrum, with many systems operating in the atmospheric window between 8 and $14\mu\text{m}$. Snow cover melt dynamics in the thermal region of the EM spectrum are a function of incident radiation as well as surface longwave emission. The onset of melt is representative of a continuum within the snowpack. The pack is better characterized as an evolving medium, which initially manifest microstructural changes indicative of metamorphic transitions. Surface and near

surface segments of the snow pack are the primary interface through which energy enters the pack to drive these structural changes. Energy input in the form of solar radiation (addressed in the previous discussion) and thermal input derived from large diurnal variations in temperature are responsible for initial near surface changes. (Colbeck, 1989) examined the relative importance of solar insolation and diurnal temperature variation in the onset of rapidly crystal growth near the snow surface. Simulations in this analysis indicate that from the surface down to approximately 0.25m, grain growth would increase with increasing radiation input, but this process is pronounced due to strong diurnal air temperature fluctuations. These two processes induce strong temperature gradients within the uppermost regions of the snow pack, driving vapour flow and constructive grain metamorphism. Colbeck (1989) assumes that these two processes are more intense for high altitude snow cover at low latitudes with the most vigorous growth occurring within the upper 0.1m of the pack. Thermal exitance is a function of snow surface skin temperature and emissivity (Marks and Dozier, 1992). Dozier and Warren (1982) determine that thermal infrared emission does not depend on grain size, density, liquid water content, and impurities, but primarily on the viewing geometry. Snow highly approximates the behaviour of a blackbody with emissivities ranging between 0.985-0.990 and is relatively invariant to wavelength in the 8-14 μ m interval (Dozier and Warren, 1992). Marks et al. (1992) illustrate in the Sierra Nevada that near surface snow temperature tends to follow air temperature as a result of the surface layer establishing thermal equilibrium with the near surface atmosphere. Satellite derived surface temperatures can be useful in tracking changes in surface conditions that are correlated with internal melt production. The use of snow surface reflectance alone would not

suffice in this endeavour, primarily because substantial decreases in reflectance are not solely due grain enlargement resulting from melt onset. Impurities and litter on the snow surface can cause substantial reductions in reflectance (Warren, 1982). Snow surface temperature information coupled with optical information would assist in narrowing those surface conditions most indicative of an increase in energy input and melt production. Interestingly, a small amount of surface impurities has the most effect on reflectance mainly in visible wavelengths ($\lambda < 1\mu\text{m}$) (Warren, 1982). A decline in reflectance means an increase in absorption, therefore the presence of surface impurities may accelerate the melt process.

4.2 Snow Surface Optical Properties and Energy Balance Process during Melting

The energy balance equation is used to quantify snowmelt and applied to a control volume of snow, allows the fluxes of energy penetrating the snow surface and retained by the volume to be expressed as changes in internal energy (Shook and Gray, 1997).

Generally, the energy balance of a snow pack is expressed as

$$\Delta Q = S_{\text{net}} + H + L_v E + G + M \quad [3]$$

where ΔQ is change in snow pack energy, S_{net} , H , $L_v E$, G , and M are net radiation, turbulent sensible, turbulent latent, conductive, and advective energy fluxes. When the

pack is in temperature equilibrium ($\Delta Q = 0$) the resulting negative energy balance will cool the snow pack, increasing its cold content (the amount of energy required to bring it to 0°C).

$$C_c = -C_i \int \rho_s T dz \quad [4]$$

where ρ_s , C_i , T are density, specific heat of ice, and layer temperature respectively and integrated over depth (dz). Conversely, a positive energy balance will warm the snow pack. Energy input to the snow pack is initially partitioned into overcoming the ‘cold content’. Once the snow pack has become isothermal, additional energy goes towards solid to liquid phase change (positive ΔQ) and melt is produced. Melt conditions of an isothermal snow pack can be influenced by air temperatures above 0°C , which could produce precipitation input to the pack as rain adding energy through latent heat transfer. During periods of active melting net radiation and convective ($H + L_v E$) serve as dominant energy sources for melt production. Given the temperature of the pack changes little during this period, large changes in the internal state of the pack are mitigated by latent rather than sensible heat input ($L_v E$ rather than H) (Oke, 1987). If the air above the snow pack is warmer than the snow surface, the vapour pressure is higher in the air promoting an air-to surface vapour pressure gradient. The resultant downward turbulent flux of moisture and condensation would add energy to the snow surface given the latent heat of vaporization released during condensation (at 0°C) is 7.5 times higher than latent heat of fusion required for melting water (Oke, 1987). The primary source of energy during melt is net radiation. The net radiation term (S_{net}) in (1) can be decomposed into the following shortwave (K) and longwave (L) flux components:

$$S_{\text{net}} = K_{\downarrow} - K_{\uparrow} + L_{\downarrow} - L_{\uparrow} = K_{\text{net}} + L_{\text{net}} \quad [5]$$

where the arrows denote incoming (\downarrow) and outgoing (\uparrow) energy (Oke, 1987). Given the significant contribution solar irradiance makes to the snowmelt process, snow pack reflectance and absorption characteristics, as a function of wavelength (λ), can influence the amount of solar radiation partitioned into energy for melt production. Incident photons that are not reflected from the snow pack will be absorbed in ice grains and converted to heat. Since the thermal diffusivity of snow is low, this heat energy will be retained at depth (Dozier et al, 1989). Asymmetry can occur between radiative cooling and appears to have warmed more rapidly than it cooled (Nolin, 1993). This process can result in subsurface heating and has been characterized as the “solid-state greenhouse effect”. Matson and Brown (1989) as well as Nolin (1993) has examined this phenomena, which results from both rapid absorption of shortwave energy at depth with relatively little loss in energy through longwave (thermal) emission only from the surface of the snow pack. More energy is retained at depth resulting in the onset of melt near the surface although surface air temperatures may not exceed 0° C (Dozier et al., 1989). Energy available to drive this process is that not reflected (but absorbed) expressed as (Oke, 1987):

$$K_{\text{net}} = K_{\downarrow} (1-\alpha) \quad [6]$$

where variation in surface albedo (α) can influence the amount of energy entering the

pack for melt. Once the pack has become isothermal, additional energy, primarily controlled by this radiative process goes directly towards the production of melt. This process starts in the upper part of the pack and proceeds downward, initially producing intermittent melt. This melt infiltrates deeper into the pack and refreezes, adding latent heat to the pack at depth. As the melt season continues, this process becomes more pronounced, producing preferential flow paths for melt to exit the snow pack (Wakahama, 1965).

This dynamic link between surface radiative conditions and the pack's propensity for melt production and release is the primary mechanism the algorithm proposed in this analysis attempts to leverage.

Acknowledgments. This study was supported by NASA under the Earth System Science Fellowship (ESS) Grant NGT5. Thanks to Dr. Steve Yool for guidance and Dr. Andrew Comrie for his suggestions.

REFERENCES

Cao, Changyong and Nina Siu-Ngan Lam. 1997. "Understanding the Scale and Resolution Effects in Remote Sensing and GIS." Scale in Remote Sensing and GIS. Dale A. Quattrochi and Michael F. Goodchild, Eds. Boca Raton, FL: CRC Lewis, 57-72.

Cutter, S.L. Golledge, R., Graf, W.L., 2002. The big questions in geography. *The Professional Geographer*, Volume 54, Number 3, 305-317.

Bales RC, Dressler KA, Imam B, Fassnacht SR, Lampkin DJ, Helfrich, SR. Fractional snow cover in the Colorado and Rio Grande basins, 1995-2002. In preparation to *Water Resources Research*.

Bohren, C.F., and B. R. Barkstrom. 1974. Theory of the optical properties of snow. *Journal of Geophysical Research*, Volume 79, No. 30, 4527-4535.

Cayan, D.R. 1996. Interannual climate variability and snowpack in Western US. *Journal of Climate*, Volume 9, 928-951.

Cayan, D.R., S.A. Kammerdiener, M.D. Dettinger, J.M. Caprio, and D.H. Peterson. 2001. Changes in the onset of spring in the Western United States. *Bull. Amer. Meteorol. Soc.*, Volume 82, 399-415.

Colbeck, S.C. 1982. An overview of seasonal snow metamorphism. *Review of Geophysics and Space Physics*, Volume 20., No. 1, pp45-61.

Colbeck, S.C. 1989. Snow-crystal growth with varying surface temperatures and radiation penetration. *J. Glaciol.*, Volume 35, no. 119, pp 23-29.

Crippen, R.E. and R.G. Blom, Unveiling the Lithology of Vegetated Terrains in Remotely Sensed Imagery, *Photogrammetric Engineering & Remote Sensing*, 67(8): 935-943, 2001.

Dettinger, M.D. and Cayan, D.R. 1995. Large-scale atmospheric forcing of recent trends toward early snowmelt runoff in California. *Journal of Climate*, Volume 8, 606-623.

Dozier, J. 1989. Spectral signature of alpine snow cover from the Landsat Thematic Mapper. *Remote Sens. Environ.*, 28, 9-22.

Dozier, J., and S.G. Warren. 1982. Effect of view angle on the infrared brightness temperature of snow. *Water Resources Research*, Volume 18, No. 5, 1424-1434.

Dozier, J., R.E. Davis, and A. Nolin. 1989. reflectance and transmittance of snow at high spectral resolution, in IGARSS '89, *Quantitative remote sensing: an economic tool for the Nineties*, Vancouver, Canada, 662-664, IGARSS '89 12th Canadian Symposium on Remote Sensing, No 89Ch2768-0.

Green, R.O., R.D. Roberts, and T. Painter. 2002. Spectral snow-reflectance models for grain-size and liquid water fraction in melting snow for the solar-reflected spectrum.

Annals of Glaciology, Volume 34, 71-73.

Kattelman, R., and J. Dozier. 1999. Observations of snowpack ripening in the Sierra Nevada, California, USA. *Journal of Glaciology*, Volume 45, No. 151, 409-416.

Koivusalo, H., M. Heikinheimo, and T. Karvonen. 1999. Surface energy exchange over a boreal snowpack: comparison of two snow energy balance models. *Hydrol Process*, Volume 13, 2395-2408.

Koivusalo, H., M. Heikinheimo, and T. Karvonen. 2001. Test of a simple two-layer parameterization to simulate the energy balance and temperature of a snow pack. *Theor. Appl. Climatol.* Volume 70, 65-79.

Koskinen, J., S. Metsamaki, J. Grandell, S. Janne, L. Matikainen, and M. Hallikainen. 1999. *Snow monitoring using radar and optical satellite data*. Remote Sens. Environ., vol (69), pp16-29.

Kuittinen, R. 1992. *Remote sensing for hydrology progress and prospects*, WMO Operational Hydrology Report, No 36, WMO-No. 773, WMO. Geneva, Switzerland.

Lampkin, D.J., and S.R. Yool. 2005. Monitoring mountain snowpack evolution using near-surface optical and thermal properties. *Hydrological Processes*, Volume 18, 3527-3542.

Marks, D., and J. Dozier. 1992. Climate and energy exchange at the snow surface in the alpine region of the Sierra Nevada 2. Snow cover energy balance. *Water Resources Research*, Volume 28, No. 11, 3043-3054.

Marks, D., J. Dozier, and R.E. Davis. 1992. Climate and energy exchange at the snow surface in the alpine region of the Sierra Nevada 1. Meteorological measurements and monitoring. *Water Resources Research*. Volume 28, No. 11, 3029-3042.

Matson, D.L., and R.H. Brown. 1989. Solid-state greenhouses and their implications for icy satellites. *Icarus*, Volume 77, 67-81.

Molotch, N.P., and R.C. Bales. 2005. Scaling snow observations from the point to the grid-element: Implications for observation network design, AGU Hydrology Days, Fort Collins, Co.

Mote, T.L., M.R. Anderson, K.C. Kuivinen, and C.M. Rowe. 1993. Passive microwave-derived spatial and temporal variations of summer melt on the Greenland ice sheet. *Annals of Glaciology*, Number 17, 233-238.

Mote, P.W. 2003. Trends in snow water equivalent in the Pacific Northwest and their climatic causes. *Geophysical Research Letters*, Volume 30, No. 12.

doi:10.1029/2003GL017258.

Nagler, T. and H. Rott. 1998. SAR tools for snowmelt modeling in the project HydAlp. In Proceedings of IEEE International Geoscience and Remote Sensing Symposium (IGARSS'98) Symposium, Seattle, WA, IEEE, New York.

Nolin, A., and J. Dozier. 1993. Estimating snow grain size using AVIRIS data. *Remote Sens. Environ.*, Volume 44, 231-238.

Nolin, A., and J. Dozier. 2000. A hyperspectral method for remote sensing of grain size of snow. *Remote Sens. Environ.*, Volume 74, 207-216.

Piesbergen, J., F. Holecz, and H. Haefner. 1995. Snow cover monitoring using multitemporal ERS-1 SAR data. In Proceedings of IEEE International Geoscience and Remote Sensing Symposium (IGARSS'95), Florence, Italy, IEEE, New York, pp. 1750-1752.

Oke, T.R. 1987. Boundary layer climates 2nd edition. Routledge.

Painter, T.H., J. Dozier, D.A. Roberts, R.E. Davis, and R.O. Green. 2003. Retrieval of subpixel snow-covered area and grain size from imaging spectrometer data. *Remote Sens. Environ.*, Volume 85, 64-77.

Robinson, D.A. 1995. Decadal variations of snow cover in *Natural Climate Variability on Decade-to-Century Time Scales*, National Research Council, National Academy Press, Washington, DC, 60-66.

Serreze, M.C., M.P. Clark, and R.L. Armstrong. 1999. Characteristics of the western united states snowpack from snowpack telemetry (SNOTEL) data. *Water Resources Research*, Volume 35, No. 7, 2145-2160.

Singh, P, and V.P. Singh. 2001. *Snow and glacier hydrology*. Kluwer Academic Publishers.

Shook, K., and D.M. Gray. 1997. Snowmelt resulting from advection. *Hydrological Processes*, Volume 11, 1725-1736.

Solberg, R. D. Hiltbrunner, J. Koskinen, T. Gunneriussen, K. Rautianen, M. Hallikainen. 1997. *Snow algorithms and products, SNOWTOOLS WP410*, Norwegian Computing Center, Report 924, Oslo, Norway, 112.

Stewart, I.T., D.R. Cayan, and M.D. Dettinger. 2004. Changes in snowmelt runoff timing in Western North America under a 'business as usual' climate change scenario. *Climate Change*, volume 62, 217-232.

Townshend, J.R.G., and C.O. Justice. 2002. Towards operational monitoring of terrestrial systems by moderate-resolution remote sensing. *Remote Sens. Environ.*, Volume 83, 351-359.

Ulaby, F.T., R.K. Moore, and A.K. Fung. 1982. Microwave remote sensing: active and passive volume II, radar remote sensing and surface scattering and emission theory. Addison-Wesley Publishing Company.

Wakahama, G. 1965. Metamorphisms of wet snow. *Low Temp. Sci., Ser. A*, Volume 23, 51-66.

Warren, S.G. 1982. Optical properties of snow. *Rev Geophys. Space Phys.* 20:67-89.

Wiscombe, W.J., and Warren, S.G. 1981. A model for the spectral albedo of snow I: Pure snow. *J. Atmos. Sci.*, 37:2712-2733.

Yang, Z.-L. 2003. Description of recent snow models, in *Snow and Climate*, in eds. E. Martin and Armstrong, International Committee on Snow and Ice.

Appendix B

**Numerical Simulations of MODIS Sensitivity Potential for Assessing Near Surface
Mountain Snow Melt**

**NUMERICAL SIMULATIONS OF MODIS SENSITIVITY POTENTIAL FOR
ASSESSING NEAR SURFACE MOUNTAIN SNOW MELT**

D.J. Lampkin and S.R. Yool
Department of Geography and Regional Development
The University of Arizona
Tucson, AZ 85721
Phone: 520-626-8523
Fax: 520-621-1422
Email: dlampkin@hwr.arizona.edu

Glossary of Symbols

Symbol	Name
μm	micrometers
nm	nanometers
λ	wavelength [μm]
X	size parameter, which describes the size of a sphere relative to the wavelength of incident electromagnetic energy
r	spherical particle radius [μm]
θ_s	zenith angle of incident beam [degree]
$\rho_{m,\lambda}$	simulated directional hemispherical reflectance
L^0_λ	simulated at-sensor radiance, assuming horizontal Lambertian surface target [$\text{W}\cdot\text{m}^{-2}\cdot\text{sr}^{-1}\cdot\mu\text{m}^{-1}$]
L^s_λ	simulated at-satellite radiance assuming variable surface slope [$\text{W}\cdot\text{m}^{-2}\cdot\text{sr}^{-1}\cdot\mu\text{m}^{-1}$]
τ_s	downward atmospheric transmission through solar incident angle
Φ_s	solar azimuth angle [degree]
Φ'	surface azimuth angle [degree]
α	surface slope angle [degree]
τ_v	upward atmospheric transmission through view angle
E^b_λ	direct solar irradiance [$\text{W}\cdot\text{m}^{-2}\cdot\mu\text{m}^{-1}$]

ABSTRACT

Variations in amount of near surface snow melt produce changes in snow grain size. We evaluated Moderate Resolution Imaging Spectroradiometer (MODIS) visible and near-infrared band for monitoring snow pack ripeness using a Mie scattering model, coupled with a simple approach for computing directional hemispherical reflectance (albedo or total flux leaving surface divided by total irradiance). Results suggest MODIS visible and near-infrared bands may have the potential to detect changes in grain size as an indicator of mountain snow pack evolution during the melt season. Modeled at-sensor radiance was produced for grain size changes ranging from $10\mu\text{m}$ to $1000\mu\text{m}$.

Differences in simulated at-sensor radiance as a function of grain size, solar zenith angle, surface slope, and amount of diffuse irradiance were compared to band specific noise equivalent radiance (NE Δ L) thresholds. MODIS wavelengths greater than 667nm may be sensitive to large changes in grain sizes, particularly those bands with coarse spatial resolution (1000m). Longer wavelengths showed greater sensitivity to small changes in smaller grains than to small changes in larger grains. Shorter wavelengths with small fine spatial resolution (500m) appear less effective overall for monitoring changes in grain size. Variation in solar zenith angle has a greater impact on changes in larger grains (100-1000 μm) than smaller (10-100 μm). The overall magnitude of difference in modeled at-sensor radiance demonstrates that the affect of diffuse irradiance may not be substantial. Surface slope does not appreciably affect changes in model at-sensor radiances for various grain sizes. This may not be true given the model does not account for snow BRDF.

1. INTRODUCTION

An understanding of global and regional change in climate and the assessment of water resources require we monitor the temporal and spatial variability of snow cover characteristics from local to global scales (Dozier, 1989).

Continuous monitoring of temporal and spatial variability in snow cover is needed to address complex relationships among seasonal forested canopy snow cover, climate, and water resources (Dozier, 1989). Snow stores at least one third of the water used for crop irrigation worldwide (Steppuhn, 1981). Variability in regional climate affects snow covered area, amount, and timing of yields. Monitoring snow cover is important particularly in the semi-arid western United States, where annual water consumption averages 44% of renewable supplies, compared to 4% in the rest of the country (El-Ashry and Gibbons, 1988). Snow typically changes how drainage basins respond to the input of water; moreover, water stored as snow enters the basin over an extended period of time (Schultz and Engman, 2000).

In the last 20 years remote sensing research has led to significant progress in monitoring and measuring certain snow hydrologic processes. In particular, estimating the timing of snowmelt run-off can be improved by monitoring when the snowpack is primed to produce run-off. Remote sensing can provide a rough estimate of melt by monitoring the snowpack in the early spring with a variety of sensors (Rango, 1993); Sensors in the visible and near- infrared portion of the spectrum have become important data sources for snow studies from regional to global scales (Rott, 1987). Snowpack radiation balance controls heating and melting in the surface layer of snow, which affects spectral reflectance from the snow surface (Davis et al., 1993). Snow reflectance in the

near-infrared wavelengths depends on the metamorphic state of the snow; in the visible spectral region, reflectance is controlled by the amount and distribution of absorbing impurities (Davis et al., 1993). Radiation is the dominant component of the energy budget and drives snow metamorphism, leading to changes in snow grain size and reflectance (Colbeck, 1989).

We used simulated at-sensor radiances to evaluate the potential of TERRA Moderate Resolution Imaging Spectroradiometer (MODIS) visible and near-infrared bands for monitoring snow surface metamorphism due to melting.

2. BACKGROUND

Once seasonal snow cover has been established in a basin, the snow undergoes various transformations: The snowpack changes rapidly in spring reaching an isothermal state at 0°C and satisfying the snowpack liquid water holding capacity (Rango, 1993). When these two conditions have been met, the snowpack is ripe and absorption of additional energy will produce snowmelt (Rango, 1993). As melt progresses entrained liquid water within the snow pack matrix tends to increase grain size. Grain clusters form quickly, decreasing reflectance (Davis et al., 1993). Nolin and Stroeve (1997) demonstrated the relationship between snowpack energy balance, grain growth, and albedo. Nolin (1998) used a one-dimensional model of snowpack energy and mass balance to calculate grain growth and that output was then used to drive a radiative transfer model that calculated spectral albedo at each time step. Changes in energy balance were seen to strongly affect albedo through grain growth, especially during

periods of snowpack warming. These data show that in the near-infrared wavelengths, albedo values drop nearly 20% during a 10-day period during which grain sizes increased significantly (Nolin, 1998).

Work has been done to extract and monitor snow surface grain size and liquid water using airborne and satellite measurements. Dozier et al. (1981) examined the impact of grain size and snow pack water equivalence on snow reflectance in the visible and NIR regions of the EM spectrum, using the delta-Eddington approximation to the equation of radiative transfer. The delta-Eddington approach decomposes the equation of radiative transfer into orthogonal Legendre polynomials, and is designed to handle strongly forward-directed scattering media such as snow (Liou, 2002). An increase in grain size was found to cause a decline in snow surface albedo.

Examination of Advanced Very High Resolution Radiometer (AVHRR) visible and NIR signatures acquired over transects in Canada demonstrated satellite observations could be used to detect the presence of surface melt (Dozier et al., 1981). In particular, modeled reflectance showed optimal sensitivity to changes in snow surface grain size was between $1\mu\text{m}$ and $1.2\mu\text{m}$, and extends to about $1.4\mu\text{m}$ (Dozier et al., 1981). Green and Dozier (1996) explored use of a discrete-ordinate approximation of the radiative transfer equation to model snow as a mixture of ice and liquid water spheres. The discrete-ordinate method involves discretization of the basic radiative transfer equation and the solution of a set of first-order differential equations (Liou, 2002). Modeled spectra as a function of grain size and liquid water content were fit against spectra acquired from the Airborne Visible/Infrared Imaging Spectrometer (AVIRIS) Mammoth Mountain data set in California. Results indicate grain size and

melt water retrievals were consistent with the range of elevations and temperatures for the data (Green and Dozier, 1996). Snow melt estimates were high in vegetated regions due to the presence of liquid water in the leaves (Green and Dozier, 1996). Nolin and Dozier (2000) retrieved snow grain size from near-infrared AVIRIS data using an inversion technique that relates an ice absorption feature centered at $1.03\mu\text{m}$ to an optically equivalent snow grain size. This technique requires, however, that pixels be completely snow covered, have less than 1% litter by weight on the surface, and that the sensor carry sufficiently high spectral resolution to resolve the absorption feature (Nolin and Dozier, 2000). Green et al. (2002) used a radiative transfer model to simulate snow reflectance as a function of grain size and liquid water fraction for the visible region of the electromagnetic (EM) spectrum. Green et al. (2002) developed two models of spectral reflectance of melting snow: The first modeled treated melting snow as interspersed spheres of ice and liquid water; the second simulated melting snow as spheres with liquid water shells. Both models showed a shift in the absorption features centered at $1.03\mu\text{m}$ towards shorter wavelengths, consistent with the location of minima in the complex refractive index of ice vs. liquid water (Green et al., 2002). Validation of modeled reflectance was performed by comparing modeled snow spectra with measured spectra of frozen and melting snow. Measured spectra demonstrated the same shift in the $1.03\mu\text{m}$ absorption features towards shorter wavelengths (Green et al., 2002). Painter et al. (2003) used AVIRIS to retrieve sub-pixel snow-covered area and grain size using the multiple end-member snow-covered area and grain size (MEMSCAG) algorithm. MEMSCAG maps sub-pixel snow cover and grain size simultaneously using spectral mixture

analysis coupled with radiative transfer modeling of snow spectra (Painter et al., 2003). MEMSCAG had a 4% RMSE for snow-covered area, compared to snow area determined with high resolution photographs. For grain radii ranging from 80 to 750 μm , MEMSCAG had a RMSE of 74 μm for a mean of 3 x 3-pixel AVIRIS window (Painter et al., 2003). Airborne sensors such as AVIRIS contain superior spatial detail, but often lack the necessary coverage to monitor snow cover in mountain basins spanning several degrees of latitude. Airborne systems collect data on a per request basis, making them insufficient for operational monitoring of snow cover.

MODIS provides adequate spatial and spectral resolution within the visible and near infrared for monitoring basin-scale mountain snow cover (Table I). Painter et al. (2003) speculated that MODIS band centered at 1.24 μm could prove useful in mapping sub-pixel snow area and grain size. Our study is a first-order assessment of the potential sensitivity of MODIS visible and near-infrared (NIR) bands (0.405 μm to 1.25 μm), to changes in near surface conditions of mountain snow cover. We assume changes in grain size serve as a remote sensible proxy for monitoring the onset and duration of snow surface melt.

Table I: MODIS sensor characteristics.

Sensor Specifications			
Height	705 km		
Decending Node	10:30am		
Ascending Node	1:30pm		
Orbit	Sun-Synchronous, circular, near-polar		
Swath Dimensions	Cross-Track	Along-Track (Nadir)	
	2330 km	10 km	
Spatial Resolution	250 m	500 m	1000 m

Source: <http://modis.gsfc.nasa.gov/about/specs.html>

3. THEORY AND MODEL

Snow grains occur in a variety of shapes; many are non-spherical and concave. To model them via Mie scattering theory requires the assumption that scattering properties of the grain can be represented appropriately by an ‘equivalent sphere’ of known radius (Dozier and Warren, 1982). An optically equivalent sphere is then used to approximate ice crystals in the snow pack. This equivalent sphere is that which has the same volume-to-surface ratio as the irregularly shaped grains in the snowpack (Nolin, 1998). Grain size r (according to symbol convention used in Wiscombe and Warren, 1981) will refer in this paper to an optically equivalent sphere. Modeling the scattering and absorption of radiation by snow using Wiscombe-Warren Model

(WWM) (Wiscombe and Warren, 1981) assumes each grain scatters within the far field of surrounding grains. This condition is not always true for closely packed grains in a natural snow pack, but the assumption holds for spheres that are in relative isolation, where 1) spheres are not arranged in a regular array; 2) inter-particle interference effects are negligible since the center-to-center separation d is large compared to the incident wavelength λ , for the solar spectrum (Dozier and Warren, 1982); 3) each grain is exposed to an incident plane wave; and 4) grains do not shadow one another (Wiscombe and Warren, 1981). Formulas for modeling scattering by spheres using Mie theory require as input the dimensionless size parameter, given by:

$$X \equiv 2\pi r / \lambda \quad [1]$$

where:

r = radius of grain

λ = wavelength of incident energy

as well as complex refractive index $m(\lambda)$ for a given wavelength and grain radius. These parameters are used to derive single-scatter albedo (ω) (ratio of scattering to extinction cross-section), and the asymmetry factor (g) (mean value of $\cos\theta$, where θ is the scattering angle) (Mie, 1908; Wiscombe, 1980; Wiscombe and Warren, 1981).

WWM was used to compute directional hemispherical reflectance or albedo, which is the integrated total flux leaving a surface in all directions divided by the total irradiance (Warren, 1982). Directional hemispherical reflectance was computed for near surface non-shallow snowpack, as a function of wavelength and grain size for wavelengths between 0.4 μm and 1.2 μm (in 0.1 μm increments). Mie scattering parameters and solar zenith angle are inputs to the model. WWM determines directional hemispherical reflectance, neglecting polarization, as well as the influence of surface contaminants (i.e. soot) for a semi-infinite snow pack (i.e substrate reflectance causes less than 1% change in snow cover reflectance (Dozier et al., 1989)) and direct beam illumination, at a solar zenith angle θ , using the delta-Eddington approximation to the equation of radiative transfer (Wiscombe and Warren, 1981).

For the visible wavelength region the difference in intensities between considering and not considering polarization was generally less than 1% (Hansen, 1971). The assumption of an optically semi-infinite snowpack is valid under certain conditions. Because of the inverse dependence of optical depth on grain radius, radiation will penetrate deeper into the pack of larger particles if the density is constant. Snowpack thickness(given in liquid water equivalent, according to Wiscombe and Warren (1981), necessary to regard the snowpack as semi-infinite is 2 cm for grain radius $r = 50\mu\text{m}$ ($\rho = 0.1 \text{ g cm}^{-3}$), ~ 8 cm for $r = 200\mu\text{m}$ ($\rho = 0.4 \text{ g cm}^{-3}$), and 20 cm for $r = 1000\mu\text{m}$ ($\rho = 0.4 \text{ g cm}^{-3}$). Generally, the model is robust in representing the behavior of snow cover in the visible and near-infrared regions, but has limitations: WWM neglects effects due to close packing, which restricts its validity to $\lambda \leq 20\mu\text{m}$

and nonsphericity of snow grains, which may cause errors at very large solar zenith angles θ , approaching 90° . The model calculates only fluxes, not intensities, with no accounting for snow Bidirectional Reflectance Distribution Function (BRDF) (Warren, 1982). Directional hemispherical reflectance differs from BRDF in that the BRDF is a measure of reflected energy in a particular direction, given incident energy in a particular zenith and azimuth angle (Warren, 1982). Warren and Wiscombe (1981) examined the influence of snow surface contamination. They showed that small amounts of impurities affect snow albedo mainly in the visible ($\lambda < 1\mu\text{m}$) (Warren, 1982). Reductions of visible albedo by a few percent can be caused by approximately 10 parts per million by weight (ppmv) of desert dust or approximately 0.1 ppmv of carbon soot (Warren, 1982). When impurities are present, coarse grain snow demonstrated a greater reduction in albedo than fine-grained snow (Warren, 1982).

4. METHODS

4.1 Grain Size and Wavelength Selection

Grain radii ranges and increments (Δr) selected for in this analysis characterize snow metamorphism under various conditions. A rigorous treatment of snow grain metamorphism will not be addressed in this analysis. We will present for orientation an overview of grain metamorphism in the context of potential satellite sensitivity to changes in near surface snow pack state. For in depth treatment of this subject, see Colbeck (1973, 1979, 1982, 1983, 1986, and 1997). Colbeck (1982) has classified snow grains depending on the dominant process of its metamorphism: Snow is classified as wet or dry depending on whether it is at or below its melting temperature. Dry snow is subdivided into two categories: the crystalline shape characterized as an equilibrium form or as a kinetic growth form. Wet snow is classified depending on the liquid water content as tightly packed grain clusters (low liquid water contents), or well-rounded, cohesionless grains (high liquid water contents, with liquid water completely occupying between grain pore space) (Colbeck, 1982). Snow grains in these categories have variable rates of growth as a function of several factors, including temperature and vapor gradients, liquid water content, grain shape and grain size (Colbeck, 1982). In dry seasonal snow where grain growth proceeds slowly, the rate of grain growth increases markedly when even small quantities of water are added. Grain growth in wet snow (low liquid content between 3-5%) is much greater than isothermal dry snow but much less than liquid-saturated (high liquid water content) wet snow (Colbeck, 1982). During metamorphism, snow grains can occupy a range of sizes. Average grain radii range

for new snow can be 20 – 100 μm , 100 – 300 μm for fine grained older snow, and 1000 – 1500 μm for old snow near the melting point (Warren and Wiscombe, 1981).

We computed modeled reflectance as a function of grain size increments that represent new snow, older snow, as well as snow metamorphism in dry and wet phases. A grain radius of 10 μm was used to represent new snow. This value is below the range for new snow but was used to characterize spectral behavior across the full range of possible grain size radii that could potentially exist in nature. Grain radius of 1000 μm was used to represent old snow at or near the melting point for wet snow at high and low liquid water content. Ice is ten times more absorptive in the near-infrared (mainly between 1.55 and 1.75 μm) than water due to its higher absorption coefficient (imaginary component of refractive index) (Dozier, 1989). Changes in grain radii from 10 μm to 1000 μm , at various increments (10 - 100 μm , 100 - 1000 μm , 10-1000 μm , and 1000 - 1050 μm) were used to represent rapid changes in grain metamorphism common during destruction of small grains and increase in large grain radii in saturated wet snow (Colbeck, 1982). Increments in grain radii of $\Delta 2\mu\text{m}$ for small (10 μm) were used to simulate grain metamorphism under dry snow conditions where small grain radii increase slowly in the absence of a temperature gradient. Under these conditions, small chemical potential differences between grains due to differences in curvature and stress would cause small temperature and vapor pressure differences and slow grain growth through heat and vapor diffusion (Colbeck, 1983). Increments in grain radii of $\Delta 2\mu\text{m}$ for large (1000 μm) were used to simulate grain metamorphism of wet snow under saturated and non-saturated conditions, where growth rates can increase or decrease from saturate to non-saturated conditions as a

function amount of pore-filling liquid water. The amount of liquid water present in pore spaces mediates heat and mass flows among grains. Liquid water slows the growth rate of grain clusters in non-saturated wet snow, but increases individual, suspended grains in saturated wet snow (Colbeck, 1982). Due to the complexities of representation, we ignore simulation scenarios that account for transitional ice morphologies such as

- well faceted, complex crystal structures (derived from kinetic growth),
- multicrystalline grain clusters formed from cycles of freezing and thawing (melt-freeze crystals),
- high density, low porosity, surface and depth melt-freeze layers formed from creation and refreezing of meltwater,
- surface fragments amalgamated to form wind crusts,
- supercooled rainwater that refreeze onto the surface, forming a smooth, impermeable glaze.

A wavelength range between 0.4 and 1.250 μm was selected to encompass the visible and near-infrared bands on TERRA MODIS. Few bands in the visible were designed for land/snow targets and may have a tendency to saturate over snow (bands 8-19), depending on sun-sensor geometry (Thome, 2003 personal communication). In higher wavelength bands, beyond 1.25 μm (MODIS bands 6 and 7), snow has a low response where surface reflectance is approximately 0.1 or less (Wiscombe and Warren, 1981).

Fig. 1 demonstrates modeled reflectance as a function of wavelength for grain radii of 10, 100, and 1000 μm at solar zenith angles of 5 and 60°. The largest change in

reflectance across wavelengths corresponds to larger grain radii as well as higher solar zenith angles.

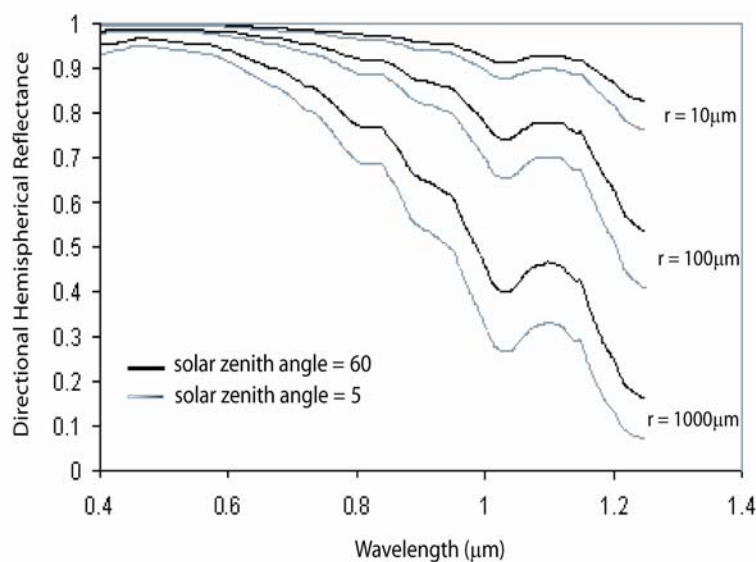


Figure 1: Modeled directional hemispherical reflectance vs. wavelength for grain size radii $10\mu\text{m}$, $100\mu\text{m}$, and $1000\mu\text{m}$ at direct beam incident at a solar angle of 5 and 60 degrees. Modeled reflectance were generated by varying grain and wavelength, assuming spherical grains and using Mie scattering theory to characterize single-grain scattering regime. Figure based on Wiscombe and Warren (1981).

4.2 Simulated At-Satellite Radiance and Band Sensitivity

We converted simulated band-averaged hemispherical reflectance to at-sensor radiance, assuming a Lambertian surface and ignoring downwelling and path radiance contributions (Schowengerdt, 1997). The at-sensor radiance can be approximated by the following expression:

$$L_{\lambda}^0 = (\rho_{m,\lambda} E_{\lambda}^b \tau_s \cos \theta_s / \pi) \cdot \tau_v \quad [2]$$

where:

L_{λ}^0 = simulated at-satellite radiance assuming a horizontal surface [$\text{W} \cdot \text{m}^{-2} \cdot \text{sr}^{-1} \cdot \mu\text{m}^{-1}$]

$\rho_{m,\lambda}$ = simulated directional-hemispherical reflectance

E_{λ}^b = direct solar irradiance [$\text{W} \cdot \text{m}^{-2} \cdot \mu\text{m}^{-1}$]

τ_v = upward atmospheric transmission through view angle

τ_s = downward atmospheric transmission through solar incident angle

θ_s = solar zenith angle

Modeled reflectance was converted to radiance using the above expression for various grain sizes. MODIS band-averaged solar irradiance values, weighted by MODIS band specific normalized spectral response functions, were taken from Thuillier et al.(2003). Atmospheric transmission corresponding to MODIS bands was derived from MODTRAN4 output for a US Standard Atmosphere at 45 degree solar zenith angle and surface pressure of 710 mb.

Variation in simulated at-sensor radiance as a function of grain size has meaning in the context of MODIS sensor performance, through evaluating how a change in received radiance is discriminated from noise: The Noise Equivalent Change in Radiance (NE Δ L), defined as the incremental radiance at wavelength λ required to change the signal level by an amount equal to the noise, was used as a threshold to evaluate MODIS visible/NIR band performance. NE Δ L figures (Table II) were acquired from calibration measurements published in Barnes et al. (1988).

Table II. Band-averaged solar irradiance, atmospheric transmission, typical in-band radiance, estimated NE Δ L for visible and near-infrared MODIS bands.

MODIS Band	Center \dagger λ (nm)	Bandwidth \dagger (nm)	Measured* NE Δ L [W/m ² ·sr· μ m]
8	412	405-420	0.0484
9	443	438-448	0.0317
3	469	459-479	0.1120
10	488	483-493	0.0247
11	531	526-536	0.0183
12	551	546-556	0.0189
4	555	545-565	0.0960
1	645	620-670	0.1304
13	667	662-672	0.0082
14	678	673-683	0.0069
15	748	743-753	0.0095
2	858	841-876	0.0598
16	869	862-877	0.0062
17	905	890-920	0.0296

18	936	931-941	0.0404
19	940	915-965	0.0295
5	1240	1230- 1250	0.0750

† source < <http://modis.gsfc.nasa.gov/about/specs.html>>

* taken from Barnes et al. (1998)

5. RESULTS AND DISCUSSION

Estimated at-sensor radiances for variations in grain size were computed. Several trials were run to determine MODIS visible and NIR band sensitivity to changes in grain size under variable solar zenith angles, diffuse irradiance, and surface slope.

5.1 Simulated At-Sensor Radiance Sensitivity to Grain Size

We computed percent change in radiance for the following changes in grain radii: 10 -100 μm , 100 – 1000 μm , 10 – 1000 μm , and 1000 - 1050 μm (see Figure 2). Percent difference tends to increase with wavelength. The largest percent change in at-sensor radiance was for an increase in grain radius from 10 μm to 1000 μm . The smallest difference was for an increase in radii from 1000 μm to 1050 μm . The greater the Δr , the larger the percent difference in simulated at-sensor radiance.

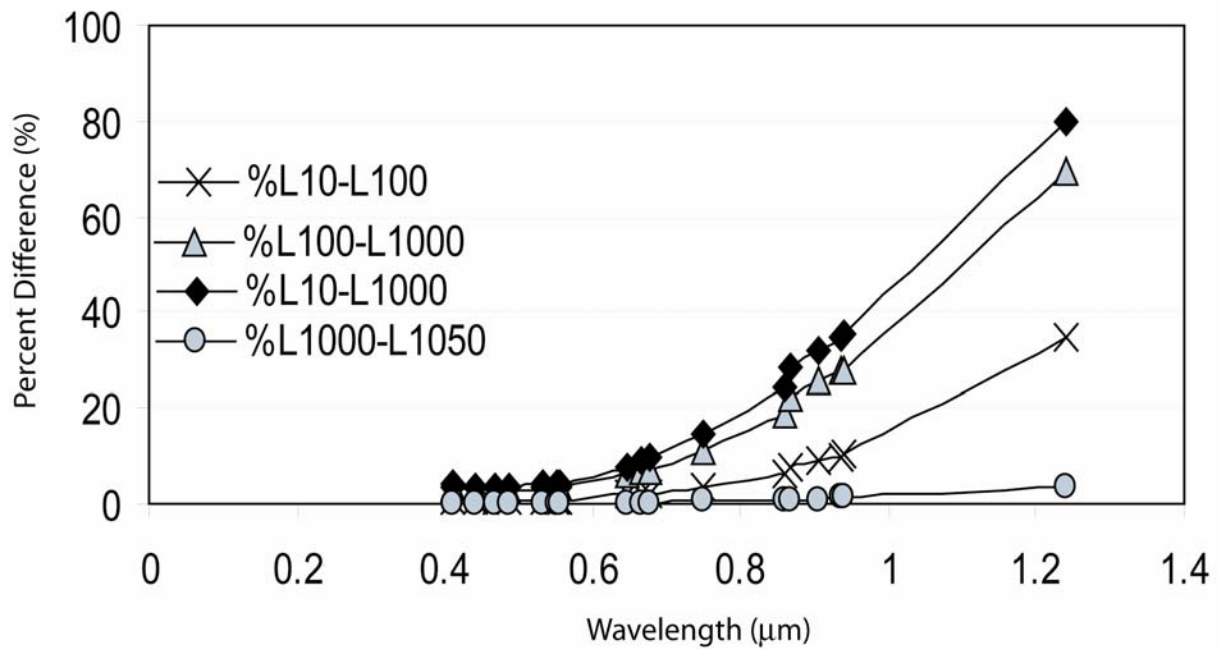


Figure 2: Percent difference between simulated at-sensor radiance vs. wavelength for the following grain size increments: 10 μm -100 μm , 100 μm -1000 μm , 10 μm -1000 μm , and 1000 μm -1050 μm . Differences appear consistently larger for longer wavelengths.

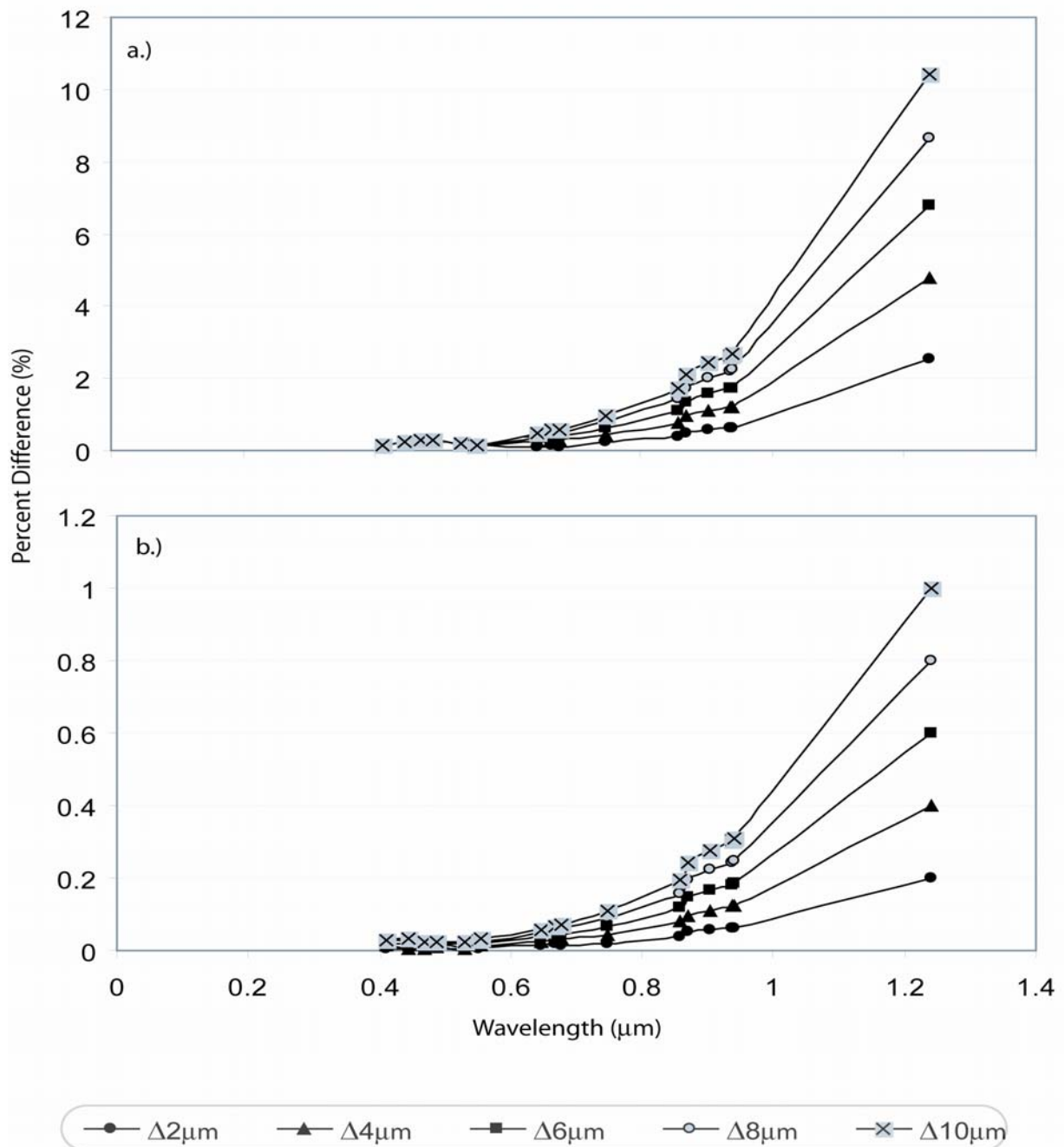


Figure 3: Percent difference between simulated at-sensor radiance vs. wavelength for the following changes in grain size: a.) grain radius ranging from 10 μm to 20 μm at 2 μm increments, b.) grain radius ranging from 1000 μm to 1010 μm at 2 μm increments. The magnitude in percent difference appears to be larger for small grain sizes (10 μm to 20 μm range) than large grain sizes (1000 μm to 1010 μm range).

Differences in at-sensor radiance for changes less than $10\mu\text{m}$ were computed in $2\mu\text{m}$ increments starting at a relatively large grain size of $1000\mu\text{m}$ and a smaller grain size of $10\mu\text{m}$. Figure 3 displays graphs of changes in radiance starting at 10 and $1000\mu\text{m}$. Figures 3(a) and 3(b) show greater differences in radiance for larger changes in grain size. Differences in radiance also increase as wavelength increases. The magnitude in radiance difference was greatest for a grain size increment of $\Delta 10\mu\text{m}$, and $\lambda \sim 1.2\mu\text{m}$ for both a representative large and small grain. The maximum difference of approximately 11% for representative small grain radii ($10\mu\text{m}$) (Figure 3a) was larger than the difference for representative large grain radii ($1000\mu\text{m}$) (Figure 3b) at approximately 1%. Table III provides a summary of band sensitivity as measured by radiance difference greater than $NE\Delta L$ for the following changes in grain radii: 10 - $100\mu\text{m}$, 100 - $1000\mu\text{m}$, 10 - $1000\mu\text{m}$, and 1000 - $1050\mu\text{m}$.

Table III: MODIS Band Sensitivity for variable grain size increments at 10, 100, and $100\mu\text{m}$.

Center λ (nm)	MODIS Band	10- $100\mu\text{m}$	100- $1000\mu\text{m}$	10- $1000\mu\text{m}$	1000- $1050\mu\text{m}$
412	8	▲	▲	▲	-
443	9	▲	▲	▲	-
469	3	▲	▲	▲	-
488	10	▲	▲	▲	-
531	11	▲	▲	▲	▲
551	12	▲	▲	▲	▲
555	4	▲	▲	▲	-
645	1	▲	▲	▲	-

667	13	▲	▲	▲	▲
678	14	▲	▲	▲	▲
748	15	▲	▲	▲	▲
858	2	▲	▲	▲	-
869	16	▲	▲	▲	▲
905	17	▲	▲	▲	▲
936	18	▲	▲	▲	▲
940	19	▲	▲	▲	▲
1240	5	▲	▲	▲	-

▲-percent difference was above NE Δ L threshold

--percent difference was below NE Δ L threshold

Table III suggests that for grain radii increments greater than 50 μ m the MODIS sensor may be capable of distinguishing the resulting at-sensor radiance. At a 50 μ m change in grain size, the bands centered at 412nm, 443nm, 469nm, 488nm, 555nm, 858nm, and 1240nm were unable to discriminate signal from noise, given the change in modeled radiance was below the noise threshold.

Table IV: MODIS band sensitivity to changes in grain size at $2\mu\text{m}$ increments starting at an initial grain radius of $10\mu\text{m}$ and $1000\mu\text{m}$.

Small Grain Size ($10\mu\text{m}$)						Large Grain Size ($1000\mu\text{m}$)				
$\Delta 10\mu\text{m}$	$\Delta 8\mu\text{m}$	$\Delta 6\mu\text{m}$	$\Delta 4\mu\text{m}$	$\Delta 2\mu\text{m}$	Center λ (nm)	$\Delta 2\mu\text{m}$	$\Delta 4\mu\text{m}$	$\Delta 6\mu\text{m}$	$\Delta 8\mu\text{m}$	$\Delta 10\mu\text{m}$
▲	▲	▲	▲	▲	412	-	-	-	-	-
▲	▲	▲	▲	▲	443	-	-	-	-	▲
▲	▲	▲	▲	▲	469	-	-	-	-	-
▲	▲	▲	▲	▲	488	-	-	-	▲	▲
▲	▲	▲	▲	▲	531	-	-	-	▲	▲
▲	▲	▲	▲	▲	551	-	-	-	▲	▲
▲	▲	▲	▲	▲	555		-	-	-	-
▲	▲	▲	▲	▲	645	-	-	-	-	-
▲	▲	▲	▲	▲	667	▲	▲	▲	▲	▲
▲	▲	▲	▲	▲	678	▲	▲	▲	▲	▲
▲	▲	▲	▲	▲	748	▲	▲	▲	▲	▲
▲	▲	▲	▲	▲	858		-	-	-	▲
▲	▲	▲	▲	▲	869	▲	▲	▲	▲	▲
▲	▲	▲	▲	▲	905	-	▲	▲	▲	▲
▲	▲	▲	▲	▲	936	▲	▲	▲	▲	▲
▲	▲	▲	▲	▲	940	-	▲	▲	▲	▲
▲	▲	▲	▲	▲	1240	-	-	-	-	-

▲-percent difference was above NE Δ L threshold

--percent difference was below NE Δ L threshold

Table IV presents bands that exhibit sufficient sensitivity to small changes in grain size starting at an initial grain size radius of $10\mu\text{m}$ and $1000\mu\text{m}$. Table IV demonstrates that changes in a representative small grain size ($10\mu\text{m}$) is detectable by every visible/NIR band. There was greater variation in band sensitivity for a representative large ($1000\mu\text{m}$) grain size: Longer wavelengths, specifically 667nm , 678nm , 748nm , 869nm , and 936nm were the most sensitive to the smallest grain size increment ($\Delta 2\mu\text{m}$) considered in this analysis. Band sensitivity increases with an increase in λ , as grain size increments were increased. Shorter wavelength bands did not demonstrate sufficient sensitivity until grain radii were changed by $8\mu\text{m}$. At a $\Delta 10\mu\text{m}$, short wavelength bands centered at 443nm , 488nm , 531nm , and 551nm (coarse resolution of 1000m) were sufficiently sensitive.

5.2 Simulated At-Sensor Radiance Sensitivity to Solar Zenith Angle

The effect of solar zenith angle was explored by modeling changes in simulated at-sensor radiance as a function of grain size for the following solar zenith angles (θ_s): 0° , 20° , 40° , and 60° . Grain size increments used to derive simulated at-sensor radiance were $10\text{-}100\mu\text{m}$, $100\text{-}1000\mu\text{m}$, and $10\text{-}1000\mu\text{m}$ for each solar zenith angle. Figure 4 depicts the relationship between percent difference in modeled at-sensor radiance vs. wavelength for various solar zenith angles. Figure 4(a) shows changes in simulated radiance from a representative grain radius of $10\mu\text{m}$ to $100\mu\text{m}$ at the various solar zenith angles. As λ increases, so does the percent difference. The larger difference occurs for a nadir solar zenith angle (i.e. $\theta_s = 0^\circ$), while the largest for $\theta_s = 60^\circ$. Figure 4(b) and 4(c) demonstrate the same trend, where percent difference increases with increasing

wavelength and the largest difference occurs for nadir solar zenith angle. Figure 4 suggests the difference in simulated at-sensor radiance is larger for a change in grain radius from 10-1000 μm . Additionally, the figure suggests that a variation in solar zenith angle has a greater impact on changes in larger grains (100-1000 μm) than smaller (10-100 μm) where the average difference in modeled radiance for the 100-1000 μm case was approximately 23 ($\text{W}\cdot\text{m}^{-2}\cdot\text{sr}^{-1}\cdot\mu\text{m}^{-1}$) and 6 ($\text{W}\cdot\text{m}^{-2}\cdot\text{sr}^{-1}\cdot\mu\text{m}^{-1}$) for the 10-100 μm . Difference in modeled at-sensor radiance for the three grain size increments all were above the NEAL threshold for each sol

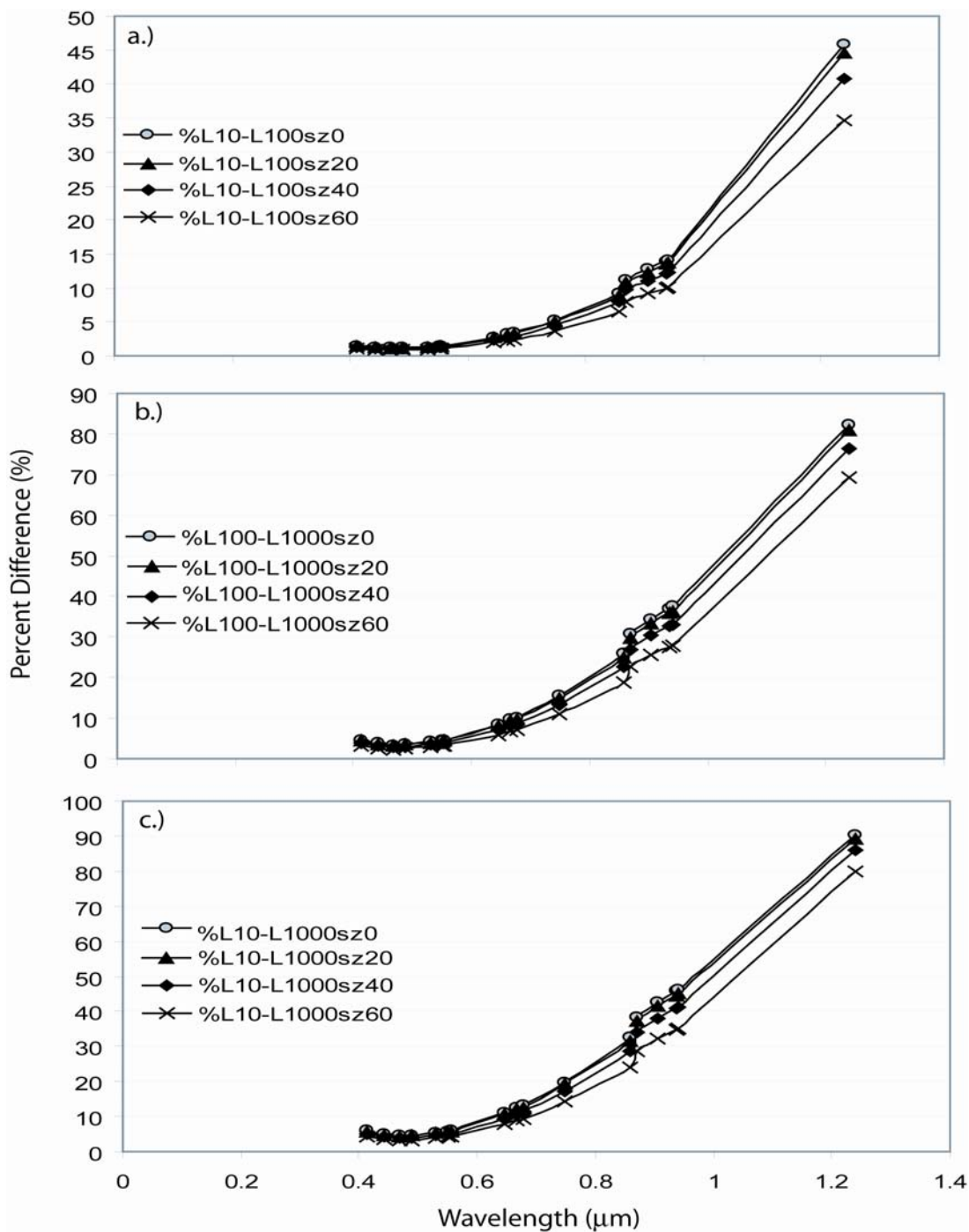


Figure 4: Percent difference between simulated at-sensor radiance vs. wavelength for grain size increments as a function of solar zenith angle. Solar zenith angles (θ_s) range between 0° to 60° at 20° increments: a.) $10\mu\text{m}$ - $100\mu\text{m}$, b.) $100\mu\text{m}$ - $1000\mu\text{m}$, c.) $10\mu\text{m}$ - $1000\mu\text{m}$. Differences appear consistently larger for longer wavelengths. The largest difference for all grain size increments occur at $\theta_s = 0$ (nadir).

5.3 Simulated At-Sensor Radiance Sensitivity to Diffuse Irradiance

The WWM enables calculation of directional hemispherical reflectance for any given ratio of diffuse to direct solar incidence. We examined the effect of increased diffuse irradiance through varying the diffuse/direct ratio for 10%, 50%, and 100% diffuse irradiance. Figure 5 illustrates percent difference in modeled at-sensor radiance for the 10-100 μm , 100-1000 μm , and 10-1000 μm change in grain radii for variable diffuse irradiance. For all three cases of percent diffuse irradiance, there is a consistent increase in percent difference as λ increases. Diffuse irradiance has a greater affect on larger grain size increments (10-1000 μm) with an average difference (for $0.4\mu\text{m} < \lambda < 1.2\mu\text{m}$) of ~ 1.5 ($\text{W}\cdot\text{m}^{-2}\cdot\text{sr}^{-1}\cdot\mu\text{m}^{-1}$). In contrast, average difference of a 10-100 μm was only ~ 0.5 ($\text{W}\cdot\text{m}^{-2}\cdot\text{sr}^{-1}\cdot\mu\text{m}^{-1}$). The overall magnitude of difference in modeled at-sensor radiance demonstrates that the effect of diffuse irradiance may not be substantial across the range of increments considered in this analysis. Difference in modeled at-sensor radiance for all three grain size increments were above the NE Δ L threshold for each diffuse irradiance case.

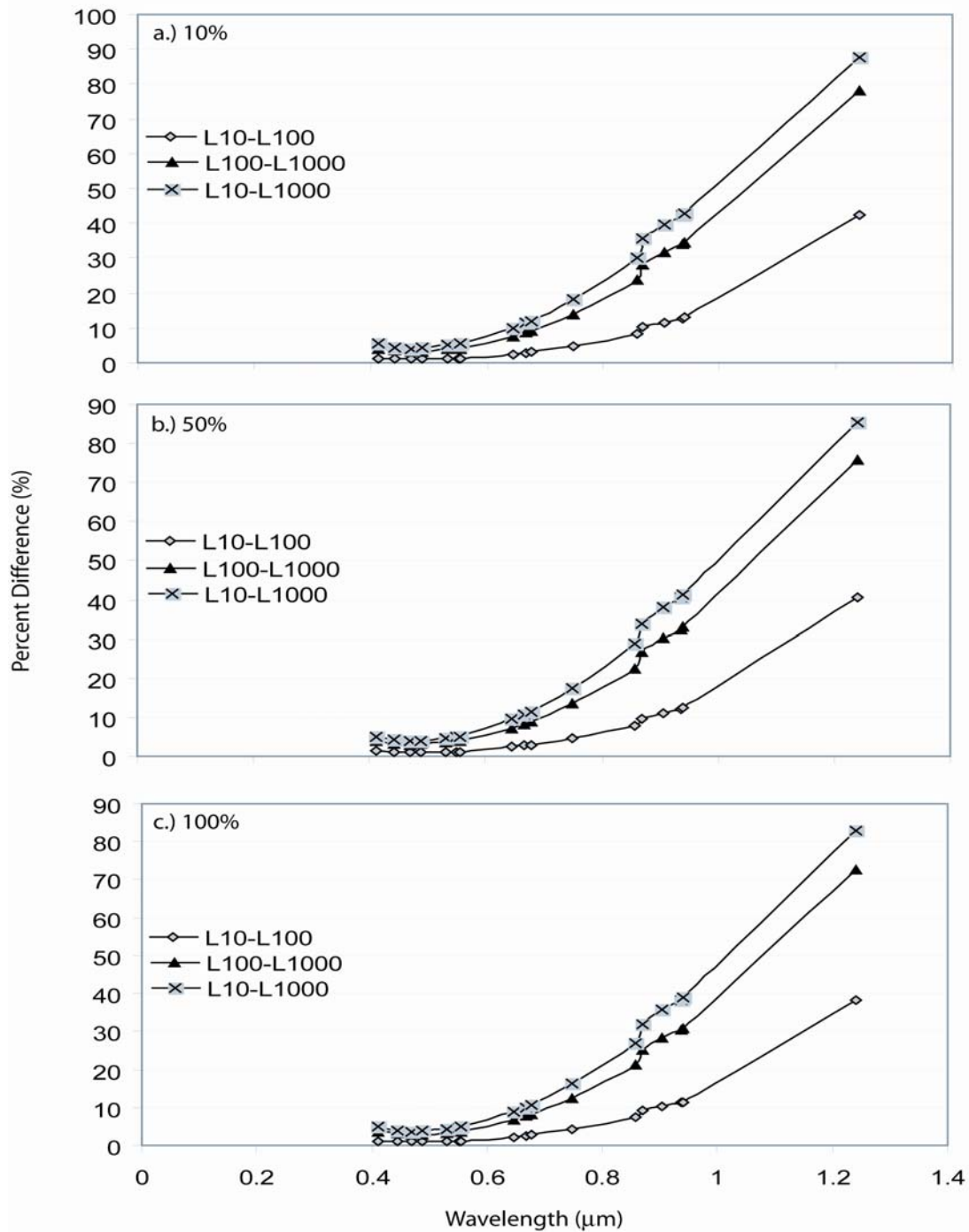


Figure 5: Percent difference between simulated at-sensor radiance vs. wavelength for grain size increments at variable diffuse/direct solar irradiance ratio. Percent diffuse irradiance ratios are at 10%, 50%, and 100%: a.) 10 μm -100 μm , b.) 100 μm -1000 μm , c.) 10 μm -1000 μm . Differences appear consistently larger for longer wavelengths. Diffuser irradiance has a greater affect on larger grain size increments.

5.4 Simulated At-Sensor Radiance Sensitivity to Local Surface Slope

We attempted to account for the influence of complex mountain terrain through varying the local surface slope in deriving simulated at-sensor radiance. Ideally, sloped terrain will cause different radiance values observed by the satellite sensor according to the angle of incidence and the amount of sky illumination (Teillet, et al., 1982).

Assuming a Lambertian surface and ignoring multiple reflection due to surrounding slopes we used the following expression for correcting for variable slope angles (α) at 5, 10, 15, 20, 25, and 30° for a fixed solar azimuth angle (Φ_s) of 135° and a surface azimuth angle (Φ') of 90°:

$$L_{\lambda}^s = L_{\lambda}^0 \cdot (\cos(i) / \cos(\theta_s)) \quad (\text{Teillet et al., 1982}) \quad [3]$$

where:

$$\cos(i) = \cos \theta_s \cos \alpha + \sin \theta_s \sin \theta_s \cos(\Phi_s - \Phi')$$

L_{λ}^s = simulated at-satellite radiance assuming variable surface slope [$\text{W} \cdot \text{m}^{-2} \cdot \text{sr}^{-1} \cdot \mu\text{m}^{-1}$]

Results indicate very small differences in derived simulated at-sensor radiance for 10-100 μm , 100-1000 μm , and 10-1000 μm at variable slope angles. For example, the average difference in modeled at-sensor radiance (for $0.4\mu\text{m} < \lambda < 1.2\mu\text{m}$) for the 10-100 μm change in grain radius is about 1.6 ($\text{W} \cdot \text{m}^{-2} \cdot \text{sr}^{-1} \cdot \mu\text{m}^{-1}$). Percent difference for the grain radii increments mentioned above suggest surface slope effects are negligible. This is certainly not true. This first-order model may be inadequate to quantify terrain effects

due to the Lambertian assumption and lack of provisions for snow BRDF. Results indicate that all MODIS visible/NIR bands may be sensitive to changes in grain radii for variable surface slopes given modeled at-sensor radiance differences were above band NEAL thresholds.

Variations in MODIS band sensitivity indicate many of the visible and near-infrared bands may have the potential for monitoring changes in snow pack grain size, particularly for changes greater than $10\mu\text{m}$. At $\Delta 10\mu\text{m}$, wavelength bands greater than 662nm appeared useful, possibly because these bands have larger instantaneous fields of view (IFOV) than those bands shorter than 662nm . A larger area increases the radiant energy collected over the ground and compensates for reduced energy in the longer wavelengths. Greater atmospheric attenuation due to dominant Rayleigh scattering in the shorter wavelength bands could contribute to reduced at-sensor radiance in these bands, thereby reducing band sensitivity. At $\Delta 50\mu\text{m}$, bands centered at 469nm and 555nm were insensitive. These two bands have a 500m IFOV, while maintaining a narrower bandwidth (at 20nm). The band centered at 645nm was more sensitive than 469nm and 555nm bands. The 645nm band had a 60% larger bandwidth than both 469nm and 555nm bands. This increase in bandwidth was greater than the difference in energy at 469nm vs. 645nm . Using Planck's distribution for radiant exitance and assuming the sun is a black body at a temperature of 6000 Kelvin , we determined there was 16% more energy at the center wavelength for 469nm than 645nm . The impact of an increase in IFOV was thus more influential than the difference in energy as a function of wavelength.

Results showed MODIS visible/NIR bands were sufficiently sensitive to small changes in grain size: Bands longer than 645nm at an IFOV of 1000m were able to detect the smallest increment in grain size ($\Delta 2\mu\text{m}$). For grains less than 1000m, sensitivity decreased to about a $\Delta 6\mu\text{m}$. At an $8\mu\text{m}$ change in grain size, bands with wavelengths less than 645nm at 1000m IFOV become sufficiently sensitive. Longer wavelength bands with large IFOV show significant sensitivity. There was an increase in sensitive bands with an increase in grain radius. At a change in grain radius of $10\mu\text{m}$, band 10 (488nm) was the shortest wavelength band above the NE Δ L threshold. Therefore, increments in large grain sizes, IFOV controls band sensitivity over wavelength, whereas for increments in small grains band wavelength dominates band sensitivity.

At visible wavelengths, ice particles are strongly forward scattered and increases slightly with wavelength (Diner et al., 1999). Results from this analysis failed to account adequately for the influence of local surface slope. The model inaccurately treats ice particles as Lambertian reflectors and ignores snow BRDF. This could contribute to the lack of model sensitivity to surface slope variations. It is known that failure to account for snow BRDF can cause errors as large as 50% in outgoing flux, particularly at large viewing zenith angles (Diner et al., 1999).

Snow grains increase in size due to aging and the onset of melt (Warren, 1982). This process can cause a subsequent decrease in albedo. Larger grains are both more absorptive and more forward scattering than smaller grains. For $\lambda < 2.5\mu\text{m}$, decreases in albedo are due to a decrease in single-scattering albedo and an increase in the asymmetry factor (Wiscombe and Warren, 1981). The single-scattering albedo is the ratio of the extinction cross section to the geometric cross section and probability that a photon is

intercepted by a particle. Accordingly, the single-scattering albedo of large grains will be scattered initially, increasing the probability for absorption. The probability increases significantly with increasing wavelength (see Figure 6a)(Wiscombe and Warren, 1981). An increase in the asymmetry factor (a measure of the direction of scattered energy) has less of an influence than single-scattering albedo. This phenomenon is demonstrated in figure 6b, which plots the asymmetry factor as a function of wavelength for a grain radius of 1000um. The magnitude of increase in forward scattering, as indicated by the asymmetry factor, is far less than the magnitude of decrease in single scattering albedo for large grains. Effectively, there is less energy reflected to the sensor, when snow grains become increasingly large, thereby reducing the differential amount of at-sensor radiance.

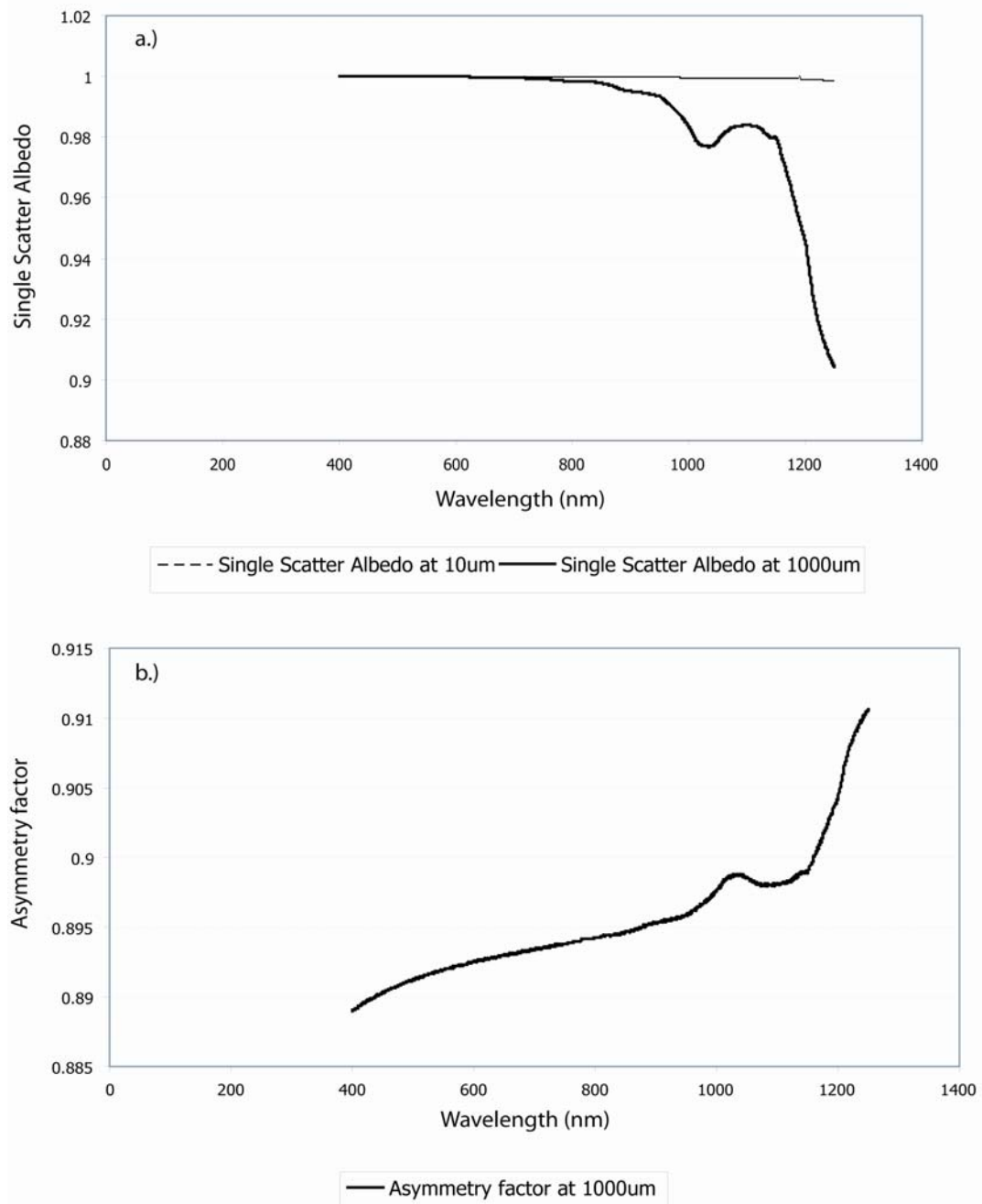


Figure 6: a.) Single-scatter albedo for 10µm and 1000µm grain size as a function of wavelength; b.) asymmetry factor for 1000µm grain size as a function of wavelength in the visible and near-infrared regions of the electromagnetic spectrum. The magnitude of increase in the forward scattering direction as indicated by the asymmetry factor, as the wavelength increases, is far less than the decline in single scattering albedo for large grains. Therefore, as snow grains become increasingly large there will be less energy reflected to the sensor due to an increase in the probability of absorption.

6. CONCLUSION AND RECOMMENDATIONS

First-order simulation results demonstrate MODIS visible/NIR bands may have adequate sensitivity to detect mountain snow pack ripeness. Longer wavelength bands had greater sensitivity to large changes in grain sizes, especially those bands with larger IFOV. These bands showed greater sensitivity to small increments in smaller grains than to small changes in larger grains. Shorter wavelength bands with small IFOV (500m) appear less effective overall for monitoring ablating snow packs. In nature, average grain radii for new snow falls in the range 20-100 μm , 100-300 μm for fine grained snow, and 1.0-1.5mm for old snow near the melting point (Wiscombe and Warren, 1981). The small grain size of 10 μm used in this analysis falls outside those found in nature, but our results indicated that large increments in grain radii could be monitored using MODIS and used to indicate the condition of the snow surface. Further study is needed to determine the smallest change in grain size each band is capable of resolving using actual sensor measurements of snow surface radiances during ablation events. Improve simulations by including assessment of the full surface irradiance, snow surface BRDF, considering the affect of surface impurities, and improve corrections for atmospheric effects. This may be accomplished through the use of a GIS –based radiative transfer model or the discrete-ordinate radiative transfer model (DISORT) (Stamnes et al., 1988) , which is capable of producing directional spectral reflectance allowing specification of illumination and observation angles (Green et al., 2002). We will examine potential of satellite sensor performance for monitoring shallow snowpacks and saturated wet snow surfaces. Additional work should be done to explore other sensors such as AVHRR for potential in monitoring snow surface dynamics. Future work will involve development

of an algorithm to monitor changes in the timing, and spatial distribution of snow melt in vegetated mountainous terrain, using MODIS (TERRA and AQUA) daily reflectance and surface temperature.

Acknowledgments. This study was supported by NASA Headquarters under the Earth System Science Fellowship (ESS) Grant NGT5. I would like to thank Dr. Kurtis Thome and Dr. Chris Catrall at University of Arizona's Remote Sensing Laboratory for their support as well as Dr. Ann Nolin at Oregon State University for her valued feedback. Additionally, I'd like to thank the anonymous reviewers for their time and constructive suggestions, which resulted in a superior manuscript. I would also like to thank Dr. Fassnacht for his thoughtful suggestions and support and Dr. Tim Warner for his patience as well.

REFERENCES

- Barnes, W.L., T.S. Pagano, and V. Salomonson. 1998. Prelaunch characteristics of the moderate resolution imaging spectroradiometer (MODIS) on EOS-AM1. *IEEE Trans. Geosci. Remote Sensing*. Volume 36, No. 4, pp1088-1100.
- Colbeck, S.C. 1973. Theory of metamorphism of wet snow. Cold Regions Research and Engineering Laboratory Report 313.
- Colbeck, S.C. 1979. Grain clusters in wet snow. *J. Colloid Interface Sci.*, Volume 72, No. 3, pp371-384.
- Colbeck, S.C. 1982. An overview of seasonal snow metamorphism. *Review of Geophysics and Space Physics*, Volume 20., No. 1, pp45-61.
- Colbeck, S.C. 1983. Theory of metamorphism of dry snow. *Journal of Geophysical Research*, Volume 88, No. C9 pp5475-5482.
- Colbeck, S.C. 1986. Statistics of coarsening in water-saturated snow. *Acta metal.*, Volume 34, No. 3, pp347-352.
- Colbeck, S.C. 1989. Snow-crystal growth with varying surface temperatures and radiation penetration. *J. Glaciol.*, Volume 35, no. 119, pp 23-29.

Colbeck, S.C. 1997. A review of sintering in seasonal snow. Res. Rep. 97-10. U.S. Army Cold Reg. Res. and Eng. Lab., Hanover, N.H.

Davis, R.E., A.W. Nolin, R. Jordan, J. Dozier. 1993. Towards predicting temporal changes of the spectral signature of snow in visible and near-infrared wavelengths. *Annals of Glacio.*, Volume 17, pp 143-148.

Diner, D.J., G.P. Asner, R. Davies, Y. Knyazikhin, J.P. Muller, A.W. Nolin, B. Pinty, C.B. Schaaf, and J. Stroeve. 1999. New directions in earth observing: scientific applications of multiangle remote sensing. *Bulletin of Amer. Met. Soc.*, Volume 80, No. 11, pp2209-2228.

Dozier, J. 1989. Spectral signature of alpine snow cover from the Landsat Thematic Mapper. *Remote Sens. Environ.*, 28, 9-22.

Dozier, J., and S.G. Warren. 1982. Effect of view angle on the infrared brightness temperature of snow. *Water Resources Research*, Volume 18, No. 5, pp1424-1434.

Dozier, J., S. R. Schneider, and D.F. McGinnis. 1981. Effect of grain size and snowpack water equivalence on visible and near-infrared satellite observations of snow. *Water Resour. Res.*, vol(17), no. 4. pp1213-1221.

El-Ashry, M. and D. Gibbons. 1988. *Water and arid lands of western United States*, Cambridge Univ. Press, New York.

Green, R.O., and J. Dozier. 1996. Retrieval of surface snow grain size and melt water from AVIRIS spectra. In 1996 Airborne Geoscience Workshop. Pasadena, CA. Jet Propulsion Laboratory, pp 127-134.

Green, R.O., J. Dozier, D.A. Roberts, and T.H. Painter. 2002. Spectral snow reflectance models for grainsize and liquid water fraction in melting snow for the solar reflected spectrum. *Annals of Glaciology*, 34, 71-73.

Hansen, J.E. 1971. Multiple scattering of polarized light in planetary atmospheres, 2, sunlight reflected by terrestrial water clouds, *J. Atmos. Sci.*, Volume 28, pp 1400-1426.

Liou, K.N. 2002. *An Introduction to atmospheric radiation 2nd edition*. Academic Press, International Geophysics Series, Volume 84.

Mie, G. 1908. Beitrage zur optic truber medien, speziell kolloidaler metallosungen. *Annalen der Pjysik*, Volume 25, 377-445.

Nolin, A.W., and J.C. Stroeve. 1997. The changing albedo of the Greenland ice sheet: implications for climate modeling. *Ann. Glaciol.*, Volume 25, pp51-57.

Nolin, A.W. 1998. Mapping the martian polar ice caps: applications of terrestrial optical remote sensing methods. *Journal of Geophysical Research*, Volume 103, No. E11, pp25,851-25,864.

Nolin, A.W., and J. Dozier. 2000. A hyperspectral method for remotely sensing the grain size of snow. *Remote Sensing of Environment*, 74(2), 207-216.

Painter, T.H., J. Dozier, D.A. Roberts, R.E. Davis, R.O. Green. 2003. Retrieval of subpixel snow-covered area and grain size from imaging spectrometer data. *Remote Sensing of Environment*, 85 (2003), 64-77.

Rango, A. 1993. *II. Snow hydrology and remote sensing*. Hydrological Processes, Volume 7, pp 121-138.

Rott, H. 1987. Remote sensing of snow in *Large Scale Effects of Seasonal Snow cover*, Proceedings of the Vancouver Symposium, August 1987. IAHS Publ. no. 166.

Schowengerdt. 1997. *Remote sensing: models and methods for image processing 2nd* edition. Academic Press.

Schultz, G.A., E.T. Engman. 2000. *Remote Sensing in hydrology and water management*. Springer.

Steppuhn, H.1981. Snow and agriculture. In Gray, D.M. and Male, D.H. (Eds.).1982. *Handbook of snow:principles, process, management and use*. Pergamon Press, Toronto.

Teillet, P.M., B. Guindon, and D.G. Goodenough. 1982. On the slope-aspect correction of multispectral scanner data. *Canadian Journal of Remote Sensing*, Volume 8, No. 2, pp84-105.

Thuillier, G., M. Herse', D. Labs, T. Foujols, W. Peetermans, D. Gillotay, P.C. Simon, and H. Mandel. 2003. The solar spectral irradiance from 200 to 2400 nm AS measured by the SOLSPEC spectrometer from the ATLAS and EURECA missions. *Solar Physics*, Volume 214, pp1-22.

Warren, S.G.1982. Optical properties of snow. *Rev Geophys. Space Phys.* 20:67-89.

Wiscombe, W.J., and Warren, S.G.1981. A model for the spectral albedo of snow I: Pure snow. *J. Atmos. Sci.*, 37:2712-2733.

Appendix C

Monitoring Mountain Snow Pack Evolution Using Near Surface Optical and Thermal Properties

**MONITORING MOUNTAIN SNOW PACK EVOLUTION USING NEAR
SURFACE OPTICAL AND THERMAL PROPERTIES**

D.J. Lampkin and S.R. Yool
Department of Geography and Regional Development
The University of Arizona
Tucson, AZ 85721
Phone: 520-626-8523
Fax: 520-621-1422
Email: dlampkin@hwr.arizona.edu

ABSTRACT

A Near Surface Moisture Index (NSMI), which models relative moisture through construction of a feature space using visible band and a thermal band was developed to track the evolution of spring snow melt potentially from MODIS. A simple analytical radiative transfer model for computing directional hemispherical reflectance and emissivity derived from the delta-eddington approximation to the equation of radiative transfer was used to produce the NSMI. Modeled reflectance and emissivity, as a function of grain size, were used to produce the NMSI feature space constructed from the Normalized Difference Snow Index (NDSI) on the abscissa and brightness temperature (T_b) on the ordinate. As grain size increases, the dynamic range or sensitivity of NDSI is reduced, with saturation occurring approximately around 400-450 μm grain radius. T_b for various grain sizes at fixed kinetic temperatures between 245, and 273 Kelvin and NDSI as a function of grain size were used to construct simulated NSMI. Cold Land Processes Experiment (CLPX) field measurements of surface wetness, surface/near surface grain size, average pack temperature and surface temperature for late February and March in Fraser, Colorado were correlated with measured NSMI using a March 4, 2002 scene from Advanced Spaceborne Thermal Emission and Reflection Radiometer (ASTER) as validation of simulated NSMI. Ground-based measurements indicate significant changes in snow surface properties, representing a warming pack across three ISA's from February to March. Similar behaviors are reflected in changes in average pack temperatures. Surface and average pack temperatures in March were warmer for all three sites, with the St. Louis ISA having the warmest temperatures, near 0° C. ASTER

measured reflectance and surface brightness temperature (T_b) were sampled from each ISA and used to construct an NMSI. Lower elevation ISA (St. Louis Creek) demonstrated higher mean T_b and lower mean NDSI while the higher elevation ISA (Alpine) showed higher mean NDSI and lower mean T_b. ASTER derived NSMI demonstrated behavior consistent with simulations with deviations due to topography, vegetation, and regional heterogeneity.

1. INTRODUCTION

To understand impacts of climate variability on water resources, we must monitor the temporal and spatial variability of snow cover characteristics from local to global scales. Continuous monitoring of temporal and spatial variability in snow cover is needed to address complex relationships among seasonal forested canopy snow cover, climate, and water resources (Dozier, 1989). Snow stores at least one third of the water used for crop irrigation worldwide (Steppuhn, 1981). Variability in regional climate affects snow covered area, amount, and timing of yields. Monitoring snow cover is important particularly in the semi-arid western United States, where annual water consumption averages 44% of renewable supplies, compared to 4% in the rest of the country (El-Ashry and Gibbons, 1988). Snow typically changes how drainage basins respond to the input of water; moreover, water stored as snow enters the basin over an extended period of time (Schultz and Engman, 2000).

In the last 20 years remote sensing research has led to significant progress in monitoring and measuring certain snow hydrologic processes: In particular, estimating the timing of snowmelt run-off can be improved by monitoring when the snowpack is primed for run-off. Remote sensing provides a rough estimate of melt by monitoring the snow pack in the early spring (Rango, 1993). New NASA technology aboard the TERRA Earth Observing System (EOS) platform launched December 1999 spanning the solar reflective visible (0.4-0.7 μm), Near Infrared (NIR) (0.7-1.3 μm), Shortwave Infrared (SWIR) (1.3-3 μm), and thermal infrared (3-14 μm) regions of the electromagnetic spectrum (EM), may improve snow pack measurements: The Moderate Resolution Imaging Spectroradiometer (MODIS), and the Advanced Spaceborne Thermal

Emission and Reflection Radiometer (ASTER) are both operational aboard TERRA. . The MODIS sensor was designed to test new technology and provide a context for the development of improved products for earth science research. MODIS capacity to acquire data every 1-2 days, with spatial resolutions at 250, 500, and 1000 meters and 36 bands, makes it useful for monitoring snow cover dynamics. ASTER has improved spatial resolutions that are wavelength dependent; the visible/NIR bands have a spatial resolution of 15m, SWIR is 30m, and Thermal Infrared is 90m and 14 bands from 0.5-11.6 μ m.

This study is an initial examination of a surface moisture index to infer snow pack ripeness conditions using optical remote sensors. We are particularly interested in the utility of operational monitoring of mountain snow surface melt using MODIS. Using the delta-Eddington approach to characterize a theoretical Near Surface Moisture Index Space (NSMI), we modeled the radiative transfer of snow reflectance and brightness temperature as a function of grain size using visible, SWIR, and thermal MODIS bandpasses. Due to its improved spatial resolution, an ASTER scene acquired on March 4, 2002 was used to construct a satellite measured NSMI as validation. We correlated NMSI values with Cold Land Processes Experiment (CLPX) field measurements in North-Central Colorado for snow pack characteristics such as surface wetness, surface/near surface grain size, average pack temperature and surface temperature for late February and March.

2. BACKGROUND

Once seasonal snow cover has been established in a basin, snow undergoes various transformations: The snowpack changes rapidly in spring, reaching an isothermal state at 0°C and satisfying the snowpack liquid water holding capacity (Rango, 1993). When these two conditions have been met, the snowpack is ripe and absorption of additional energy will induce snowmelt (Rango, 1993). As melt progresses, liquid water entrained within the pack matrix tends to increase grain size. Grain clusters form causing a decline in snow surface reflectance (Davis et al., 1993). Nolin and Stroeve (1997) demonstrated the relationship between snowpack energy balance, grain growth, and albedo: Nolin (1998) used a one-dimensional model of snowpack energy and mass balance to calculate grain growth and that output was then used to drive a radiative transfer model that calculated spectral albedo at each time step. Changes in energy balance were seen to strongly affect albedo through grain growth, especially during periods of snowpack warming. These data show that in the near-infrared wavelengths, albedo dropped nearly 20% during a 10-day period during which grain sizes increased significantly (Nolin, 1998).

Work has been done to extract and monitor snow melt and snowpack depletion water using satellite measurements. Landsat Thematic Mapper (TM) has been used to monitor snow cover depletion. Landsat operates at 30m² nominal spatial resolution, a 16-day repeat acquisition interval, and has adequate spectral capabilities for mapping snow cover due to its strong contrast with snow-free regions (Rango et al., 2000). Landsat TM has poor repeat coverage relative to the rate of depletion of snow cover (Rango et. al., 1983). The Advanced Very High Resolution Radiometer (AVHRR) has

also been used to monitor depletion of snow cover. AVHRR has a nominal spatial resolution of 1.1km^2 , limiting applicability to basins with a minimum area of 200 km^2 - but has improved repeat coverage over TM with two acquisitions a day (daytime and night time) (Rango et. al., 1983). Rango et. al. (1983) used combined Landsat TM and AVHRR to derive modeled snowmelt runoff curves for the King's River basin in California.

Using the delta-Eddington approximation to the equation of radiative transfer, Dozier et al. (1981) examined the impact of grain size and snow pack water equivalence on snow reflectance in the visible and NIR regions of the EM spectrum. The delta-Eddington approach decomposes the equation of radiative transfer into orthogonal Legendre polynomials, and is designed to handle strongly forward-directed scattering media such as snow (Liou, 2002). Examination of AVHRR visible and NIR signatures acquired over transects in Canada demonstrated satellite observations could be used to detect the presence of surface melt (Dozier et al., 1981). In particular, modeled reflectance showed optimal sensitivity to changes in snow surface grain size between $1\mu\text{m}$ and $1.2\mu\text{m}$, extending to about $1.4\mu\text{m}$ (Dozier et al., 1981). Green and Dozier (1996) used a discrete-ordinate approximation of the radiative transfer equation to model snow as a mixture of ice and liquid water sphere. Modeled spectra as a function of grain size and liquid water content were fit against spectra acquired from the Airborne Visible/Infrared Imaging Spectrometer (AVIRIS) Mammoth Mountain data set in California. Results indicate grain size and melt water retrievals were consistent with the range of elevations and temperatures for the data (Green and Dozier, 1996). Snow melt estimates were high in vegetated regions due to the presence of liquid water in the leaves

(Green and Dozier, 1996). Nolin and Dozier (2000) retrieved snow grain size from near-infrared AVIRIS data using an inversion technique that relates an ice absorption feature centered at $1.03\mu\text{m}$ to an optically equivalent snow grain size. This technique requires, however, that pixels be completely snow covered, have less than 1% litter by weight on the surface, and that the sensor carry sufficiently high spectral resolution to resolve the absorption feature (Nolin and Dozier, 2000). Painter et al. (2003) used AVIRIS to retrieve sub-pixel snow-covered area and grain size using the multiple end-member snow-covered area and grain size (MEMSCAG) algorithm. MEMSCAG maps sub-pixel snow cover and grain size simultaneously using spectral mixture analysis coupled with radiative transfer modeling of snow spectra (Painter et al., 2003). MEMSCAG had a 4% root mean square error for snow-covered area, compared to snow area determined with high resolution photographs. For grain radii ranging from 80 to $750\mu\text{m}$, MEMSCAG had a RMSE of $74\mu\text{m}$ for a mean of 3 x 3-pixel AVIRIS window (Painter et al., 2003). Despite superior spatial detail, airborne sensors such as AVIRIS often lack the necessary coverage to monitor snow cover in mountain basins spanning several degrees of latitude. Airborne systems collect data on a per request basis, rendering them insufficient for *operational* monitoring of snow cover.

3. THEORY AND MODEL

3.1 Modeled Near Surface Moisture Index (NSMI)

Spectral data about the optical and thermal response of near surface snowpack during melt may be used in an integrated approach for tracking snowmelt. The Near Surface Moisture Index (NSMI) for snow is a feature space using optical and thermal variables to characterize the state of the snowpack. This approach borrows from Nemani et al. 1993, in which they construct a feature space of Normalized Difference Vegetation Index (NDVI) vs. surface temperature, to monitor vegetation moisture. In this analysis we develop a modeled NMSI for monitoring changes in snow surface moisture constructed from a feature space defined by the Normalized Difference Snow Index (NDSI) and surface brightness temperature.

Brightness temperature (T_b) instead of thermodynamic surface temperature (T) was used because it could be easily modeled using the Dozier and Warren (1982) radiative transfer model, which will be explained later. Additionally, since snow can be considered a near black-body, where modeled snow emissivity is close to 1 for wavelengths in the visible, NIR, and SWIR and snow temperatures in the mid-latitudes between 250-273 K (Dozier and Warren, 1982), then the use of T_b is not an unreasonable. NDSI was used instead of NDVI because it is known to be sensitive to the spectral variation of snow as opposed to other land cover materials. Dozier and Marks (1987) initially derived NDSI using TM data to discriminate snow from other land surface materials. Independent of a sensor, NDSI can be expressed as:

$$\text{NDSI} = (\text{Visible Band} - \text{SWIR Band}) / (\text{Visible Band} + \text{SWIR Band}) \quad [1]$$

Dozier and Marks (1987) used TM band 2 (0.53-0.61 μm) as the visible band and band 5 (1.57-1.78 μm) as the SWIR band. NDSI is based on snow and ice high visible reflectance and low SWIR reflectance (Riggs et al., 1994). Dozier (1989) proposes the use of NDSI as a grain size sensitive index. Dozier (1989) also indicate that an NDSI derived from using TM band 4 (0.78-0.90 μm) instead of band 5 would produce an index sensitive to grain sizes where higher index values represent larger grains. Figure 1 displays theoretical snow spectra for fine and coarse grain snow from 0.4 to 2.5 μm , which indicates a significant decrease in visible and SWIR reflectance as grain size increases. This effectively would decrease NDSI.

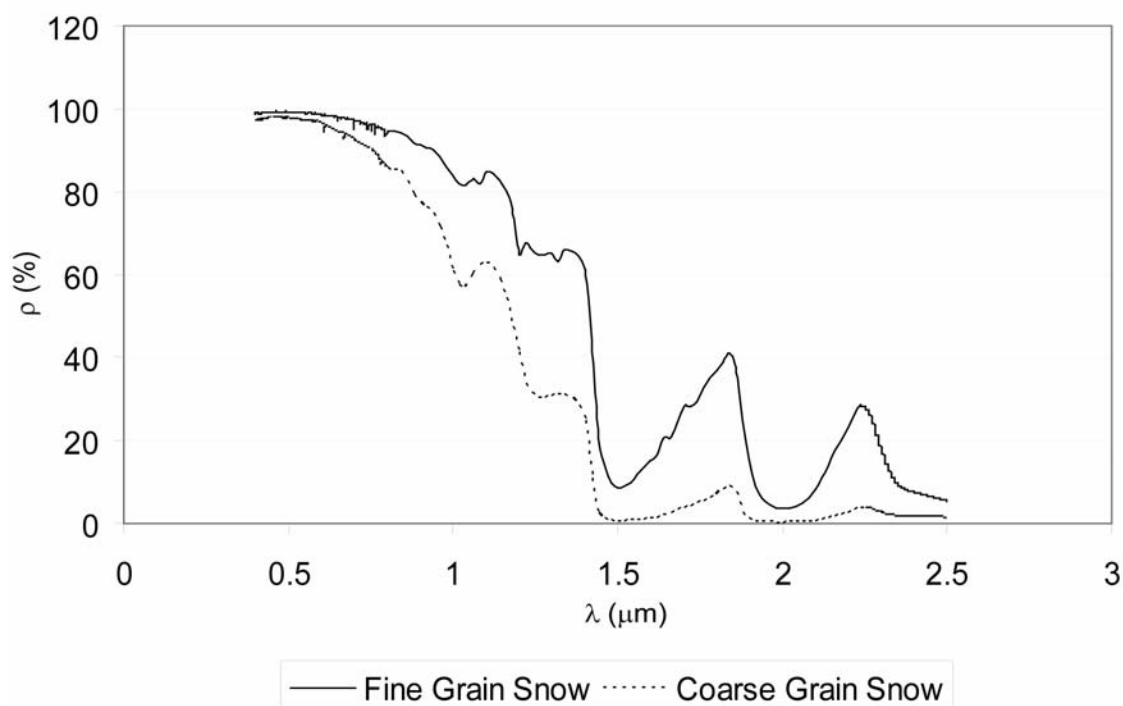


Figure 1: Percent reflectance (ρ) vs. wavelength (λ) for effective fine (24 μm) and coarse (178 μm) grain snow spanning the EM spectrum from 0.4 to 2.5 μm . The spectrum from 0.3 to 2.08 micrometers was modeled using the optical constants of ice in a Mie theory and radiative transfer model (Dozier and Warren, 1982). The spectrum from 2.08 to 14 μm was measured from (Salisbury et al., 1994).

NDSI is used in the SNOMAP algorithm on the MODIS sensor for identification of snow and ice and to discriminate between snow/ice and cumulus clouds (Riggs, et al., 1994). Pixels that are 50% or greater covered by snow have been found to have NDSI values greater than 0.4 (Dozier, 1989). Other factors can substantially reduce visible and NIR/SWIR snow reflectance and subsequently NDSI, such as soot, litter, and aging. Small amounts of impurities affect snow albedo only in the spectral region where absorption of light by ice is weakest, mainly in the visible (Warren, 1982). Therefore, thermal information (T_b used in the simulations) is used in the NSMI to control for changes in the state of the snow surface due to the melt process by tracking changes in thermal conditions of the snow surface.

Figure 2 is a conceptual diagram of NSMI as the snow pack evolves: A relatively dry snow pack occupies the lower right corner, corresponding to relatively high NDSI values and low surface temperatures. This region is dynamic and should in theory change as the snow pack evolves through the warming phase to a period when the pack becomes isothermal and begins to release melt water.

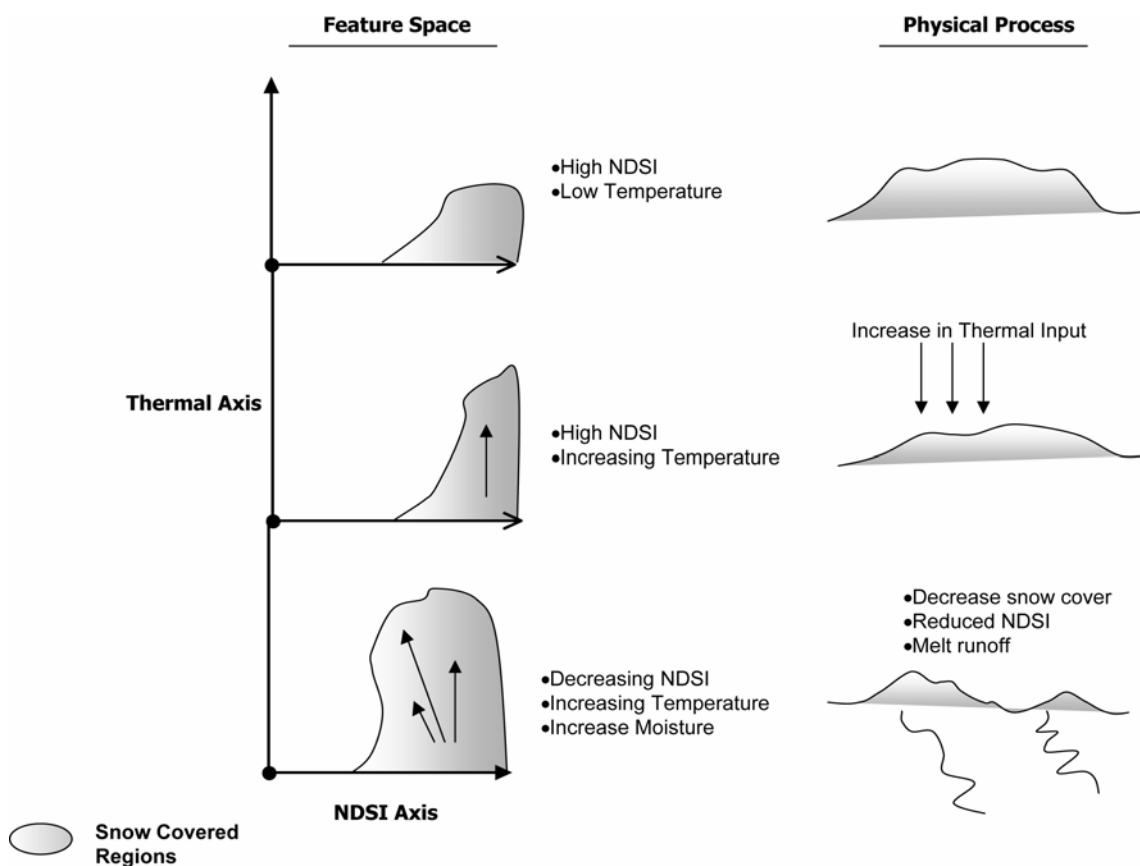


Figure 2: Diagram describing construction of NMSI feature space and theoretical variations in NMSI as a function of melt.

The feature space should capture these changes as an increase in surface temperature as well as convergence of NDSI values towards the upper right region of the feature space. The feature space can be clustered to map each pixels into regions at various stages in the melt process.

A simulated NSMI was constructed through computing modeled brightness temperature using a model derived by Dozier and Warren (1982), and NDSI using the simple Wiscombe and Warren (1981) (WWM) radiative transfer model. WWM was the

basis that Dozier and Warren (1982) used to compute brightness temperature. This is illustrated in Figure 3. Simulated monochromatic brightness temperature is given by:

$$T_b = hc / k\lambda \ln [1 + (e^{hc/(k\lambda T)} + \epsilon - 1) / \epsilon] \quad [2]$$

Where:

ϵ = directional-hemispherical emissivity

λ = wavelength

T = surface temperature

c, h, k = constant

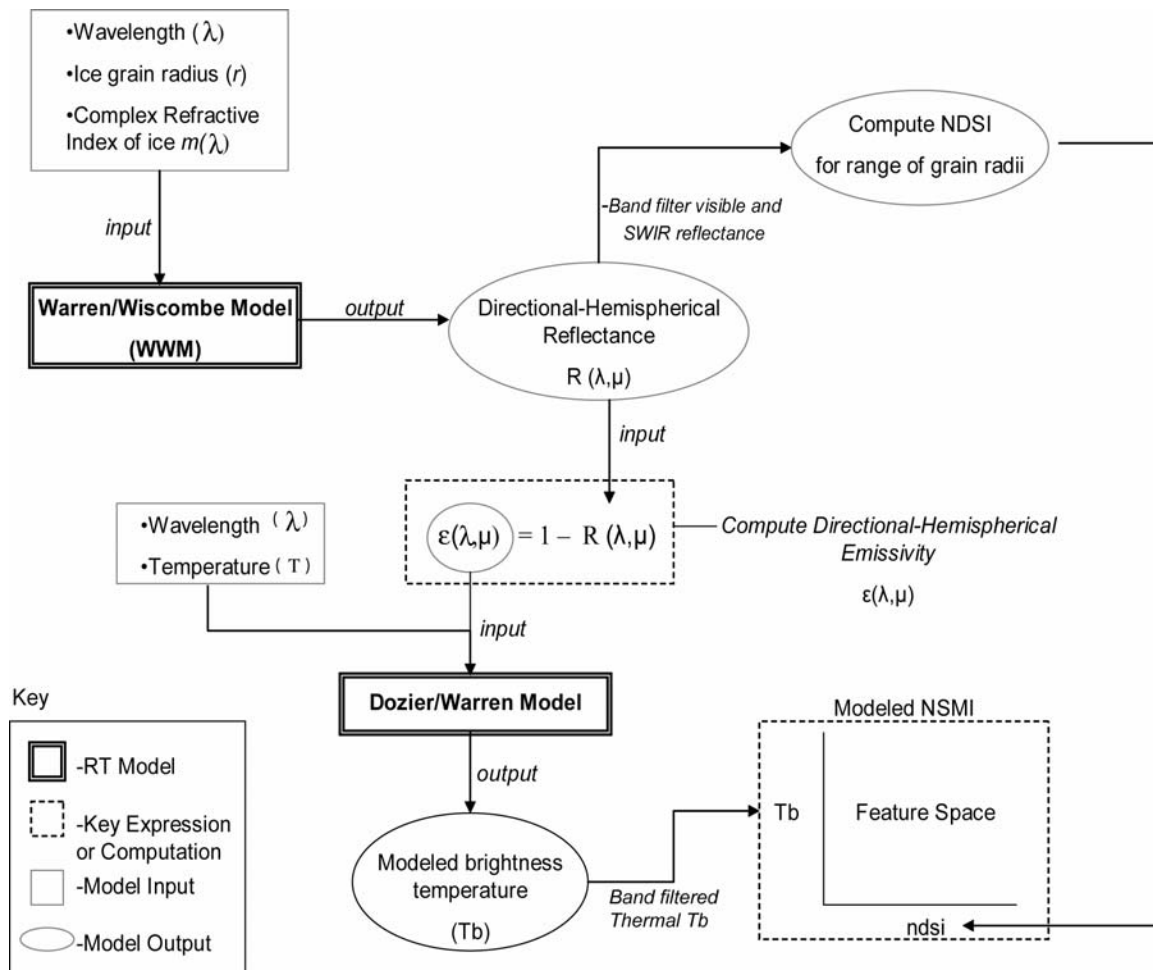


Figure 3: Schematic diagram of modeling components used in the development of simulated NSMI. Two radiative transfer models are used: WWM and Dozier and Warren (1982). WWM was used to compute simulated hemispherical-reflectance for a range of grain sizes and wavelengths. Modeled Hemispherical-reflectance was used as input into the computation of modeled NDSI and directional-hemispherical emissivity. Directional-hemispherical emissivity, wavelength and temperature (T) were used as input into the Dozier and Warren Model to compute modeled brightness temperature. MODIS band filtered reflectance was used to compute NDSI and brightness temperature (T_b) as a function of snow grain radius and wavelength. NDSI and T_b were used to construct modeled near surface moisture index feature space.

Directional-hemispherical emissivity is derived from modeled directional-hemispherical reflectance given by:

$$\epsilon(\lambda, \mu_v) = 1 - R(\lambda, \mu_v) \quad [3]$$

where $R(\lambda, \mu_v)$ is the directional-hemispherical reflectance computed using the WWM, which assumes each grain scatters within the far field of surrounding grains. This condition is not always true for closely packed grains in a natural snow pack, but the assumption holds for spheres that are in relative isolation, where 1) spheres are not arranged in a regular array; 2) inter-particle interference effects are negligible since the center-to-center separation d is large compared to the incident wavelength λ , for the solar spectrum (Dozier and Warren, 1982); 3) each grain is exposed to an incident plane wave; and 4) grains do not shadow one another (Wiscombe and Warren, 1981). WWM models scattering by spheres using Mie theory, which requires the size of the incident wavelength be comparable to the radius of the particle, for particles with radii approximately between 10^{-3} and $1\mu\text{m}$ for wavelengths in the solar reflective region of the EM spectrum (Kiddar and Haar, 1995). WWM takes as input ice grain radius (r), wavelength (λ), and the complex refractive index $m(\lambda)$ of ice. The model was iterated to produce modeled reflectance for ice particles represented as optically equivalent spheres with radii between 10 and $1000\mu\text{m}$. An optically equivalent sphere is used to approximate snow crystals in the snowpack, where the 'equivalent sphere' is that which has the same volume-to-surface ratio as the irregularly shaped grains in the snowpack (Nolin, 1998).

The WWM was used to compute directional-hemispherical reflectance, which is the integrated total flux leaving a surface in all directions divided by the total irradiance (Warren, 1982). Directional-hemispherical reflectance was computed for near surface non-shallow snowpack, as a function of wavelength and grain size. WWM determines directional-hemispherical reflectance, neglecting polarization, as well as the influence of

surface contaminants (i.e. soot) for a semi-infinite snow pack (i.e substrate reflectance causes less than 1% change in snow cover reflectance (Dozier et al., 1989)) and direct beam illumination, at a solar zenith angle θ_s , using the delta-Eddington approximation to the equation of radiative transfer (Wiscombe and Warren, 1981). For more details regarding the WWM please refer to Wiscombe and Warren (1981).

Simulated reflectance, as a function of grain radii ranging from 10 μm to 1000 μm at 10 μm increments, and wavelengths between 0.4 μm and 8.7 μm (in 0.1 μm increments) were used as input into the WWM to compute model reflectance for a fixed solar zenith angle (θ_0) of 60° , (where $\mu = \cos \theta_0$). Modeled reflectance was used to compute NDSI across band filtered MODIS visible, and SWIR bandpass at band 4 (0.54-0.565 μm), and 6 (1.628-1.652 μm) using a square wave filter. The Dozier/Warren Model was used to compute T_b across band filtered MODIS thermal band 29 (8.4-8.7 μm) at a fixed view angle (θ_v) (angle of viewing from nadir $\theta_v = 0$) of 60° (see Figure 3). Figure 4 demonstrates modeled NSMI feature space constructed from modeled NDSI and T_b as a function of grain radii. Figure 4 was constructed by computing T_b for various grain sizes at fixed surface temperatures (T) of 245, 250, 255, 260, 265, and 273 K.

NDSI sensitivity to changes in optical grain size was examined to determine how useful the index can be as a proxy for snow grain size. Figure 5 is modeled NDSI vs. optical snow grain size. NDSI appears to be sensitive to changes in snow grain radii until approximately 500 μm . After 500 μm , NDSI saturates and loses significant sensitivity to changes in larger grain radii.

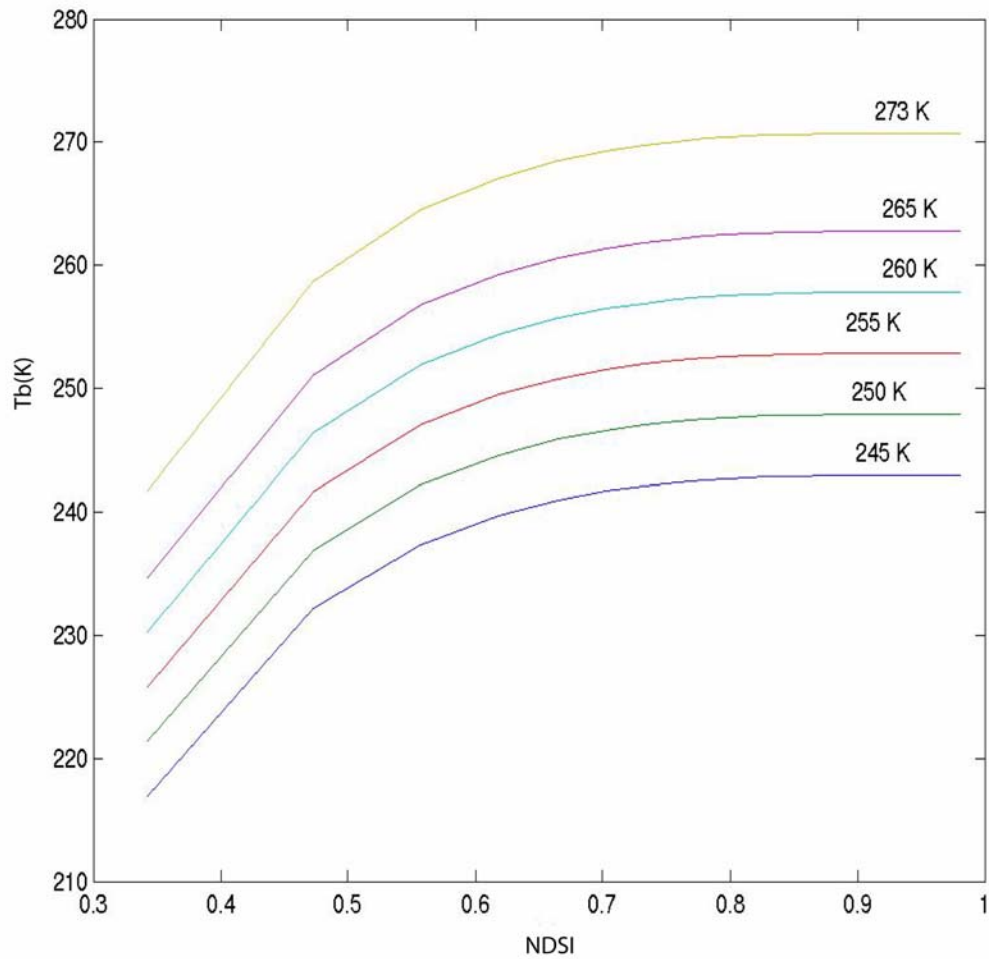


Figure 4: Simulated NMSI feature space constructed from modeled NDSI and T_b . NDSI as a function of grain size was computed and T_b derived at fixed kinetic temperatures ranging from 245 to 273K.

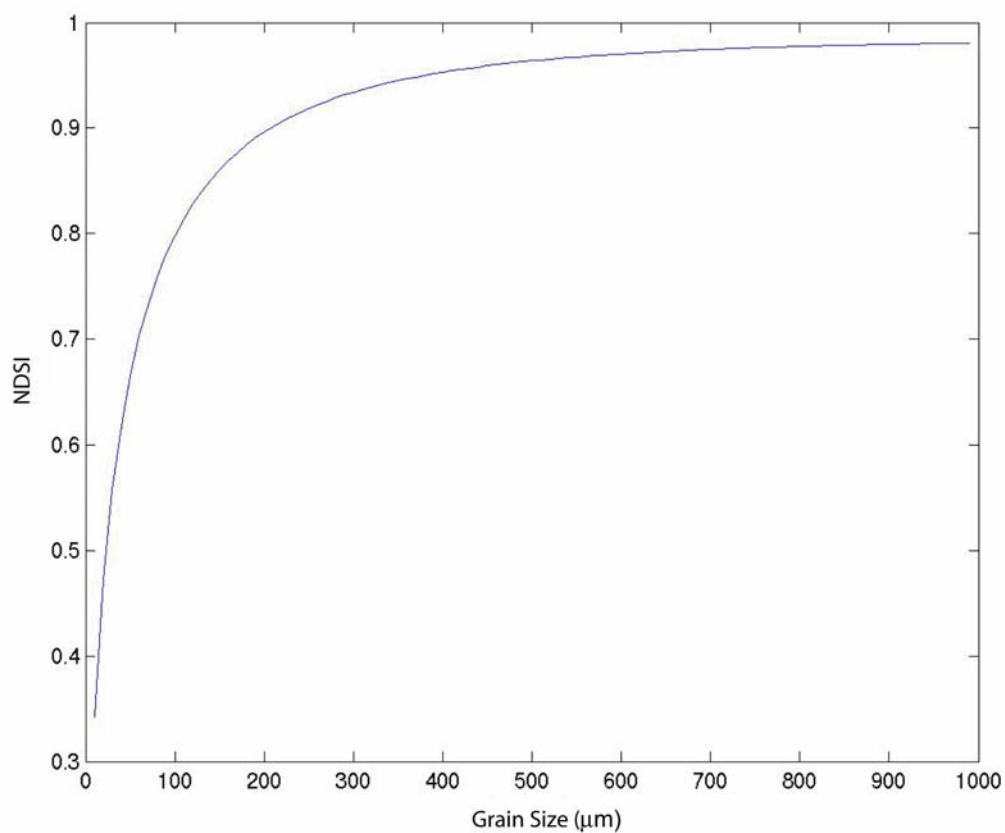


Figure 5: Modeled NDSI as a function of optical snow grain radius for grain radii ranging from 10 to 1000 μm . NDSI was computed using band averaged modeled reflectance using the WWM across MODIS bands 4 (0.52-0.60 μm) and 6 (1.6-1.7 μm). NDSI appears to saturate at an optical grain radius of $\sim 500\mu\text{m}$.

4. METHODS

Validation of the simulated NMSI involved examination of ground-based snow measurements during the ablation season as well as extracted surface reflectance and temperature measurements from ASTER. The use of ASTER as a validation source was based on its higher spatial resolution and comparable bandpass as MODIS, used in the radiative transfer modeling of simulated NSMI. Table I details a comparison of MODIS and ASTER bands used in this analysis.

Table I. Comparison of MODIS and ASTER Bands used in NSMI Simulation and Validation

Sensor	Visible (μm)	SWIR (μm)	Thermal (μm)
MODIS	Band 4 (0.54-0.565)	Band 6 (1.628-1.652)	Band 29 (8.4-8.7)
ASTER	Band 1 (0.52-0.60)	Band 4 (1.6-1.7)	Bands 10-12 (8.125-11.65)

Ground-based measurements of mean pack temperature, surface temperature, surface grain shape, and wetness, as well as surface and near surface grain size distribution were used as validation. These data were collected during the CLPX campaign in the Fraser Experimental Forest near Fraser Colorado on February 19, and March 25, 2002. Data were collected over three Intensive Study Areas (ISA) designated as Alpine, Fool Creek, and St. Louis. Table II outlines general ISA characteristics. Figure 6 displays the locations of CLPX ISAs. Each ISA spans a range in elevation as and land cover types.

Table II. General Characteristics of Fraser-CLPX Intensive Study Areas

Sample Site	Mean Elevation (m)	Land Cover Composition (%)
Alpine	3557	24-Evegreen Forest 50-Herbaceous Tundra 22-Shrub/Bush Tundra 3-Exposed/Bare Rock
Fool's Creek	3132	100-Evergreen Forest
St. Louis Creek	2726	100-Evergreen Forest

An ASTER scene acquired on April 4, 2002 was used in this analysis.

Atmospherically corrected surface reflectance and surface temperature products were downloaded for this date from the EOS Data Gateway ASTER On-Demand product archive. Each ISA was sampled with 145 reflectance and brightness temperature extractions. NSDI was computed using ASTER acquired reflectance at Band 1 (0.52-0.60 μ m) and Band 4 (1.6-1.7 μ m). Band 1 (15m²) was resampled to a spatial resolution of 30m² (band 4 resolution).

This scene was selected because it was acquired close to the date

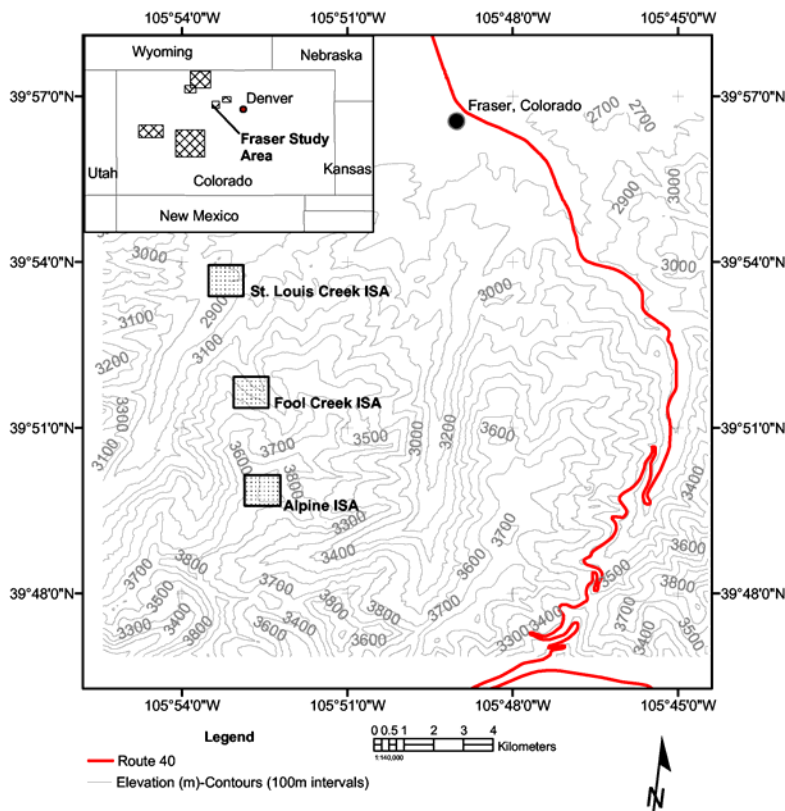


Figure 6: Topographic map of the Fraser, Colorado test region used during the CLPX field campaign with three ISA's highlighted in boxes designated as St. Louis Creek, Fool Creek, and Alpine,

of CLPX ground measurements. Since ASTER does not acquire scenes daily, temporal changes in melt season snow pack could not be assessed. Instead, this single scene was used to represent the snow pack at different stages of the melt process; the scene covers a wide range in elevation, which facilitates sampling of reflectance and temperature from lower elevation regions and higher elevation regions within the ISA boundaries. We assume lower elevation samples represent a more evolved pack than higher elevations regions. The use of regions at different elevations for a time series of images to represent the snow pack at different stages is possible because seasonal accumulation of snow

increases with elevation due to increase in precipitation with altitude and larger proportion of snowfalls than rainfalls at higher elevation as a function of the temperature lapse rate (Martinec, 1987). Solar and longwave radiation usually dominate the snow melt process (Elder et. al, 1991) but temperature also plays an important role. Due to the temperature lapse rate, lower elevation regions will generally be warmer and higher elevation regions cooler. Since snow ablation is partially controlled by energy exchanges at the air/snow interface (Elder et. al, 1991), warmer temperatures at lower elevation could accelerate surface melting relative to regions at higher elevations due to downward energy transfer from the warm air to the cool snow surface. Other important topographic variables such as slope and aspect can mitigate snow ablation as well (Elder et. al, 1991). 145 reflectance and brightness temperature pixels from the March ASTER scene were sampled within the approximate boundaries of each ISA.

Table III. Descriptive Statistics of Visible and SWIR Reflectance and Tb Pixels Sampled from ASTER Validation Scene (Total Sample per ISA=145)

ISA	Mean			Std			Max			Min		
	V	S	T	V	S	T	V	S	T	V	S	T
Alpine	0.37	0.11	274.1	0.09	0.05	3.13	0.43	0.25	284.4	0	0	269.8
Fool	0.19	0.05	275.6	0.1	0.02	0.77	0.43	0.23	277.3	0	0	273.8
St. Louis	0.14	0.06	277.2	0.06	0.01	0.85	0.44	0.10	280.2	0	0	275.6

V=visible reflectance, S=SWIR reflectance, T=brightness temperature

5. RESULTS AND DISCUSSION

5.1 Ground Data

CLPX ground data provided information on the thermodynamic state of snow pack surface and near surface. Changes in surface and near surface properties from February to March demonstrate an evolving pack. February sites were dominated generally by faceted and mixed grains with dry surface conditions (Figure 7). Surface grains were characterized as ‘new’ due to documented new snow fall during surveys. Near surface grain sizes were dominated by new and faceted grains across all three sites, with an increase in the occurrence of rounded and mixed grains than the surface. March sites (Figure 8) were characterized by an increase in faceted grains, with more mixed and rounded grains at Alpine and Fool creek compared to February. Surface conditions, though primarily dry, showed an increase in moist and wet conditions, particularly at the St. Louis site. Surface grain distribution in March was more varied, with larger numbers

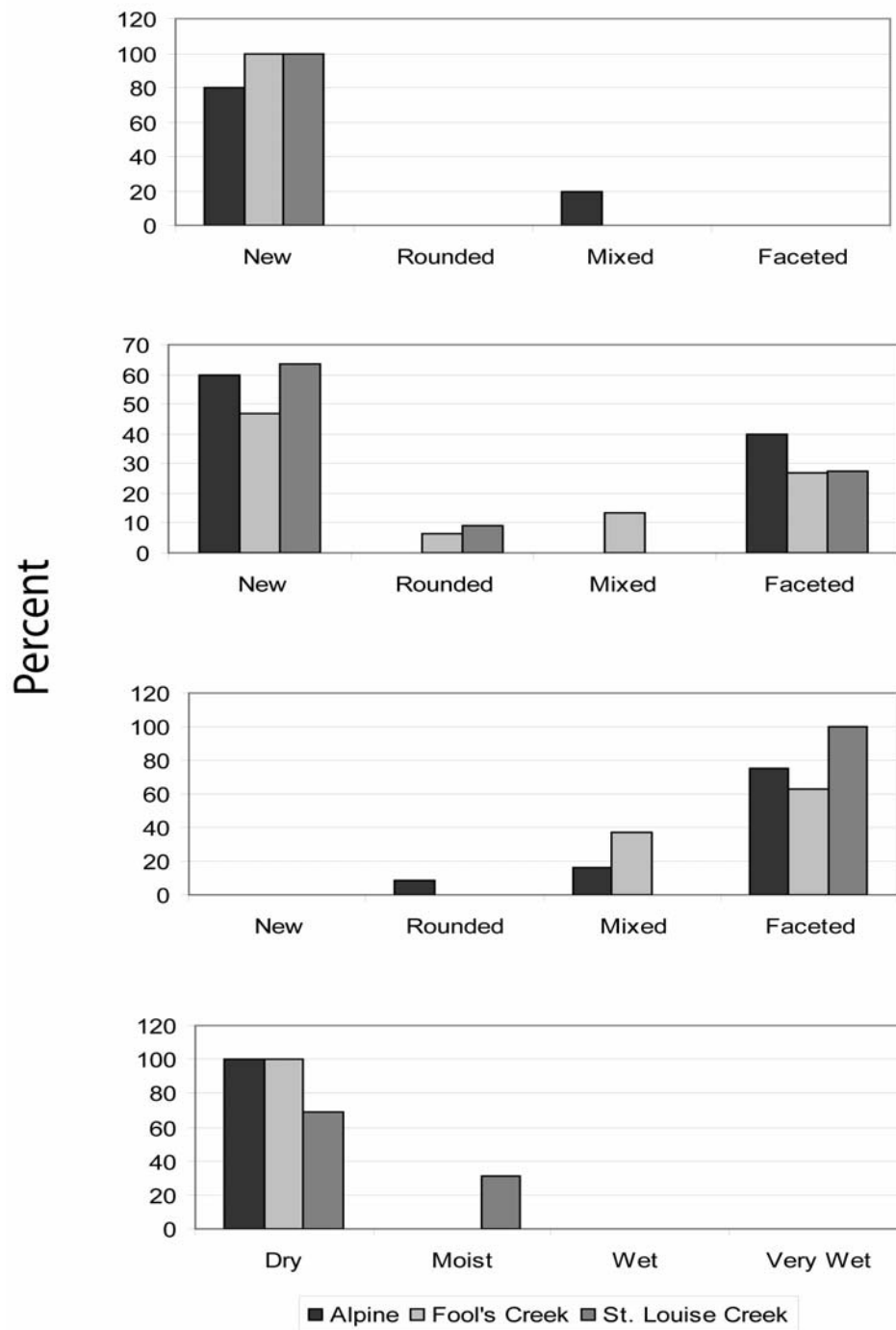


Figure 7: CLPX ground-based surface and near surface characteristics from February 19, 2002 over all three ISA's. A.) surface grain distribution, B.) near surface grain distribution, C.) majority grain shape, D.) surface wetness.

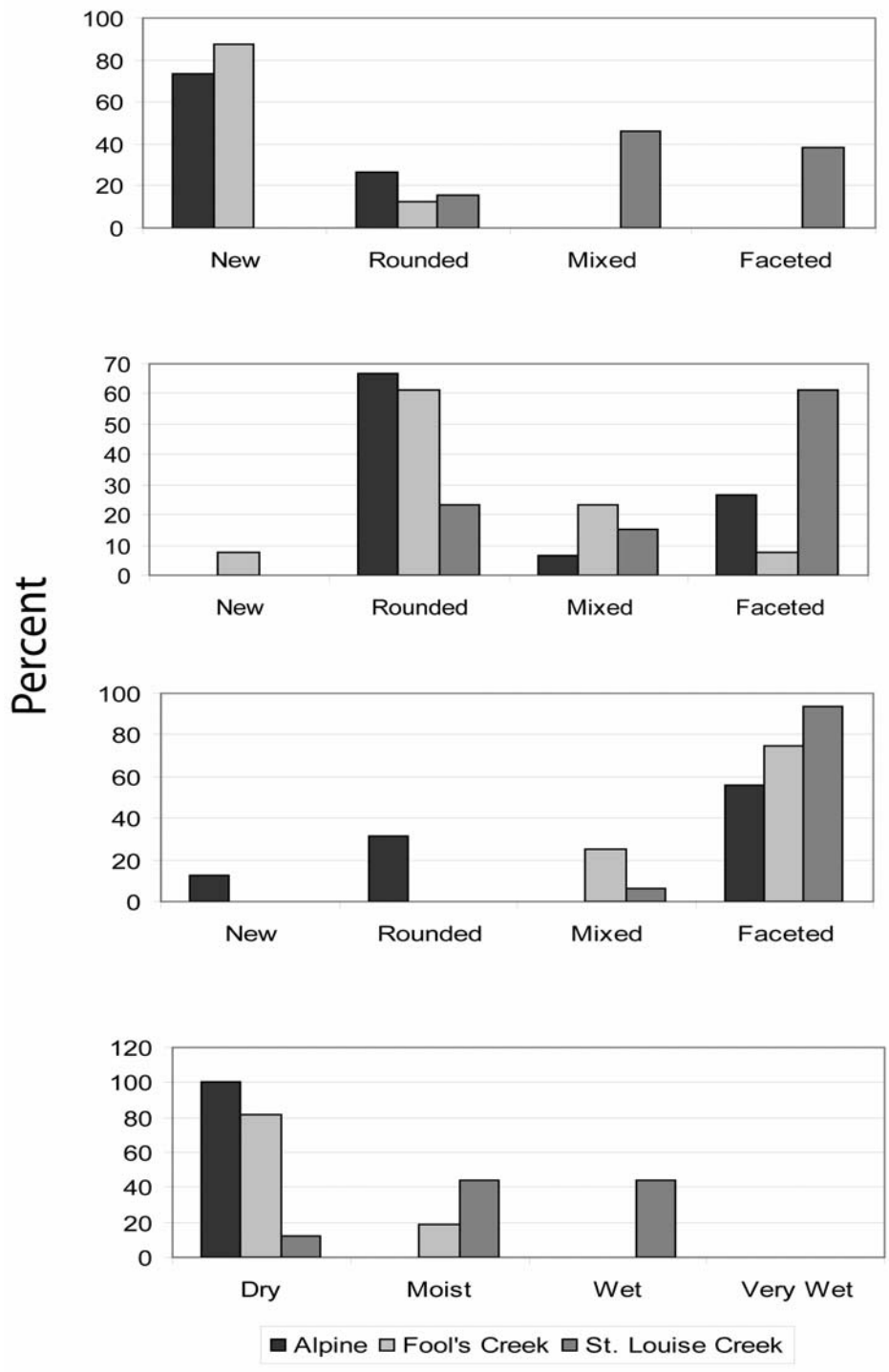


Figure 8: CLPX ground-based surface and near surface characteristics from March 25, 2002 over all three ISA's. A.) surface grain distribution, B.) near surface grain distribution, C.) majority grain shape, D.) surface wetness.

of sites having rounded, mixed, and faceted grains, particularly at the St. Louis site. Near surface grains in March were largely rounded and faceted, with an increase in rounded grains across all three sites. CLPX surface and mean pack temperatures were acquired over each ISA. Within each ISA surface and mean pack temperatures were averaged. February surface and average pack temperatures were lower at Alpine ISA than the other ISAs (Figure 9a). Surface temperatures were slightly cooler across all three sites for February. Surface and average pack temperatures in March (Figure 9b) were warmer for all three sites, with the St. Louis ISA having the warmest temperatures, near 0° C.

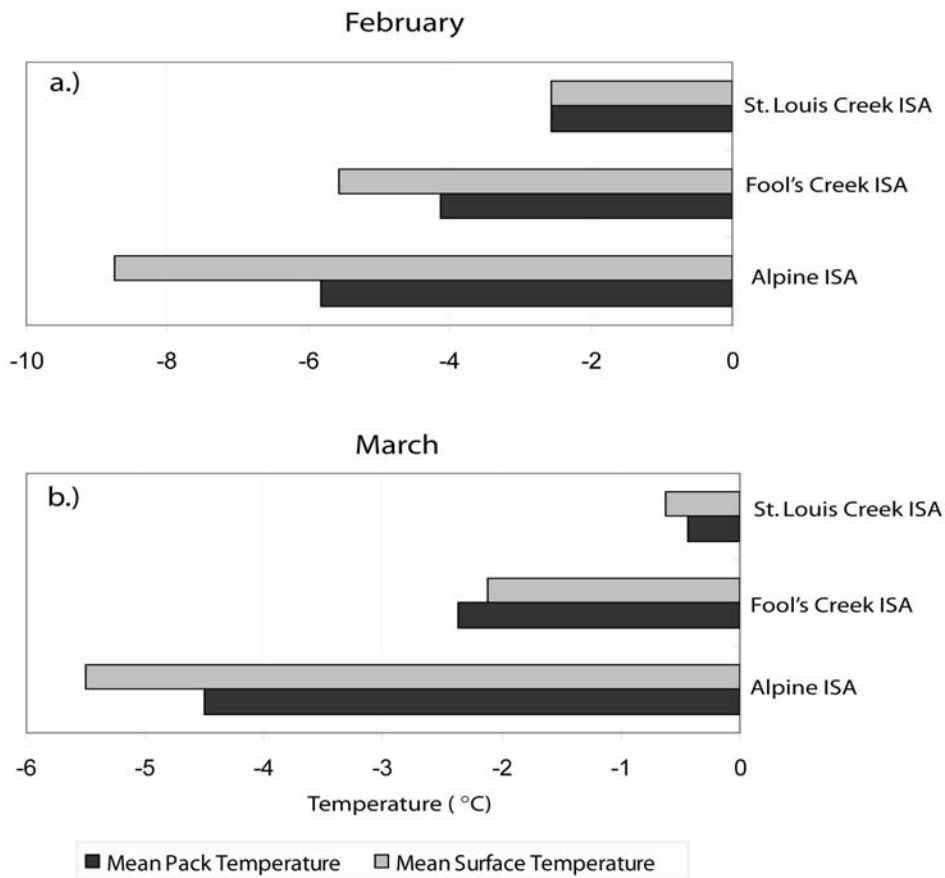


Figure 9: CLPX ground-based surface and near surface temperature over all three ISA's. Samples of average pack temperature and surface temperature derived from several snow pits within each ISA were averaged. A.) February 19, 2002 mean pack and surface temperatures, B.) March 25, 2002 mean pack and surface temperatures.

5.2 ASTER Data

Samples extracted from co-registered surface reflectance and surface brightness temperature products were used to construct the NSMI feature space. Samples from each ISA were averaged and a mean surface brightness temperature and mean NDSI were computed. Figure 10 displays ASTER derived NSMI. Alpine ISA plotted in the lower right corner of the NSMI feature space with the lowest temperatures and highest NDSI. As the temperature increased the mean NDSI decreased mapping Fool Creek and St. Louis ISAs towards the upper right region of the NSMI feature space. Assuming the higher elevation Alpine ISA represents a cooler, less evolved pack, while the St. Louis ISA represents a warmer, more evolved pack, then the trend observed in the NSMI feature space is consistent with simulated NSMI (Figure 4) and the conceptual NSMI (Figure 3).

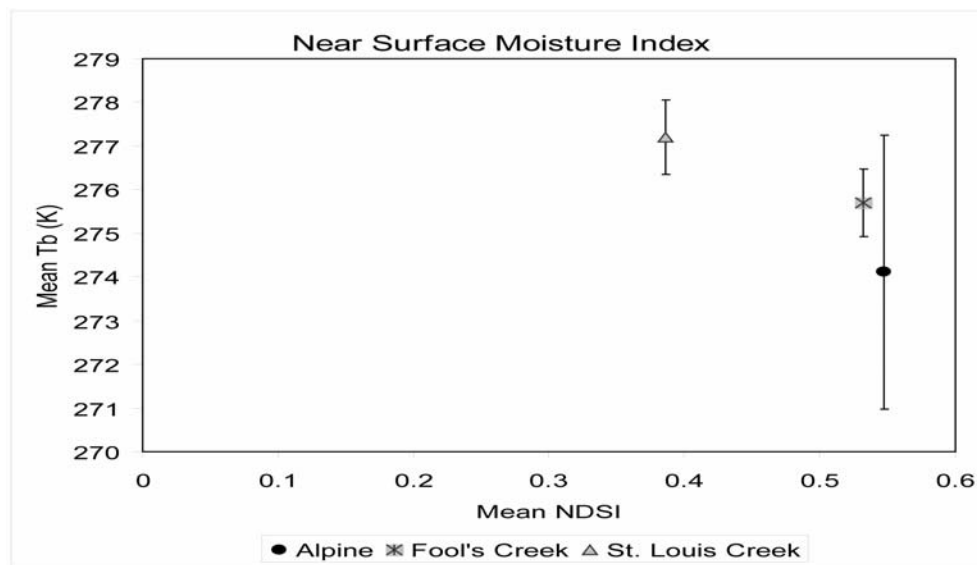


Figure 10: NSMI derived from sampled pixels from the April 4, 2002 ASTER scene. Surface brightness temperature and reflectance (used to compute NDSI) were derived from 145 samples in each ISA. Sampled values were averaged and plotted to produce a mean NSMI feature-space. Error bars characterize standard deviations for each ISA samples (Alpine std = 3.13, Fool Creek std = 0.777, St. Louis Creek std. = 0.857).

If the different regions represented time elapsed images over the Fraser study region, we might expect the Alpine site to be a scene acquired earlier in the melt season, while the St. Louis region a scene acquired later in the season. The behaviour of mean NDSI and brightness temperatures for each ISA is consistent with theory. Snow pack changes rapidly in spring reaching an isothermal state at 0°C and satisfying the snowpack liquid water holding capacity (the total amount of water the pack can hold before release of water) (Rango, 1993). When these two conditions have been met, the snow pack is ripe and absorption of additional energy will produce snowmelt (Rango, 1993). As melt progresses the impact of entrained liquid water within the snow pack matrix tends to increase grain size when the pack becomes saturated. Initially, fragile and thermodynamically unstable dendritic branches of accumulating snow grains erode through collisions and water vapor transport (Painter et al., 1998). Snow grain metamorphism is faster at higher temperatures, in the presence of liquid water (Colbeck, 1979; Painter et al., 1998). Pack ripening process is governed by large temperature gradients between grains, particularly, between grains of unequal size under conditions of high liquid content (Colbeck, 1973). Snow grains increase with liquid water content due to heat flow to the margins of grain that share boundaries (Colbeck, 1979). Smaller grains are equalized at lower temperatures when surrounded by liquid water, causing heat flow from larger particles, and rapid melt of small grains, subsequently causing small grain entrainment and grain cluster formation (Colbeck, 1973). Grain clusters form quickly, decreasing reflectance (Davis et al., 1993). An increase in grain size causes an increase in the path length that must be traveled through ice by an incident photon between scattering opportunities (Warren, 1982). As the snow becomes wetter, the

relative difference in visible and NIR/SWIR reflectance would increase. This difference is due to the increase in absorptive properties of ice from the visible to the NIR/SWIR. The absorption coefficient (imaginary part of the refractive index) increases by 7 orders of magnitude in the wavelengths from 0.4 – 2.5 μm (Dozier, 1989). Given this, an increase in grain size due to the melt process has little effect on visible reflectance, but substantially reduces NIR/SWIR reflectance (Painter et al., 1998). Model results indicate that this process would tend to increase the NDSI within a limited range as a function of grain size (NDSI saturates at approximately grain radii near 450 μm) (Figure 5). Conceptually (Figure 2) we might expect a reduction in the distribution of NDSI values as the snow pack ripens with some increase and decrease in NDSI. Figure 10 demonstrates a decrease in NDSI for the lower elevation ISA. This behavior is consistent with Kay et al. (2003), who have observed similar results when they examined the relationships between a snow grain proxy and surface temperature over Mt. Rainier, Washington using the multi-spectral MODIS/ASTER Airborne Simulator. Their results indicate a reduction in the range of values for the grain proxy over regions of the mountain that were warmer and ideally contained larger snow grains.

Standard errors for each ISA in Figure 10 indicate greater variability in brightness temperature at the Alpine site than the other two ISAs. The Alpine ISA includes great variability in vegetation cover, with higher elevation regions within Alpine being above tree-line, and dominated by only snow and rock, while lower elevations regions containing patches of dense vegetation. A solid canopy such as a coniferous forest can act as a black body in the long-wave region of the EM spectrum, with emissivities as high as 0.97 (Singh and Singh, 2000). Since snow cover has comparable emissivity, long-

wave flux between the two objects can be governed partially by temperature differences. Generally, vegetation is warmer than the snow surface, causing significant transfer of long-wave energy from the canopy to the snow surface through sensible heat flux (Singh and Singh, 2000). Greater variability in temperature and optical differences throughout the Alpine ISA as a function of vegetation distribution could account for high standard errors. Relative to vegetation in the visible region, snow has very high reflectance. In the NIR/SWIR region, the relative difference in reflectance still demonstrates higher reflectance for snow over vegetation, but with decreasing magnitude wavelength increases. Over the wavelength ranges used to compute modeled and ASTER measured NDSI, the spectral contribution of vegetation would tend to decrease visible reflectance and slightly increase NIR/SWIR reflectance. Since the difference in snow and vegetation reflectance is greater in the visible region, these wavelengths would tend to have greater influence on the decrease in NDSI over pixels containing both vegetation and snow. Additionally, the contribution of vegetation would tend to dominate the overall surface-leaving reflectance the denser the vegetation canopy within a given pixel. Generally, vegetation has higher emissivity than snow and so behaves more like a black-body. The radiant brightness temperature over vegetation would tend to be higher than snow. Variability in the relative amounts of vegetation across sampled pixels would increase the distribution of brightness temperature values and contribute to high standard errors in the Alpine ISA extracts.

6. CONCLUSION AND RECOMMENDATION

Our analysis demonstrates that sensors operating in the visible, NIR, SWIR, and thermal regions of the EM may have the potential for improved monitoring of surface snowmelt conditions as well as use in inferring snow pack state during the ablation season. A simulated NSMI using a radiative transfer model was created. A measured NSMI was constructed from extractions of ASTER measured surface reflectance and brightness temperature. Initial testing of a Near Surface Moisture Index was performed to evaluate its utility for tracking the evolution of alpine snow packs throughout the melt season. Model simulations demonstrate that the NSMI feature space should be sensitive to changes in the state of the snow pack. Ground-based measurements from the CLPX program in late February and March of 2002 indicate significant changes in snow surface properties, representing a warming pack across three ISA's. Similar behaviors are reflected in changes in average pack temperatures. The ASTER derived NSMI demonstrates behavior consistent with theory, with some deviations. Differences between theory and measurement could be due to the wide range of conditions present within any given ISA, including variations in vegetation, topography, as well as in snow BRDF. Additional considerations involve compensation for the influence of mixed pixels, which would require the determination of fraction snow covered area before constructing the NSMI. In general, grains grow more rapidly with warmer temperatures, but other processes common in the mountains can promote rapid grain growth at sub-melting temperatures as well. The unambiguous identification of ablation periods is critical to the success of the NSMI approach (personal communication, Bert Davis). Other considerations involve correcting MODIS reflectance bands for sun angle, terrain

geometry and viewing geometry for each pixel (personal communication, Bert Davis). More work is required for development of a robust algorithm, which if proven effective could be applied to the MODIS and the future NPOESS-VIIRS system as an operational tool for water management as well as a viable research aid to assess impacts of climate variability on snow cover dynamics.

Acknowledgments. This study was supported by NASA under the Earth System Science Fellowship (ESS) Grant NGT5. I would like to thank Dr. Kelly Elder for his thoughtful review as well as the National Forest Service for support. I would like to thank Dr. Anne Nolin, at Oregon State University, as well as Dr. Robert Davis (CRREL) for their valued feedback and suggestions. Additionally, I'd like to thank the anonymous reviewers for their time and constructive suggestions, which resulted in a superior manuscript. I would also like to thank Dr. Jeff Dozier (UCSB) and Dr. Don Cline (NOHRSC) for their thoughtful suggestions and support.

REFERENCES

Dozier, J., and D. Marks. 1987. Snow mapping and classification from Landsat Thematic Mapper data. *Ann. Glaciol.*, Volume 9, 1-7.

Dozier, J. 1989. Spectral signature of alpine snow cover from the Landsat Thematic Mapper. *Remote Sens. Environ.*, 28, 9-22.

Dozier, J., and S.G. Warren. 1982. Effect of view angle on the infrared brightness temperature of snow. *Water Resources Research*, Volume 18, No. 5, 1424-1434.

Dozier, J., S. R. Schneider, and D.F. McGinnis. 1981. Effect of grain size and snowpack Water equivalence on visible and near-infrared satellite observations of snow. *Water Resour. Res.*, vol(17), no.4. 1213-1221.

El-Ashry, M. and D. Gibbons. 1988. *Water and arid lands of western United States*, Cambridge Univ.Press, New York.

Green, R.O., and J. Dozier. 1996. Retrieval of surface snow grain size and melt water from AVIRIS spectra. In *1996 Airborne Geoscience Workshop*. Pasadena, CA. Jet Propulsion Laboratory, 127-134.

Kay, J.E., A.R. Gillespie, G.B. Hansen, and E.C. Petitt. 2003. Spatial relationships between snow contaminant, grain size, and surface temperature from multispectral

images of Mt. Rainier, Washington (USA). *Remote Sensing of Environment*, Vol (86), 216-231.

Liou, K.N. 2002. *An Introduction to atmospheric radiation 2nd edition*. Academic Press, International Geophysics Series, Volume 84.

Nemani, R. L. Pierce, S. Running, and S. Goward.1993. *Developing* satellite-derived estimates of surface moisture status. *Journal of Applied Meteorology*. Vol(32), 548-557.

Nolin, A.W., and J.C. Stroeve. 1997. The changing albedo of the Greenland ice sheet: implications for climate modeling. *Ann. Glaciol.*, Volume 25, 51-57.

Nolin, A.W. 1998. Mapping the martian polar ice caps: applications of terrestrial optical remote sensing methods. *Journal of Geophysical Research*, Volume 103, No. E11, 25,851-25,864.

Nolin, A.W., and J. Dozier. 2000.A hyperspectral method for remotely sensing the grain size of snow. *Remote Sensing of Environment*, 74(2), 207-216.

Painter, T.H., J. Dozier, D.A. Roberts, R.E. Davis, R.O. Green. 2003. Retrieval of subpixel snow-covered area and grain size from imaging spectrometer data. *Remote Sensing of Environment*, 85 (2003), 64-77.

Rango, A., A.E. Walker, and B.E. Goodison.2000. Snow and Ice. In *Remote Sensing in Hydrology and Water Management*, G.A. Schultz, and E.T. Engman (eds.), 239-262.

Rango, A., J. Martinec, J. Foster, and D. Marks.1983. Resolution in operational remote sensing of snow cover. In *Hydrological Applications of Remote Sensing and Remote Data Transmission* , Goodison BE (eds). IAHS Publication No. 145. IAHS Press: Wallingford; 371-382.

Rango, A.1993. II. Snow hydrology and remote sensing. *Hydrological Processes*, Volume 7, 121-138.

Riggs, G. D. Hall, and V. Salomonson. 1994. A snow index for Landsat thematic mapper and ModerateResolution Imaging Spectroradiometer. In *Proceedings, International Geoscience andRemote Sensing, Symposium*, Pasadena, CA, August, Piscataway, NJ: IEEE, 1942-44.

Salisbury, J. W., D'Aria, D. M., and Wald, A. E., 1994, Measurements of thermal infrared spectral reflectance of frost, snow, and ice. *Jour. of Geophysical Research*, v. 99, p. 24,235-24,240.

Schultz, G.A., E.T. Engman. 2000. *Remote Sensing in Hydrology and Water Management*. Springer.

Singh, P, and V.P. Singh. 2001. *Snow and Glacier Hydrology*. Kluwer Academic Publishers.

Steppuhn, H.1981. Snow and agriculture. In Gray, D.M. and Male, D.H. (Eds.).1982. *Handbook of Snow: Principles, Process, Management and Use*. Pergamon Press, Toronto.

Warren, S.G.1982. Optical properties of snow. *Rev Geophys. Space Phys.* 20:67-89.

Wiscombe, W.J., and Warren, S.G.1981. A model for the spectral albedo of snow I: Pure snow. *J. Atmos. Sci.*, 37:2712-2733.

Appendix D

Tracking Phases of Coupling between Snow Surface Optical and Thermal Properties with Melt Discharge during the Ablation Season

**TRACKING PHASES OF COUPLING BETWEEN SNOW SURFACE OPTICAL
AND
THERMAL PROPERTIES WITH MELT DISCHARGE DURING THE
ABLATION SEASON**

D.J. Lampkin¹, A.N. Nolin²

¹Department of Geography, Pennsylvania State University, University Park, PA, USA

²Department of Geoscience, Oregon State University, Corvallis, OR, USA

(unpublished)

ABSTRACT

A Near Surface Moisture Index (NSMI) for monitoring snow pack propensity for melt discharge must be able to perform during the entire ablation season. NSMI performance is contingent on the strength of coupling between surface optical/thermal and pack discharge during the melt season. We examine how well the NSMI performs by tracking phases of coupling between snow surface properties and propensity for melt using two ground-based approaches; one with higher snow surface spectral information and low temporal resolution, the other with high temporal resolution and coarse spectral information. A high spectral resolution field spectrometer was used to collect snow surface spectral signatures in addition to excavated snow pits at two sites (Berthoud Pass SNOTel Site and Robber's Roost Trailhead) near the Forest Service Fraser Experimental Research station in Fraser, Colorado during the period between March 22, 2004 and March 26, 2004. Archived data from the Mammoth Mountain Cooperative Snow Study Site (MMCS) in the eastern Sierra Nevada of California, spanning from April 1, 2002 through July 1, 2002, were used for its high temporal resolution throughout the 2002 ablation season. Data collected from the Fraser site and MMCS data set are separated by space and time, were considered a single observation in the attempt to monitor the snowmelt process. Ground-based snow surface spectra were acquired at two sites near Fraser, Colorado and compared to temperature and stratigraphic data collected from pits. Time series analysis using MMCS data indicated periods of temporal coupling between surface albedo, discharge, and surface temperature and discharge. Increases in melt discharge were associated with decreases in albedo and increases in surface temperature. A time-dependent NSMI was derived from the MMCS ground data, using albedo directly

as a proxy for a snow grain size index and surface temperature. Time varying NSMI indicated points that tracked towards low albedo and increasing surface temperature. Several days that did not follow this trajectory and were correlated with increases in snow depth, and decreases in surface temperature signalling of new snow fall events. Phases of decoupling exhibited within the MMCS-simulated NSMI were regulated by the temporal resolution (aggregation interval) specified to construct the feature space. Adjustments to the aggregation interval allow the NSMI feature space to be calibrated to various components of surface radiative variability. Coarser optical and thermal temporal resolutions will tend to shift NSMI feature space correlation to melt discharge from specific snowfall events to inter-seasonal trends. Results from this work indicate that surface optical and thermal properties can be used within the NSMI framework to track occurrences of melt discharge throughout the entire melt season.

1. INTRODUCTION

The total amount of water stored in a basin provides an estimate of the amount of water available for runoff and potential human use. Knowledge of the amount of water stored however provides no indication of when runoff will be produced or constitute a potential hazard (Elder and Dozier, 1990). Sensors in the visible and near- infrared portion of the spectrum have become important data sources for snow studies from regional to global scales (Rott, 1987). Remote sensing provides a rough estimate of melt by monitoring the snow pack in the early spring (Rango, 1993). Diagnostic information about the evolving spring time snow pack can be determined using snow surface optical and thermal properties.

The potential of optical remote sensing to track evolution of alpine snow packs and monitor the timing of melt depends on the strength of the relationship between near surface optical and thermal characteristics and potential for melt discharge throughout the ablation season. This analysis characterizes the magnitude and duration of temporal coupling between near surface spectral properties and internal snowpack parameters responsible for melt water production and release.

2. SNOWMELT PROCESS AND SURFACE ALBEDO

Snow metamorphosis, melting, and runoff are controlled by the variable magnitude of energy available to drive these processes, determined by the combination of local meteorological inputs of precipitation and energy (Marks et al., 1992). More specifically, the melt process involves a change of phase from ice to liquid water, driven by temperature and water vapour density gradients within the snow pack caused by heat exchange at the snow surface and at the snow-soil interface (Shook and Gray, 1997; Marks et al., 1992). Shortwave radiation reflected from the snow surface depends on several factors including the amount of incident solar radiation and the surface albedo (α) where:

$$K\uparrow = K\downarrow(\alpha) \quad [1]$$

The amount of energy not reflected is absorbed; therefore variations in the snow surface albedo can significantly influence the amount of energy available for melt once the pack has reached isothermal conditions.

3. DATA AND METHODS

Tracking the magnitude and duration of surface optical coupling with internal pack energy state and melt production with satellite data ideally requires timely surface spectral and internal pack information throughout the melt season. Such coupling must be characterized first using ground-based methods. In the absence of optimal high ground-based spectral and temporal resolution sampling, two field methods were used: one method employed higher snow surface spectral information and low temporal resolution; the other method used high temporal resolution and coarse spectral information (Figure 1). We used a high resolution field spectrometer to collect snow surface spectral signatures and excavated snow pits (March 22-26, 2004) at two sites (Berthoud Pass SNOTel Site and Robber's Roost Trailhead) near the Forest Service Fraser Experimental Research station in Fraser, Colorado. Archived data spanning April 1, 2002 through July 1, 2002 from the Mammoth Mountain Cooperative Snow Study Site (MMCS) in the eastern Sierra Nevada of California were selected for their high temporal resolution throughout the 2002 ablation season (Table I).

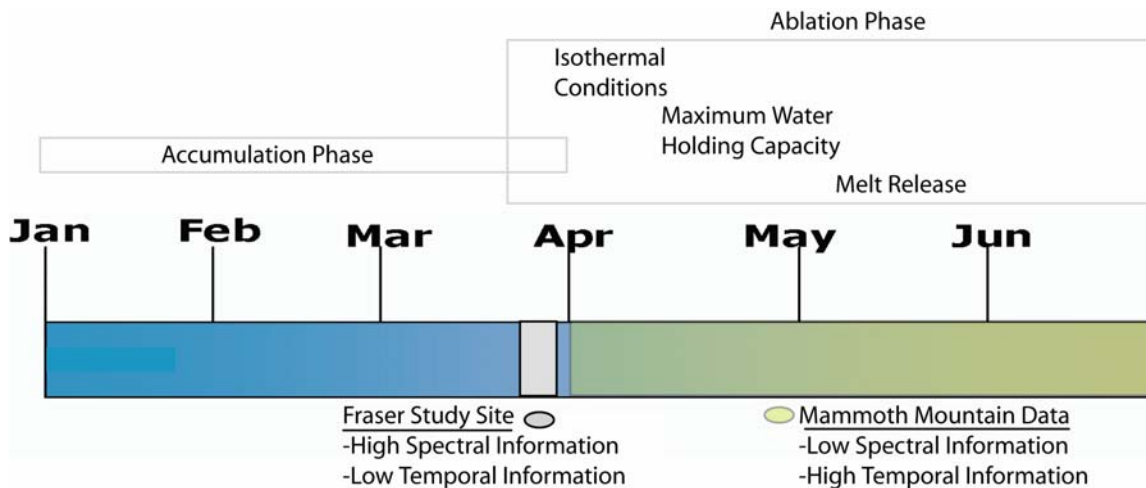


Figure 1: Graphic illustrating two field methods used in this analysis, emphasizing the trade-off between snow surface spectral information and temporal information.

Table I. Comparison of Field Methods

Study Site	Temporal Resolution	Spectral Resolution	Measurements
MMCS (Automated)	Interval: Daily Range: (1 week) 4/1/02- 7/1/02	Interval: (Integrated) Range: 0.2-2.8 μ m	albedo snow depth surface/avg temp discharge
Fraser (Manual)	Interval: Daily Range: (4 months) 3/22/04-3/26/04 (excl. 3/24/04)	Interval: (sampled at 0.001 μ m intervals) Range: 0.35-2.5 μ m	surface reflectance surface/avg temp stratigraphy

3.1 Field Sites

3.1.1 Fraser Field Sites

Two test sites were used in the Fraser region for the collection of data. Site 1 (S1) Berthoud Pass SNOTel site and site 2 (S2) Robber's Roost roadside pullout and trailhead. Figure 2 details the location of each test site relative to NASA's Cold Land Processes Experiment (CLPX) Fraser test regions. S1 is at an elevation of 3447 meters, while S2 is at an elevation of 2965 meters. The test sites are characterized by similar vegetation composition and terrain as those in the CLPX Fraser study regions (described in chapter 2). Both sites are characterized as large clearings on terrain with slopes $\leq 10^\circ$. S1 has a southeast facing aspect while S2 faces northwest (Figure 3).

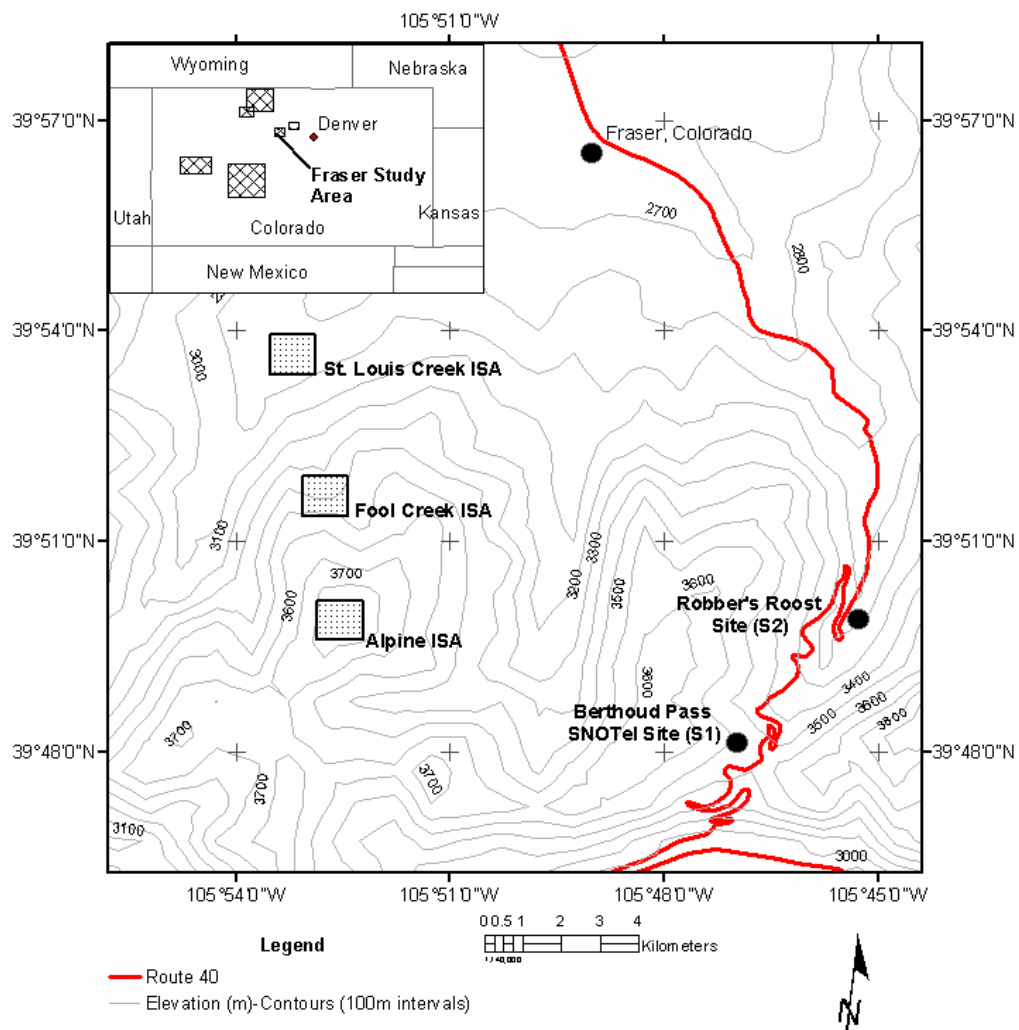


Figure 2: Location of field sites (S1 and S2) used to track snow surface spectral features and stratigraphic changes from March 22, 2004 through March 26, 2004.



Figure 3: Images of field sites: a) view of S1 looking northwest at the Berthoud Pass SNOTel installation, b) view of S2 looking southeast away from Rt. 40 at the Robber's Roost trailhead.

3.1.2 MMCS Field Site

The MMCS site is an installation of automated sensors designed to monitor energy budget conditions. The Site is in Mammoth Mountain (N37°37' W119° 2') at an elevation of 2940 meters in the eastern Sierra Nevada, California. This site has been a cooperative research field station since the 1960's involving the U.S. Forest Service, California Cooperative Snow Survey, Mammoth Mountain Ski Area, U.S. Army's Cold Regions Research and Engineering Laboratory, and the University of California, Donald Bren School of Environmental Science and Management (Figure 4).

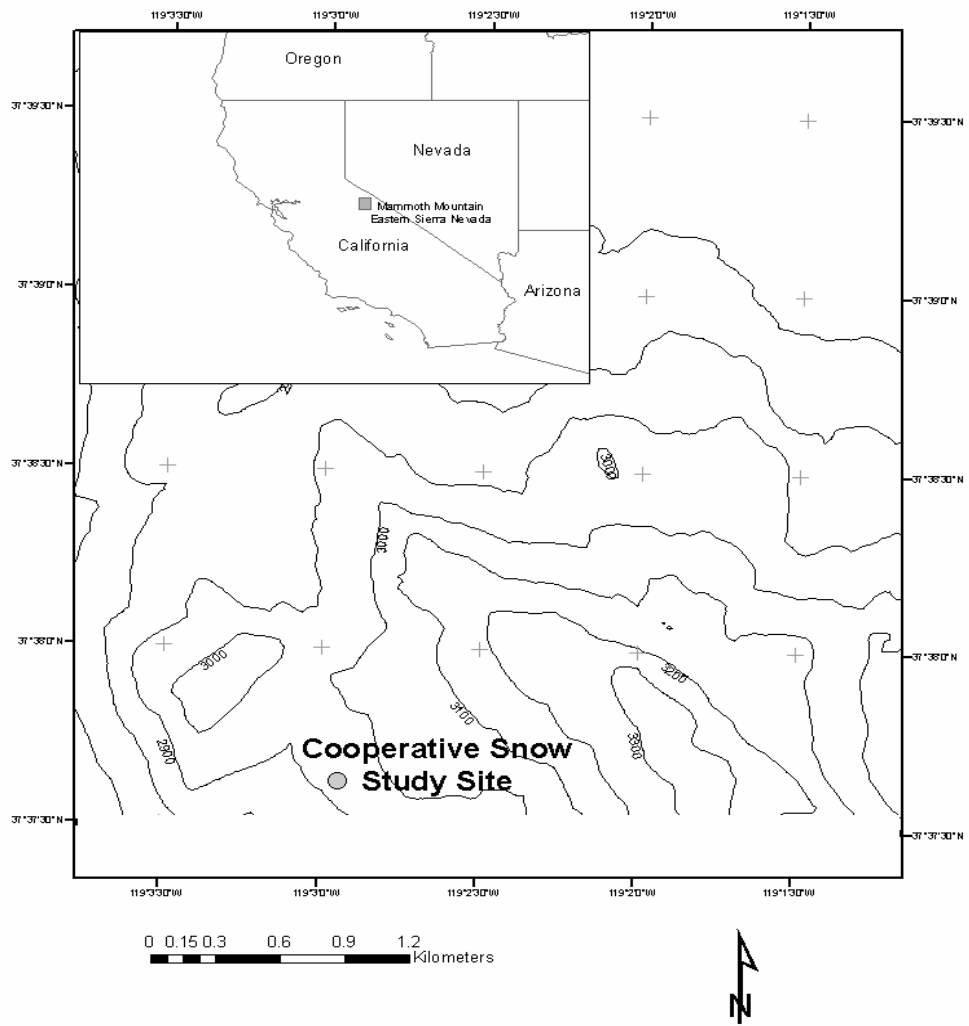


Figure 4: Location of MMCS test site on Mammoth Mountain in the Sierra Nevada Range, California.

3.2 Fraser Site Acquisitions

Spectral measurements were acquired at the two sites near Fraser, Colorado using a high spectral resolution field spectrometer operating in the visible and near-infrared (VNIR) manufactured by Analytical Spectral Devices, Inc. (ASD). Measurements at each site were taken using the portable ASD with an 8° field of view and a standard National Institute of Standards and Technology (NIST-traceable) spectralon reference panel (Table II). The location of each measurement is depicted in Appendix B for each site and day. Spectra collected for each day were averaged for each site. Measurements were timed to maximize the magnitude of solar irradiance.

Table II. Fraser Site Spectral Measurement Characteristics

Date	Time	Number of Collections	Sky Conditions
3/22	(S1) 2:00pm (S2) 4:00pm	3	(S1) clear (S2) overcast
3/23	(S1) 4:00pm (S2) 12:10pm	3	(S1) clear to partly cloudy (S2) partly cloudy
3/25	(S1) 3:10pm (S2) 1:15pm	4	(S1) partly cloudy (S2) partly cloudy
3/26	(S1) 2:10pm (S2) 12:30pm	(S1) 4 (S2) 6	(S1) partly cloudy (S2) clear, thin high cirrus

S1=Site 1, S2=Site 2

Several snow pits were dug each day at each site preceding collection of snow surface reflectance data. At each pit, maximum snow depth (from surface to exposed ground), temperature (in 10cm increments), stratigraphic structure (layer sequences, crusts, and grain size facies), and surface wetness were recorded. A single long-term temperature array was deployed at the Berthoud Pass site for the entire week (Figure 5).

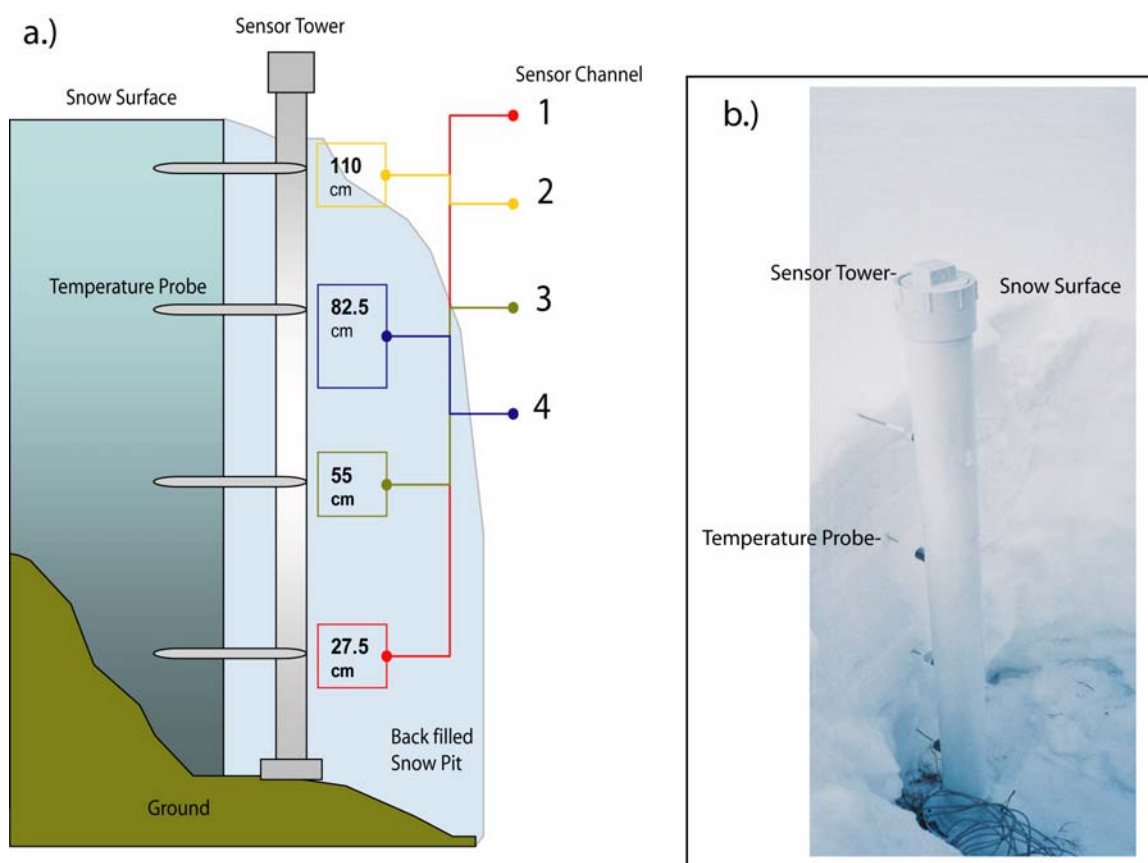


Figure 5: Graphic (a), photograph (b) demonstrating profile of long-term temperature profile monitoring. Temperature probes were set at specified depths and installed in PVC pipe tower (sensor tower). Sensor tower was placed in excavated snow pit at S1 then back filled with snow. Probes monitored temperature continuously at 30 minute intervals from March 22, 2004 through March 27, 2004.

The temperature tower was constructed from PVC pipe and installed in a 110 cm pit with four HOBO[®] standard temperature probes inserted into the undisturbed snow pit wall at 110, 82.5, 55, and 27.5 cm from the ground. The PVC casing was designed with a slot that facilitated adjustable height settings of each temperature probe. The casing was painted white to increase reflectance and reduce its absorption and longwave emission. Once the temperature tower was inserted into the pit, the pit was back filled. All temperature probes were connected to a data logger, which was set to record temperature from each probe in 30-minute intervals. The temperature array was deployed on March 22, 2004 and retrieved on March 27, 2004.

3.3 MMCS Data

Surface temperature, temperature at fixed depths, incoming and outgoing shortwave radiation (0.285-2.8 μ m), snow depth, and snow pack melt discharge were downloaded from the MMCS archive. These variables were downloaded for the ablation season of 2002 starting from April 1. This year was selected because the variables of interest were most complete across the melt season except for surface temperature, which did not have data until Day 92. MMCS variables, their initial measurement intervals, units, and temporal range are listed in Table III. All variables were averaged to daily intervals. Albedo was calculated using incoming and outgoing shortwave radiation. Nominal depths of internal pack temperature sensors were 0.1, 0.25, and 0.5 meters. Average internal pack was computed using temperature data from these depth measurements during the entire analysis period. The following dates registered zero incoming and outgoing radiation and were consequently removed from all variables: 71, 81, 91, 101,

111, 130, and 168. Snow depth measurements used in this analysis were those derived from a depth sounder mounted approximately 5.6 meters above ground on an I-beam arm. Outflow measurements were averaged from 10 ground-level discharge sensors deployed on the south end of the sensor complex and 8 on the north.

Table III. MMCS Measurement Characteristics

Variable	Archived Measurement Intervals (minutes)	Temporal Range (Day of Year)	Measurement Units
Incoming/Outgoing Shortwave Radiation	15	62-182	W/m ²
Snow Depth	15	62-182	cm
Average Pack Temperature	30	62-182	°C
Surface Temperature	15	92-182	°C
Discharge	30	62-182	Mm/day

4. RESULTS

4.1 Fraser Field Results

Several spectra were acquired at each site per day. Average spectra were computed in addition to root mean square error for each daily acquisition. Relative locations of each sample are depicted in Appendix –Section A. S1 spectra are displayed in Figure 6a. This figure depicts characteristic snow spectra, with high visible/ near infrared (NIR) reflectance (0.3-1.0 μm) and low shortwave infrared (SWIR: 1.0-2.5 μm). There is great variation however in spectra across the analysis period. The magnitude in visible/NIR reflectance as a function of time is not chronological. March 22nd and 25th demonstrate higher visible/NIR reflectance than the 23rd and 26th. SWIR reflectances at S1 illustrate higher values on March 25 and similarly lower values for the remaining days. S2 generally displays characteristic spectra. Figure 7a shows average spectra acquired at S2 during the analysis period. Visible/NIR behaviour at S2 was more complicated than at S1: Shorter wavelength ($\sim 400\text{nm}$) visible reflectance on March 22nd demonstrates the highest reflectance, followed by the 26th, 25th, and 23rd. There was an inversion in reflectance at 446nm, where March 26th and 25th values increase with wavelength. SWIR spectra produce high values on March 25, followed by the 26th, 22nd, and 23rd (primarily around the 1030nm absorption feature). Longer wavelength spectra ($> 1500\text{nm}$) display characteristic low values with little distinction among spectra as a function of day.

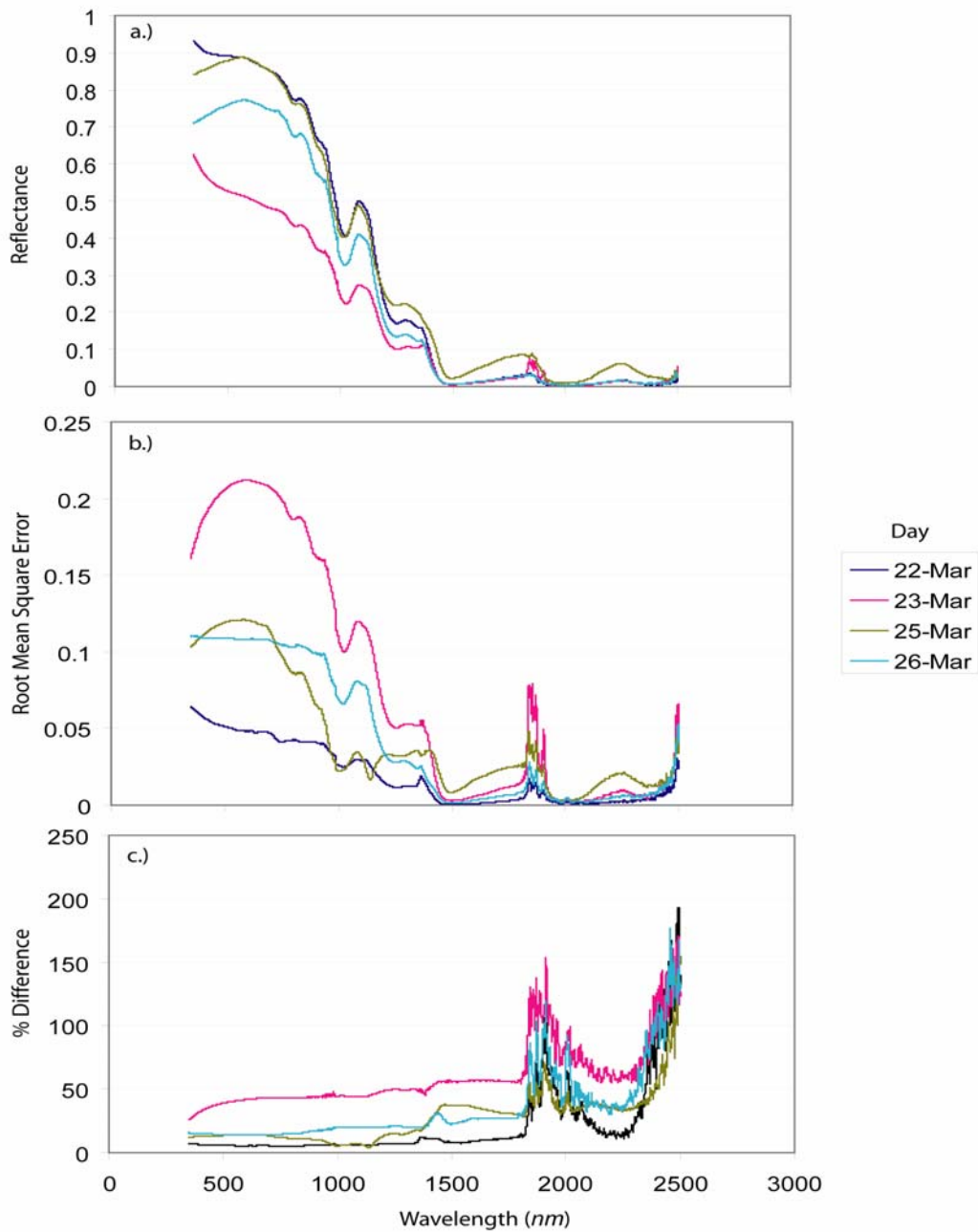


Figure 6: Snow surface spectra from S1 for each day: a) average reflectance derived from separate spectra acquired in various locations within S1, b.) root mean square error (RMSE) of spectra used to compute average reflectance, c.) percent difference ($[\text{RMSE}/\text{average reflectance}] * 100$) between RMSE and average reflectance.

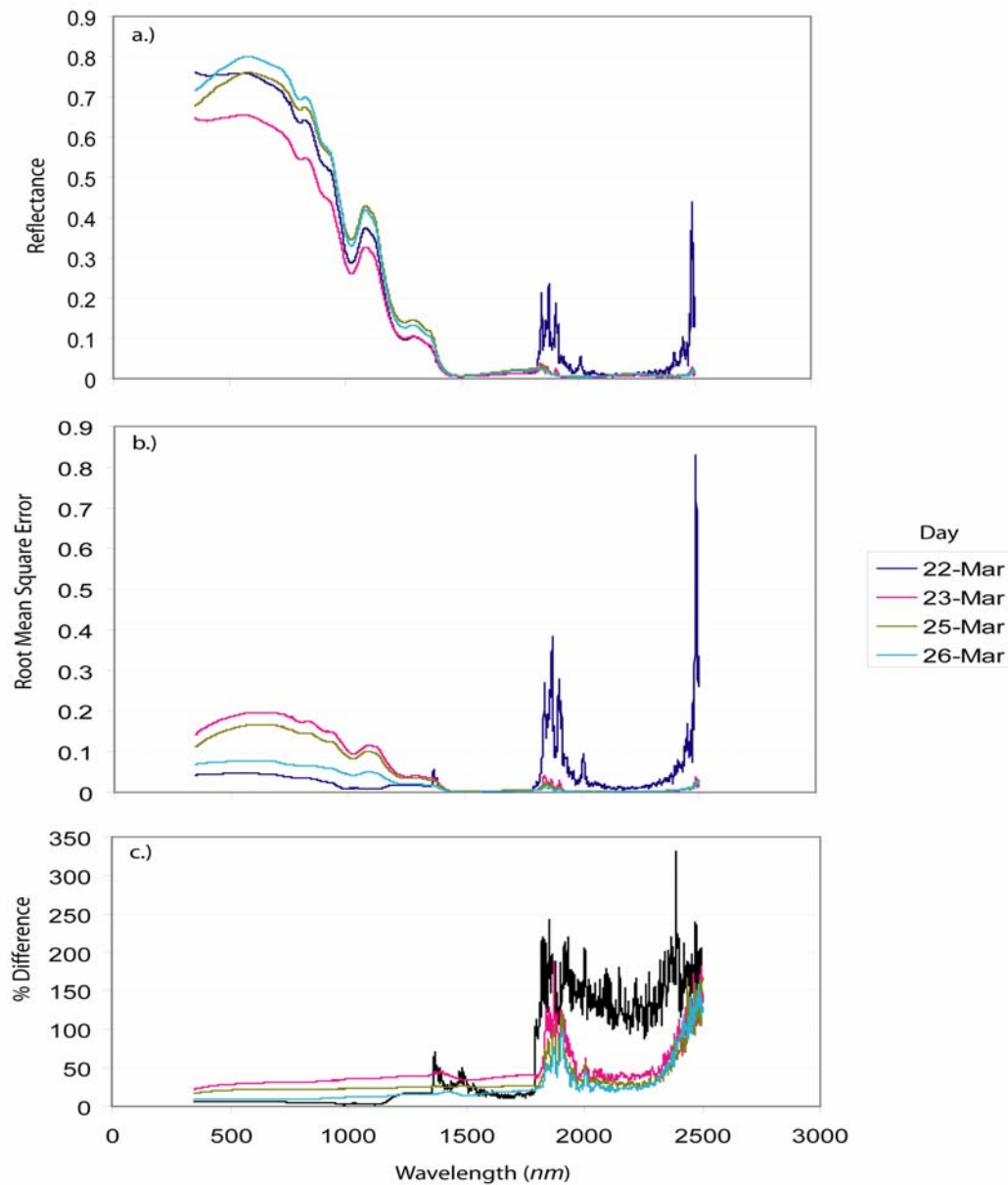


Figure 7: Snow surface spectra from S2 for each day: a) average reflectance derived from separate spectra acquired in various locations within S2, b.) root mean square error (RMSE) of spectra used to compute average reflectance, c.) percent difference ($[\text{RMSE}/\text{average reflectance}] * 100$) between RMSE and average reflectance.

Stratigraphic data derived from snow pits excavated exhibit very dynamic conditions. Daily snow pit data were archived in Appendix B. Each stratigraphy figure is archived by site and date. Various measurements were collected from the excavated pits. Stratigraphic data at S1 on March 22 (see figure S1-1 in Appendix B) indicate a well stratified pack with three distinctive snow facies; densely packed upper pack strata primarily populated by round, sintered grain clusters (primary grain diameters between ~0.1-0.3mm), loosely consolidated mid-level matrix with facet depth hoar grains (diameters between ~1-2mm), and a lower strata dominated by very unconsolidated depth hoar, with larger air filled pore spaces and small sintered hoar fragments (grain diameters ~0.5-1mm). All major strata contain intermittent ice crusts that range in thickness from 1-2 cm. A surface melt freeze crust was present as well. The snow surface condition at the snow pit on March 22nd was characterized as “very wet” with large, well sintered grain clusters ranging from 1-1.5mm in diameter. Maximum depth recorded on this day and site was at 141cm. Snow pack stratigraphy during the analysis period (see figures S1-1 through S1-4 in Appendix B) demonstrated significant changes. March 22nd temperature profile indicated variability in temperature as a function of depth with values ranging between -2 to 0.5° C. March 23rd through March 26th indicated substantial changes in the snow pack. Temperature profiles indicated isothermal conditions reached on March 23rd. Snow pack stratification remained relatively consistent during the week, with the substantial changes in snow surface characterization, proceeding from “very wet” with ~1-1.5mm grain diameters to “saturated” with ~1.5-2mm grain diameters. Ice flow pipes and ice knobs appeared in March 25th stratigraphic data indicating the production of melt and vertical preferential melt flow paths, leading to the soil substrate.

March 26th stratigraphy indicated well developed ice pipes oriented both vertically and horizontally, with horizontal pipes following prominent pre-existing ice crust layers. The distribution of melt structures on the 26th is greater throughout the excavated pit, with flow pipes indicating increased surface melt infiltration.

Stratigraphic data at S2 (see figure S2-1 through S2-4 in Appendix B) demonstrated similar stratification as at S1, with round, sintered clusters in a densely packed matrix in the upper 40cm of the pack (grain diameters ~0.1-0.2mm), mixed sintered rounds in consolidated matrix and some hoar facets in the middle of the pack (1-1.5mm grain diameters), and loose, unconsolidated depth hoar on March 22nd. Surface conditions from March 22nd through the 26th indicated consistently large grains between 1 to 3mm in diameter and “wet” to “very wet/saturated” surface wetness. S2 temperature profiles indicated a pack that was already isothermal during the entire analysis period. There appeared to be faint preferential melt flow structures in the stratigraphy throughout the week. Significant water flowed along the roadside runoff channel, ideally supplied by snowmelt from the adjacent snowfield in the clearing at the Robber’s Roost trailhead on March 26th. Additionally, the base of the excavated snow pits demonstrated damp/wet soil on the last day of the analysis period (March 26th).

Long-term temperature profile data at S1, derived from the apparatus described in figure 5, provided information about temporal changes in the thermodynamic state of the pack. Figure 8 displays temperature at depths listed earlier for the entire analysis period.

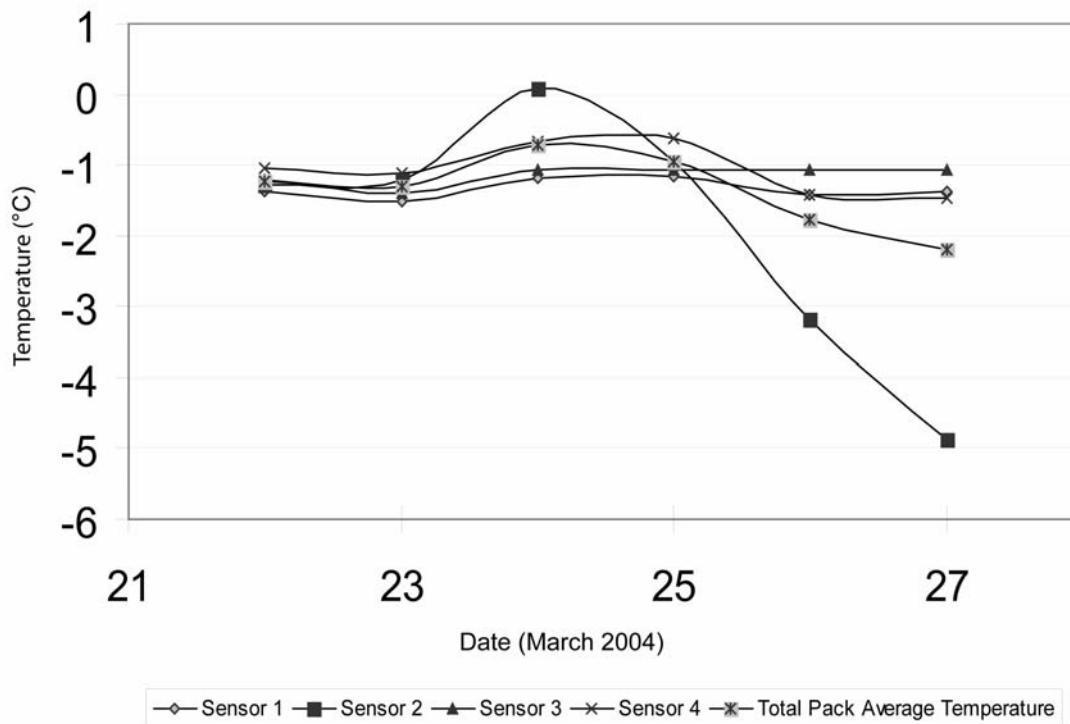


Figure 8: Long-term temperature profile data launched on March 22, 2004 at Site S1 and retrieved on March 27, 2004. Standard temperature probes were inserted into excavated snow pit at 110 (sensor 2), 82.5 (sensor 4), 55 (sensor 3), and 27.5 (sensor 1) cm from the ground. Total pack average temperature was derived from each probe.

Temperature data, collected at each depth in 30-minute intervals, were aggregated to daily temperature measurements. Figure 8 demonstrates an increase in temperature from the 22nd to the 24th, with subsequent decrease from the 24th through the 27th. The magnitude in temperature change during this period varies as a function of depth. Temperatures at a depth of 82.5cm were consistently higher than those at 110, 55 and 27.5cm until the 24th for 110cm and 26th for the remaining depth. The largest fluctuation in temperature occurs at 110cm (surface) with the highest temperature reached on the 24th. Surface temperatures decline rapidly from ~0 to -4 °C after the 24th. Deeper

probes at 55 and 27.5 cm demonstrate the smallest change during the analysis period with temperatures holding close to $\sim -1^{\circ}\text{C}$. Average pack temperature shows the pack moving towards isothermal conditions until the 25th, when average pack temperature becomes cooler, dominated primarily by a rapidly cooling surface.

4.2 MMCS Results

Snow pack state variables were acquired continuously via an automated installation during the 2002 ablation season. Table III summarizes those variables used to track the long-term relationship between snow pack surface optical and thermal properties and those that indicate the internal condition of the pack and its propensity for melt release. Descriptive statistics for computed surface albedo, surface temperature, average pack temperature, snow depth, and pack melt discharge, acquired from the MMCS data archive (Table IV). Descriptive statistics were computed only for a time interval common to variables. This time interval is dictated by the limited surface temperature variable, which only has data from days 92-182. The effective analysis period was reduced further to days 92-155 because by day 155, the snow pack had depleted to a depth where temperature probes were exposed to incoming solar insolation, causing an artificially rapid increase in average temperature (Figure 9).

Table IV. Descriptive Statistics of variables acquired from the MMCS database (N=60)

Variable	Minimum	Maximum	Mean	Standard Deviation
Computed Albedo	0.43	0.84	0.611	0.094
Snow Depth				
Average Pack Temperature				
Surface Temperature	-11.68	12.12	1.29	5.75
Discharge	0.09	5.69	1.89	1.60

Snow depth tends to decrease throughout the time series. Snow surface albedo varies similarly as snow depth. Increases in snow albedo appear partially in phase with snow depth, where both are probably responding to new accumulations. Average pack temperature shows the pack reaching isothermal conditions about day 100 holding at 0°C until approximately day 155. At day 155 average pack temperature increases rapidly and is indicative of the snow pack becoming depleted to a depth (~1m) where buried temperature probes begin to intercept more solar radiation. Once the pack reaches isothermal conditions, snow pack melt discharge signals the onset of melt release. There are approximately three prominent periods where melt discharge tends to increase sharply (day 104, 139, 150). Generally, the discharge time series demonstrates an increasing trend for most of the time series until the period leading to day 169, where melt discharge reduces to zero. Surface temperature displays significant variability with an increasing trend throughout the study period.

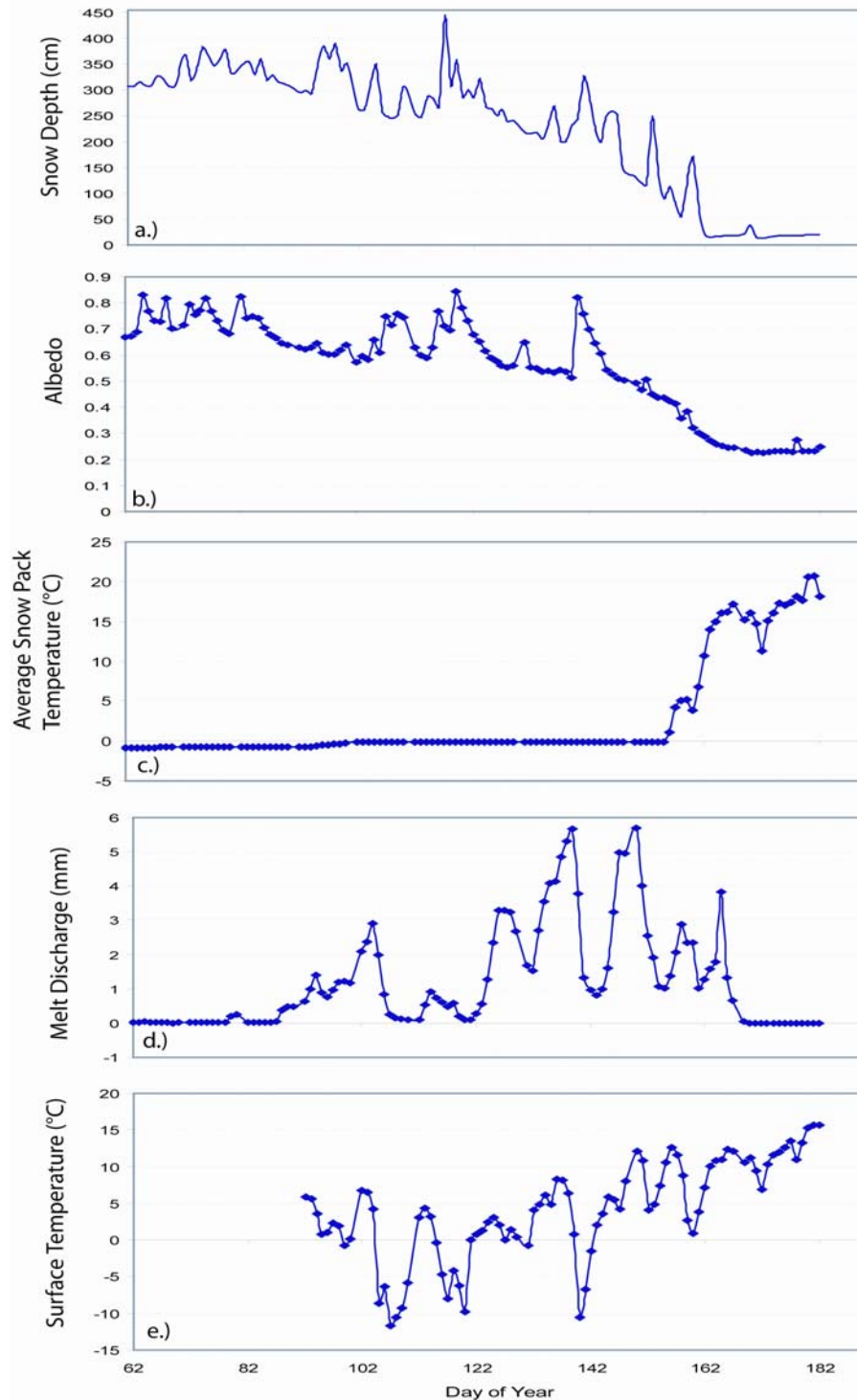


Figure 9: Time series of variables downloaded from MMCS archive in the interval between Day 62-182 (except for surface temperature, which has data from Day 92-182); a.) snow depth, b.) albedo computed from incoming and outgoing radiation, c.) average pack temperature derived from temperature sensors at 0.1, 0.25, and 0.5 meters, d.) melt discharge, and e.) surface temperature.

A primary focus of this analysis is the long-term relationship among snow surface optical and thermal variability and the snow pack propensity for melt. The analysis will focused, therefore, on surface temperature, albedo, and discharge, constrained by the temporal extent of the surface temperature variable and reduced snow depth (day 155). Figure 10 displays histograms of surface temperature, discharge, and albedo for the analysis interval between day 92-155 (N=60).

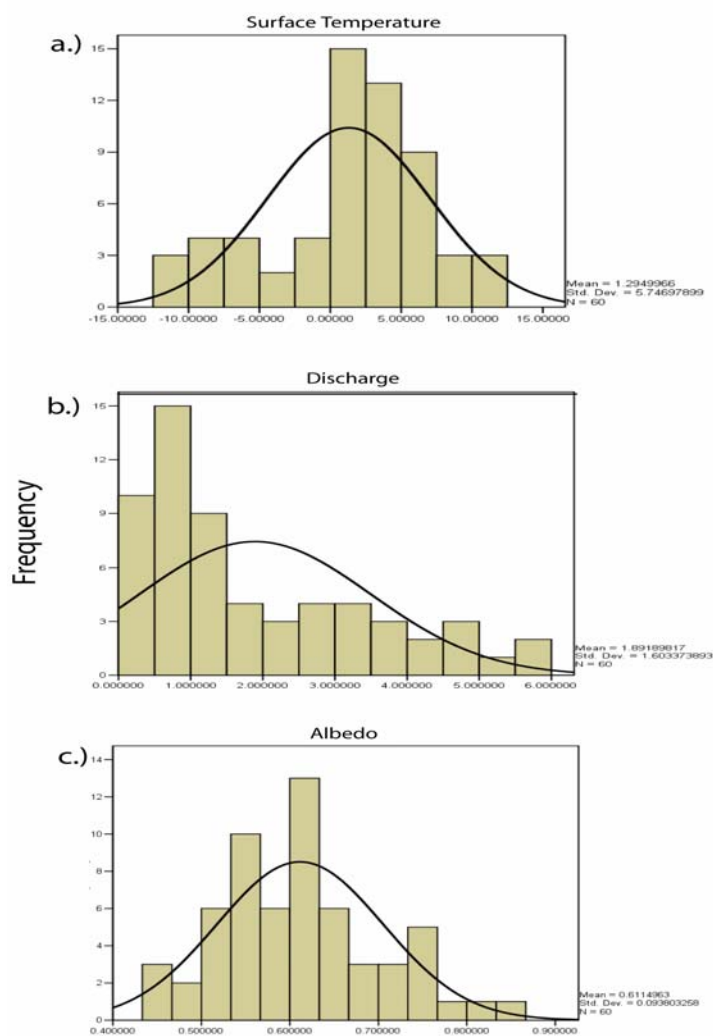


Figure 10: Histograms; a.) surface temperature, b.) melt discharge, and c.) albedo for N=60.

Surface temperature histogram (figure 10a) illustrates a moderately normal distribution that is slightly skewed towards higher temperatures. Melt discharge (figure 10b) is more platykurtic and skewed heavily towards lower melt values. Albedo demonstrates a slightly bimodal distribution (figure 10c) with peak frequency near 0.6 and the next highest frequency near 0.55. This slight bimodal behaviour in the albedo time series is evident in figure 9, where albedo fluctuates between higher and lower values, primarily as a function of possible new snowfall events. These intermittent accumulation events momentarily increase albedo, which subsequently decreases as the surface ages.

4.2.1 Time Series Analysis of Albedo, Discharge, and Surface Temperature

Time series analysis includes determination of Pearson's r correlation coefficient, univariate autocorrelation, bivariate cross-correlation, and cross-spectral analysis. Correlation coefficient (r) was calculated between albedo and discharge as well as surface temperature and discharge to determine the strength and direction of the relationship separately between albedo and surface temperature to pack melt release. A correlation coefficient of -0.639 was reported between discharge and albedo, while $r = 0.567$ between surface temperature and discharge.

Truncated (day 92-155) albedo, discharge, and surface temperature time series were detrended assuming a linear trend for each time series. The detrending process involved fitting a linear trend line through a least-squares regression routine. Regression residuals were considered times series corrected for trend. Detrended series were used in

subsequent time series analysis. Each detrended series served as input into an SPSS autocorrelation routine. Maximum lag for each series was approximately determined to be $N_{\max}/4$, where N_{\max} is the maximum length of the time series. Given $N_{\max}=60$ for each series, the maximum lag used was 16. Figure 11 depicts autocorrelation functions for each detrended variable. The largest lag correlation for albedo, discharge, and surface temperature is one day. The next highest lag for all three variables is at a two-day lag. Each variable displays a cyclic pattern in the lagged correlations with statistically significant positive and negative correlations at various intervals. The strength of these patterns is different for each variable. Cyclic patterns appear to be more pronounced for discharge and surface temperature than albedo. Albedo demonstrates the next highest negatively correlated lag (starting from a lag of zero) is approximately at day 12. Maximum discharge and surface temperature correlations cycle through negative and positive phases at approximately days 6, 10, and 16. Both the 6 and 10-day lags appear to be statistically insignificant in the surface temperature case.

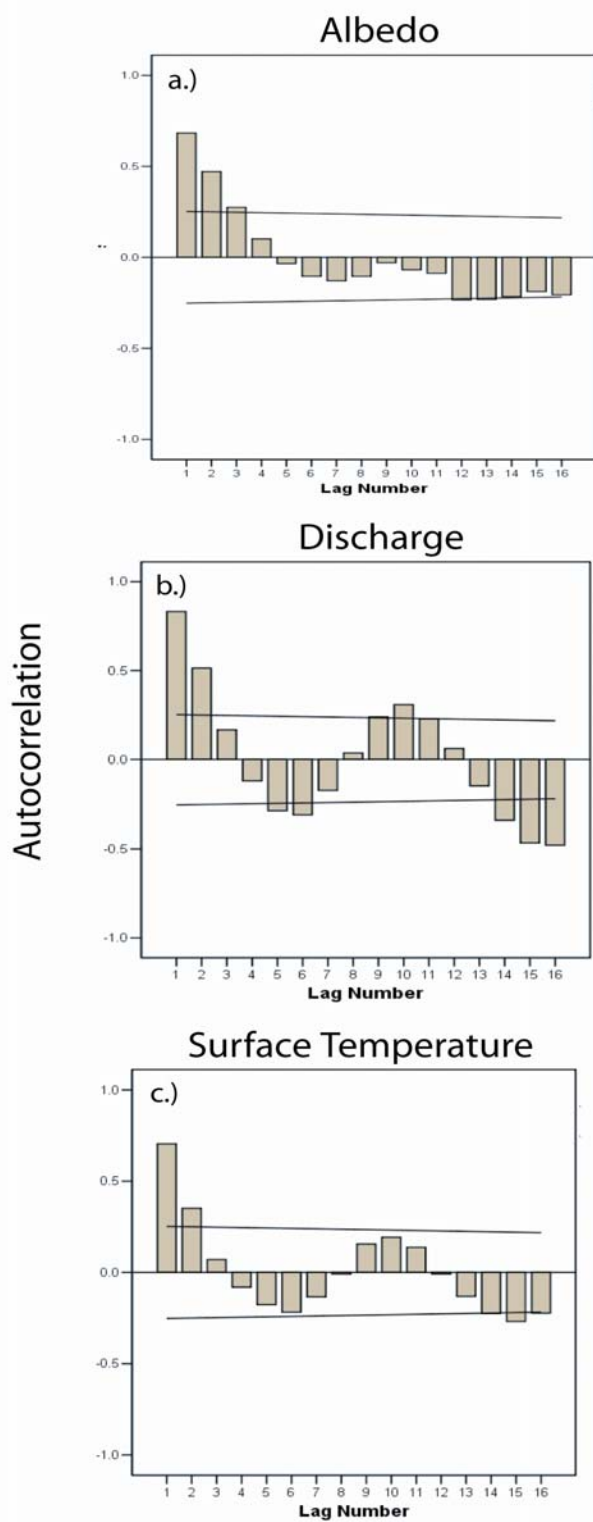


Figure 11: Univariate autocorrelations of detrended MMCS variables (N=60) at 16 day lags; a.) albedo, b.) melt discharge, and c.) surface temperature.

Cross-Correlation analysis was used to examine the temporal relationship between albedo and surface temperature, separately with melt discharge. Detrended series were input into an SPSS cross-correlation routine. Figure 12 displays results from this analysis.

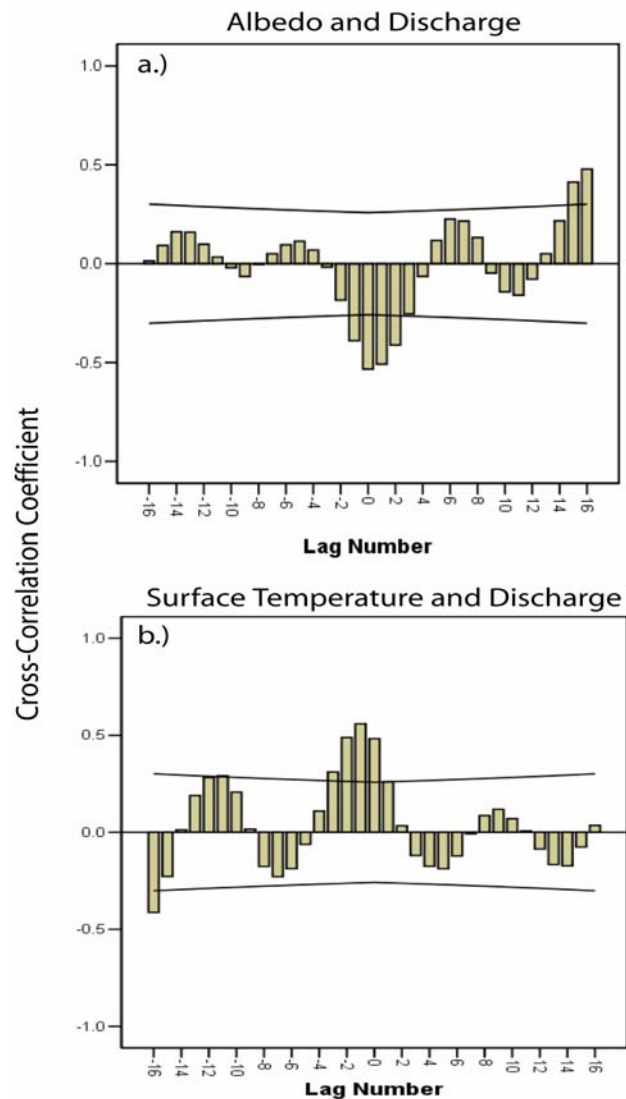


Figure 12: Cross-correlations of detrended MMCS variables (N=60) at 16 day lags; a.) albedo and discharge cross-correlation, b.) surface temperature and discharge cross-correlation.

Albedo and melt discharge cross-correlations indicate the strongest negative correlation at approximately (-1) day lag. A negative (+1) day lag appears to be the next highest correlation. Generally, lagged cross-correlations between albedo and discharge appear to be cyclic with periods of correlations cycling between positive and negative with the largest lagged correlation at +16 days. A comparable cyclic pattern appears in the cross-correlation between surface temperature and discharge. These cyclic patterns in both bivariate correlations are generally statistically insignificant and are therefore considered random. The maximum correlation was at a positive (-1) day lag.

Cross-spectral analysis has the capacity to reveal potential coordinated (or uncoordinated) cycles in one or more times series. The cross-correlation analysis is essentially the cross-product of two univariate spectra. Generally, the cross-spectral output can be the result of the application of a discrete Fourier transform of the lagged cross-correlation function between two time series. The complex output from such an analysis is not easily interpretable and therefore is expressed as an estimate of bivariate coherency and phase for each $N/2$ frequencies in the spectrum. Coherency indicates the percentage of shared variance between the two times series at a given frequency. Phase indicates the timing of time series amplitudes (peaks) in time series A with time series B at a given frequency. Figure 13 displays coherency and phase plots for albedo, surface temperature, and discharge. Detrended time series were smoothed with a 3x Hamming filter.

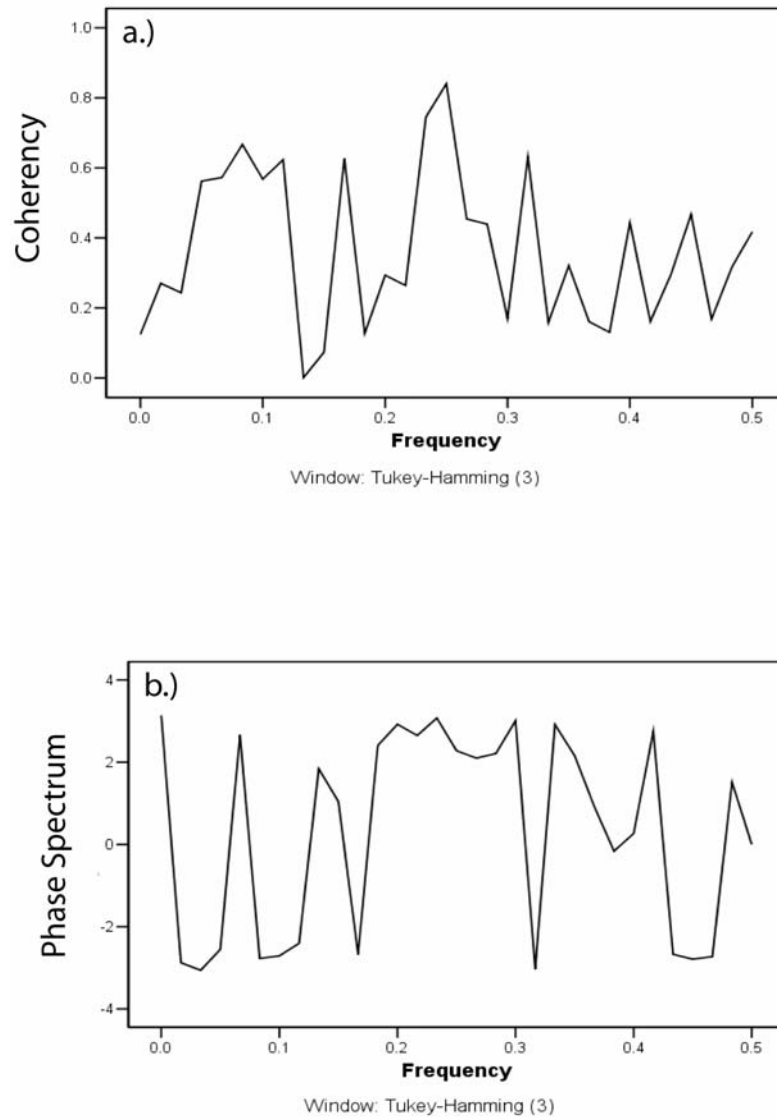


Figure 13: Cross-spectral plots of detrended albedo and discharge (N=60); a.) coherency, b.) phase.

Figure 13 demonstrates maximum coherency between albedo and discharge at approximately a frequency of 0.25 (period of 4 days). Phase spectrum for albedo and discharge appears to be strong over several frequencies. There are several spikes in the phase spectrum (at approximately 0, 0.6, 0.14, 0.33, 0.41 and 0.49), but the largest range in frequencies appears to be between 0.175 and 0.32. Figure 14 depicts phase and coherency for surface temperature and discharge.

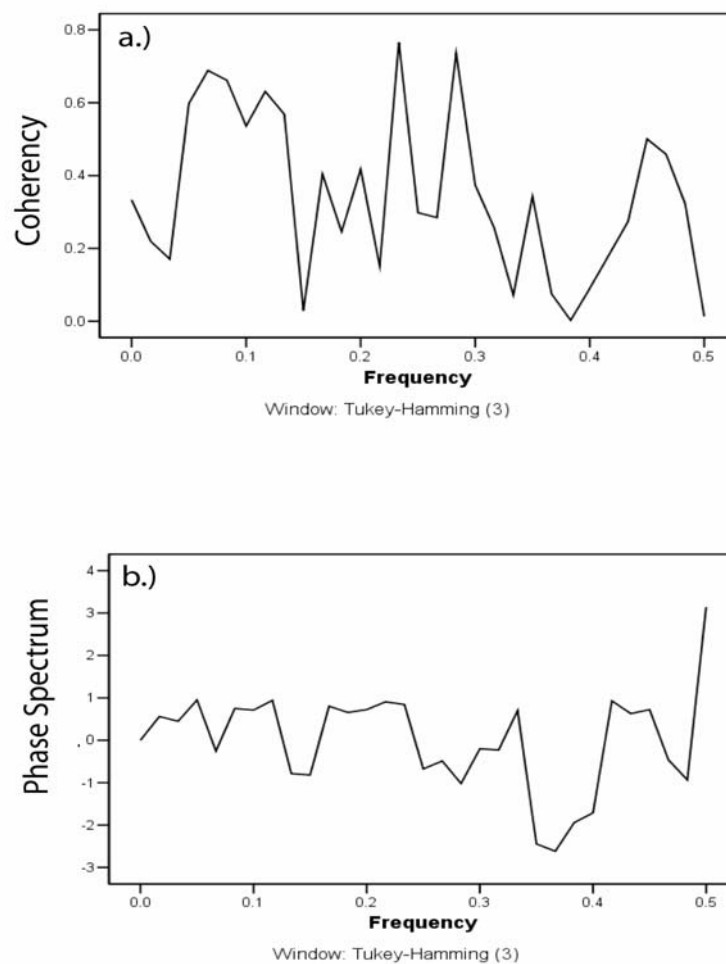


Figure 14: Cross-spectral plots of detrended surface temperature and discharge (N=60); a.) coherency, b.) phase.

Surface temperature and discharge coherency demonstrates maximum at approximate frequency of 0.24 (4 day period). Additionally, large coherency values occur at approximate frequencies of 0.28 (3.5 day period), and 0.07 (14 day period). Phase spectrum (figure 14) demonstrated less period coupling than albedo and discharge, with maximum phase near 0.5.

Time series analysis indicates periods of temporal coupling between surface albedo, discharge, and surface temperature and discharge. Understanding the strength of temporal coupling among these variables throughout the ablation season is paramount in determining the utility of the near surface moisture index (NSMI) to track snow pack melt release. Through standardizing (with trend) albedo, surface temperatures, and discharge time series, direct comparison of series behaviour is possible. Figure 15 illustrates a radar graph of standardized albedo, surface temperature, and discharge as a function of time. The time axis (represented as the outside dial) spans from day 92-155. The most interesting pattern in figure 15 is the relationships between the optical and thermal fluctuations of the snow surface with the occurrence of melt discharge. Increases in melt discharge are associated with decreases in albedo and increases in surface temperature. Periods when this pattern is the most prominent are approximately at day(s) 104, 125-129, 138, and 148.

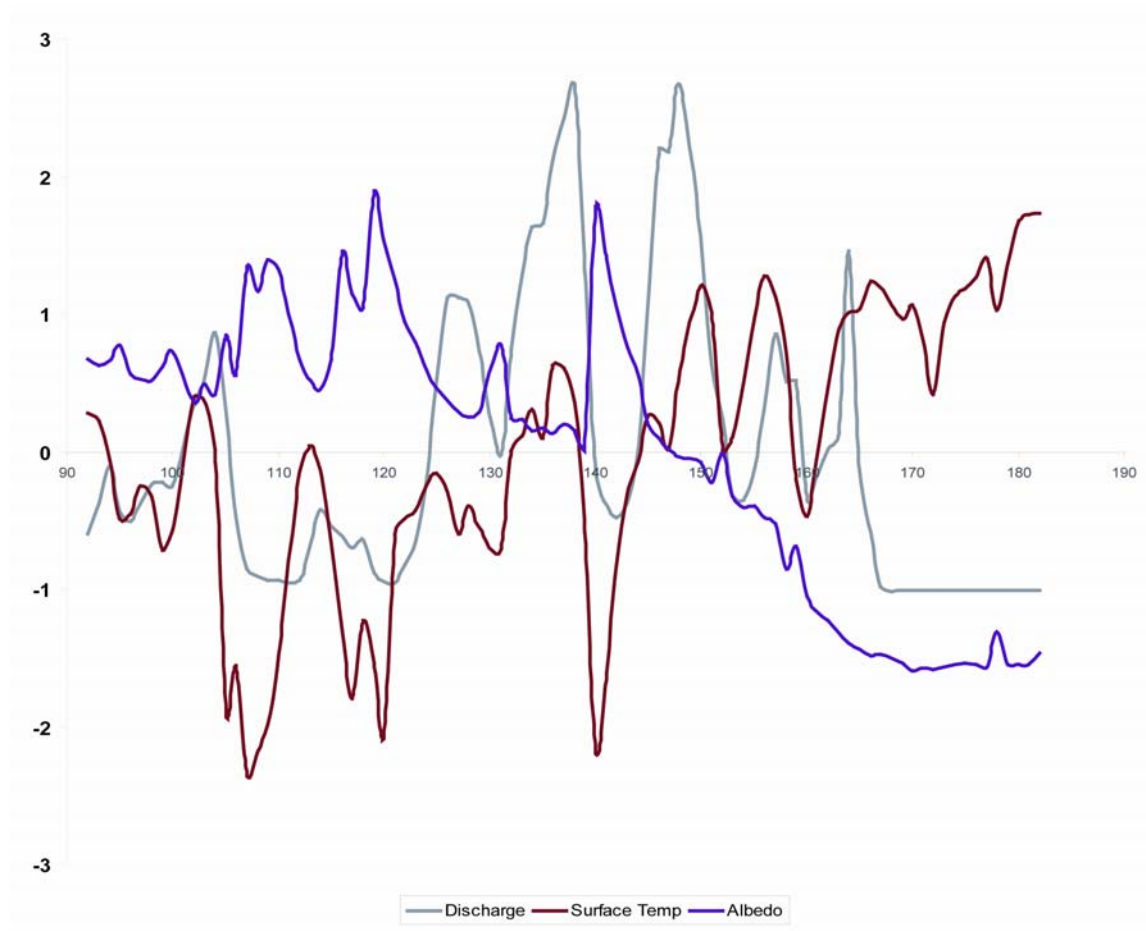


Figure 15 Plot of standardized albedo, surface temperature, and discharge as a function of time (day of year).

4.3 Simulated Time-Dependent NSMI using MMCS Data

In an attempt to further understand the usefulness of snow surface information in tracking the timing of snow melt release, a simulated NSMI was constructed by plotting the MMCS albedo and surface temperature variables between day 92-155 in a bispectral feature space. Data from these two variables were aggregated into 4-day means and plotted as albedo vs. surface temperature. A 4-day compositing period was used based on time series analysis that generally indicated such a period exhibited significant strength between snow surface properties and discharge. Figure 16 illustrates simulated NSMI using MMCS data.

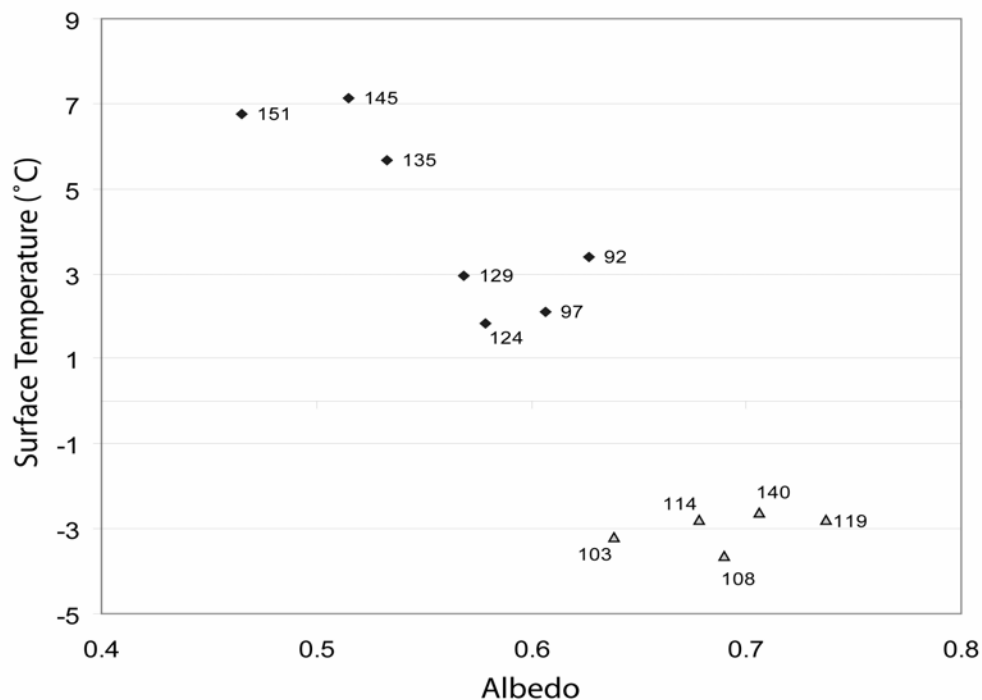


Figure 16: Simulated NSMI using MMCS albedo and surface temperature data composited using 4 day mean intervals in the temporal range between day92-155. Compositing period is marked over the plotted points. Triangle (Δ) dates are those that did not follow expected pattern of

increasing temperature and decreasing albedo as a function of time.

Simulated NSMI is actually an optical/thermal feature space populated with information about the change in the snow pack state as a function of time (indicated by the compositing date over the the plotted points in figure 16). Radiative simulations of NSMI, as well as satellite measured NSMI, we might expect an increase in surface temperature and decrease in albedo as the snowmelt season progresses (Lampkin and Yool, 2005). This general trend is illustrated in figure 16, but there are some exceptions: Those points marked by triangles (Δ) indicate a deviation from expect NSMI behaviour in surface properties as a function of time. These points are periods where albedo increased and surface temperature decreased. Points marked as diamonds (\blacklozenge) indicate behaviour consistent with expected theory.

5. DISCUSSION

Data collected from the Fraser site and those derived from the MMCS data set are separated by space and time, but were considered a single observation in the attempt to monitor the snowmelt process. The logistics of acquiring high spectral and stratigraphic resolution on daily time scale (as the Fraser data were collected) was not possible. MMCS data set provided a much longer temporal record, but at a cost. There was a substantial loss in spectral and stratigraphic detail, requiring use of coarse snow surface albedo, and surface temperature as surrogates. Additionally, average pack temperature derived from the MMCS database was used as a surrogate for overall internal state of the snowpack. Conditions at the Fraser research sites are surely different than those at the MMCS automated research site in terms of elevation, depositional regime, geographic location, and year. The link between these two sites is the snowmelt process. Equations [1-5] detail a process that is common to each snow pack, no matter the time, place or locations. It is well documented (Marks et al., 1 and 2, 1992; and many others] that topography, solar radiation, and deposition environment are all very important in controlling the rate, duration, and spatial distribution of melt, but the physics underlying melt process are key in spite of these other factors. It is reasonable; therefore to treat the body of data derived from both Fraser and MMCS as a single collection of evidence in the context of improved monitoring of the snowmelt process, particularly in the interest of demonstrating how snow surface optical and thermal properties can be used to track snow pack melt release events.

Incident solar radiation is partly reflected at a snow surface, but also penetrates and is absorbed within the snow cover, influencing internal thermal conditions, snow pack temperature profile, and snow melting processes (Fukami et. al, 1985). Figures 6 and 7 illustrate surface reflectance spectra collected at the Fraser sites. Variability of snow surface reflectance was generally correlated with changes in the internal structure of the snow pack indicative of melt conditions (Appendix B). Visible/NIR signatures varied according to optical radiative theory (Figures 6 and 7), which indicate as melt progresses entrained liquid water within the snow pack matrix tends to increase grain size. Grain clusters form quickly, decreasing reflectance (Davis et al., 1993). If the snow pack at S1 and S2 sites was continuously experiencing aging and melt (particularly surface optical changes due to melt, given these sites achieved isothermal conditions) then visible/NIR and SWIR reflectance would decline at comparable magnitudes (both sites did not contain any surface litter such as soot or branches). This is not the case and is represented in figures 6 and 7. There are days (March 25, and 26 at S1 and S2) that are not in a sequence consistent with the above expectations. This is due to observed new snowfall events on both days. Such events tend to decouple changes in surface optical properties from changes in internal state of the snow pack responsible for the production of melt. Stratigraphic data (particularly at S1) indicate that during these two days (March 25 and 26), melt production continued as evident by developing preferential flow structures. Berthoud Summit SNOTel data (station at S1 in figure 3a) validates changes observed in stratigraphic, spectral, and temperature data collected at S1. Figure 17 illustrates Berthoud Summit SNOTel snow water equivalent, accumulated precipitation,

and air temperature during the 2004 snow season from October 1, 2003 through July 1, 2004.

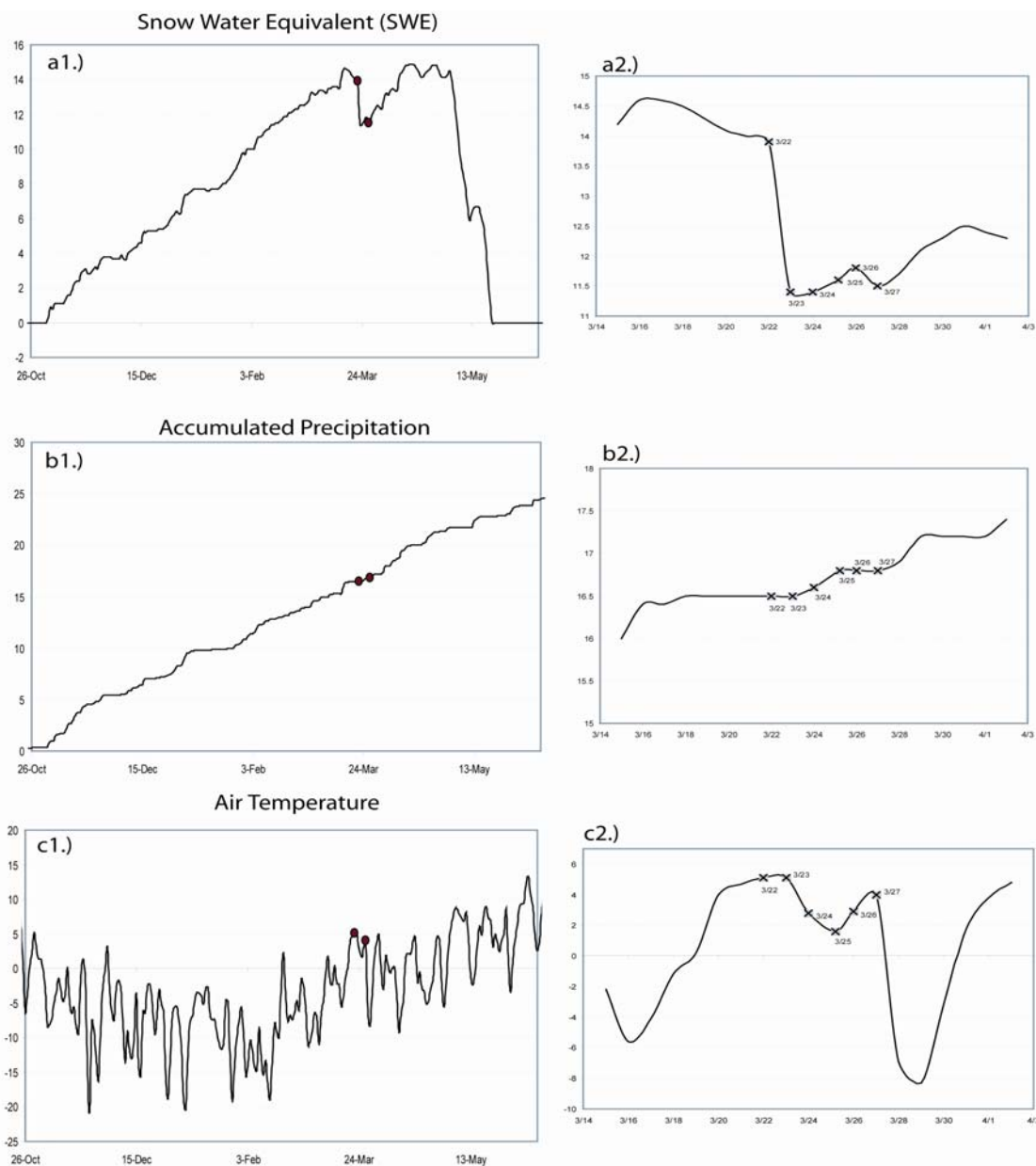


Figure 17: Berthoud Summit SNOTel data during entire snow season (October 1, 2003-July 1, 2004) and subset during the Fraser study period (March 22-27, 2004); a.) snow water equivalent (inches)-(1) entire season, (2) subset, b.) accumulated precipitation (inches)-(1) entire season, (2) subset, c.) air temperature (°C)-(1) entire season, (2) subset. Red dots indicate extent of subsets.

Unlike the visible region of the EM spectrum, absorption tends to dominate in the SWIR as a function of snow grain size and is particularly evident from 0.8-1.2 μm and 1.8-2.2 μm . These portions of the EM spectrum correspond to local minima in the absorption coefficient of ice (Kay et al., 2003). Changes in ground spectra at the Fraser sites indicate a strong response in 0.8-1.2 μm region, and an increase in noise (see figure 6c and 7c illustrating standardized RMSE) reducing the fidelity of the signal in the 1.8-2.2 μm region. Surface and internal pack state decoupling is supported further during the later part of the week, given a decrease in average pack temperature monitored by the long-term monitoring column (figure 8). It appears that a weather system characterized by increased precipitation and cooler air entered the region during the later part of the week, interrupting surface-pack coupling. The nature of coupling and decoupling events over a longer period were examined through the MMCS data set. Cross-correlation analysis between albedo and discharge (figure 12a) indicates lagged correlations that appear cyclic in nature. Cross-correlation between these two variables was strongest at (-1) day lag and was negative. Therefore, albedo leads in time over melt discharge. A similar result occurred in cross-correlation analysis between surface temperature and discharge (figure 12b). Surface temperature cross-correlations with discharge differed from that between albedo and discharge in that surface temperature was correlated positively with discharge. Coherency and phase plots derived from cross-spectral analysis indicate other patterns of temporal coupling between snow surface optical and thermal changes with melt release during the study interval. In the context of this analysis, coherency can be interpreted largely as the proportion of variance in discharge predictable from variance in surface temperature (or albedo) within each

frequency band. Albedo and discharge (figure 13a) demonstrate quite high coherency across a range of low (~ 0.03 - 0.14) and mid-range (~ 0.21 - 0.3) frequencies. Maximum coherency (~ 0.90) was approximately 0.25, suggesting that $\sim 90\%$ of variance in discharge was predictable by albedo at this frequency. A 4 day period in albedo tends to explain the largest proportion of variance in discharge. Coherency (~ 0.75) between surface temperature and discharge indicate a maximum at ~ 0.23 or 4 day period as well. Phase spectrum for albedo and discharge (figure 13b) at the frequency of maximum coherency was approximately $+3.00$ radians, corresponding to a value short of $+\pi$. Dividing by 2π to convert from radians to proportions of a cycle means that if these times series were continuous sinusoidal waves, they would be approximately a half of cycle out of phase. This would indicate that the troughs of one series would almost correspond to the peaks of the other. This indicates a nearly inverse relationship between albedo and discharge and is confirmed by a negative unlagged correlation. Surface temperature and discharge phase (figure 14b) at the maximum coherency frequency of ~ 0.23 appears to be approximately $+0.4$ radians corresponding to 0.05 fractions of a cycle. Such a low value indicates that if these two series were again sinusoidal waves, that they would be nearly in complete phase with each other and indicate that these series vary proportionally to each other as supported by a positive unlagged correlation.

Standardized albedo, surface temperature, and discharge, were plotted (figure 15) and clearly indicate two necessary changes in both temperature and albedo for significant snow pack melt release. A decrease in albedo and increase in surface temperature are required for melt production and release. This condition is obvious on day(s) 104, 125-

129, 138, and 148. Given the entire pack is isothermal during this period, the role albedo plays appears to be critical in mediating melt release in almost a mechanical fashion. As examples, surface temperatures increase and albedo either increases or remains constant on day(s) 199 and 148. These periods demonstrate no spikes in melt discharge. Several days (105, 117, and 140) display opposite changes in albedo (increase) and temperature (decrease) with a corresponding decrease in melt discharge. These dates all correspond to increases in snow depth (figure 9a) and indicate new snowfall events. It is not clear whether it is required for albedo to decrease only to elicit melt production and discharge. An instance in figure 15 that demonstrates this concept is the increase in melt discharge during the interval between day 125 and 128: The magnitude of change in surface temperature during this period is small and effectively constant, while albedo decreases gradually between day 119 and 127. It may be that the magnitude of melt discharge is enhanced by increases in surface temperature commensurate with decreases in albedo, while the timing of melt production is more heavily contingent on variations in albedo.

It is well known that surface albedo determines the amount of solar radiation that is reflected back to space (Winther et al., 1999). Shortwave energy has the capacity to penetrate deeply into the snow pack, as a function of being weakly absorbed and strongly forward scattered. Incident photons not reflected from the snow surface are transmitted, absorbed in ice grains, and converted to heat (Dozier et al., 1989). Given the effective thermal diffusivity of snow is low, this heat energy will be retained at depth and used to convert snow to melt water once isothermal conditions are reached. In the near infrared,

ice is moderately absorptive; therefore reflectance is sensitive to grain size, particularly between 1.0-1.3 μm (Dozier et. al, 1989). These radiative transfer processes establish how structural changes in the near surface mitigate the amount of incoming energy available for conversion to heat and subsequently melt.

Figure 16 depicts a time-dependent NSMI derived from the MMCS ground data (using albedo directly as a proxy for a snow grain size index and surface temperature). This time-dependent NSMI demonstrates trajectory of the snow pack through optical/thermal feature space. It is expected that as time advances the trajectory of the evolving snow pack should track from the high albedo/low temperature region of the feature space to low albedo/high temperature region. Days marked in circles largely track through the feature space according to our expectations. Those marked in triangles are the exception. Triangle-marked days appear to track to higher albedo/lower surface temperature regions out of an expected sequence. These days indicate that as the pack ages, later into the spring season, instead of decreasing albedo and increasing temperature, the opposite occurs. It appears these anomalous days coincide with periods when snow depth has increased due to new snowfall events. These events tend to shift the feature space mapping of an evolving pack towards conditions expected earlier in the melt season. Since this behaviour was exhibited over a 4-day lag, the simulated NSMI has demonstrated variability potentially correlated with inter-seasonal variation due to synoptic scale climatology (precipitation events). Serreze et al. (2001) examined large snowfall events using 24-hour positive daily Snow water equivalence (SWE) measurements from regionally grouped SNOTEL station measurements. They assume

that significant snowfall events can last for multiple days. Event lengths based on consecutive positive daily SWE changes were derived for each SNOTEL station. Results reveal that 75% (Pacific Northwest)-89% (Arizona/New Mexico) of events are of 3-day durations or less (Serreze et al., 2001). However >90% of events were those of 7-day durations or less for all regions in the study (Serreze et al., 2001). Such results indicate that the 4-day lag used in our analysis was within the range of duration for large snowfall events in the Sierra Nevada. Variation in surface optical and thermal conditions at temporal resolutions on the order or greater than a 4-day lag due to the influence of intermittent cloud cover associated with synoptic scale systems, could impact the observed variability within the simulated NSMI feature space as well. Reducing the temporal resolution through further aggregation may improve the signal-to-noise ratio and improve the strength of coupling between surface radiative characteristics and snow pack discharge. Aggregations beyond 3-4 days may average out the component of the melt signal correlated to occurrences of melt release (personal communication, Jeff Dozier). Additional work will be done to determine the optimal temporal resolution required to maximum surface signal and internal melt signal correlation.

6. SUMMARY AND RECOMMENDATIONS

Potential for remote sensors to monitor mountain snow pack evolution through use of the surface optical and thermal properties is heavily contingent on the enduring relationship between surface characteristics and the melt production process within the snow pack throughout the ablation season. This paper has explored this process by combining information from two approaches that separately provide high resolution information along one dimension (spectral, stratigraphic, or temporal) at a cost to others. The power of this analysis is in how these two approaches can be synthesized to represent the entire ablation season and enhance our understanding of phases in coupling and decoupling of snow surface optical/thermal properties with the internal melt generation process. Results indicate phases of strong coupling with a 1-4 day lag in surface optical/thermal changes to melt discharge. New snowfall events tend to decouple the surface from the snow pack propensity for melt release. Phases of decoupling exhibited within the MMCS-simulated NSMI were regulated by the temporal resolution (aggregation interval) specified to construct the feature space. Adjustments to the aggregation interval allow the NSMI feature space to be calibrated to various components of surface radiative variability. Greater aggregation (coarser temporal optical and thermal resolution) will tend to shift NSMI feature space correlation to melt discharge from specific snowfall events to inter-seasonal trends. More work is required to determine optimal selection of temporal resolution for NSMI construction. Our work demonstrates that surface optical changes can be used to track changes in the snow pack, supported by significant structural changes in the pack (i.e. melt flow tubes) during melt flow. Results from this work support the development of a satellite derived NSMI and

provides confidence that this approach would be viable to track the evolving spring time snow pack. Application of the NSMI algorithm to data derived from historical moderate resolution satellite systems as well as current and future systems would facilitate improvements in tracking the spatial distribution of mountain snow melt release.

Snowmelt maps derived from this approach could be used to improve spatially distributed snowmelt model performance in addition to better management of water resources through higher resolution information about basin-scale water release timing. However, several constraints must be considered including the influence of persistent cloud cover on the number of scenes available for melt mapping, optimal temporal resolution to reduce the affects of spatially coherent, multi-day precipitation events (snowfall), and heterogeneous terrain.

Acknowledgments. This study was supported by NASA under the Earth System Science Fellowship (ESS) Grant NGT5. Thanks to Dr. Kurt Thome for use of the portable spectrometer and for data processing support. I would like to extend my gratitude to Dr. Kelly Elder for his support and use of the Fraser Experimental Forest (National Forest Service) as base of operations during my field campaign. Thanks to Dr. Chris Cattrall for support in spectra data processing.

REFERENCES

- Davis, R.E., A.W. Nolin, R. Jordan, J. Dozier. 1993. Towards predicting temporal changes of the spectral signature of snow in visible and near-infrared wavelengths. *Annals of Glaciology.*, Volume 17, pp 143-148.
- Dozier, J. 1989. Spectral signature of alpine snow cover from the Landsat Thematic Mapper. *Remote Sens. Environ.*, 28, 9-22.
- Elder, K., and J. Dozier. 1990. Improving methods for measurement and estimation of snow storage in alpine watersheds, in Hydrology in Mountainous Regions. I- Hydrological Measurements; the Water Cycle (Proceedings of two Lausanne Symposium, August 1990). IAHS Publ. No. 193. 147-156.
- Fukami, H., K. Kojima, and H. Aburakawa. 1985. Extinction and absorption of solar radiation within a snow cover. *Annals of Glaciology*, Vol. 6. 118-122.
- Rango, A.1993. II. Snow hydrology and remote sensing. *Hydrological Processes*, Volume 7, 121-138.
- Rott, H.1987. Remote sensing of snow in Large Scale Effects of Seasonal Snow cover, Proceedings of the Vancouver Symposium, August 1987. IAHS Publ. no. 166.

Marks, D., J. Dozier, R.E. Davis. 1992. 1992. Climate and energy exchange at the snow surface in the alpine region of the sierra Nevada 1. meteorological measurements and monitoring. *Water Resources Research*, Vol. 28, NO 11. 3029-3042.

Oke, T.R. 1987. Boundary layer climates 2nd edition. Routledge.

Serreze, M.C., M.P. Clark, and A. Frei. 2001. Characteristics of large snowfall events in the montane western united states as examined using snowpack telemetry (SNOTel) data. *Water Resources Research*, Volume 37, Number 3, 675-688.

Shook, K., and D.M. Gray. 1997. Snowmelt resulting from advection. *Hydrological Processes*, Vol. 11, 1725-1736.

Winther, J-G., S. Gerland, J.B. Ørbæk, B. Ivanov, A. Blanco, and J. Boike. 1999. Spectral reflectance of melting snow in a high Arctic watershed on Svalbard: some implications for optical satellite remote sensing studies. *Hydrological Processes*, Vol. 13, 2033-2049.

APPENDIX

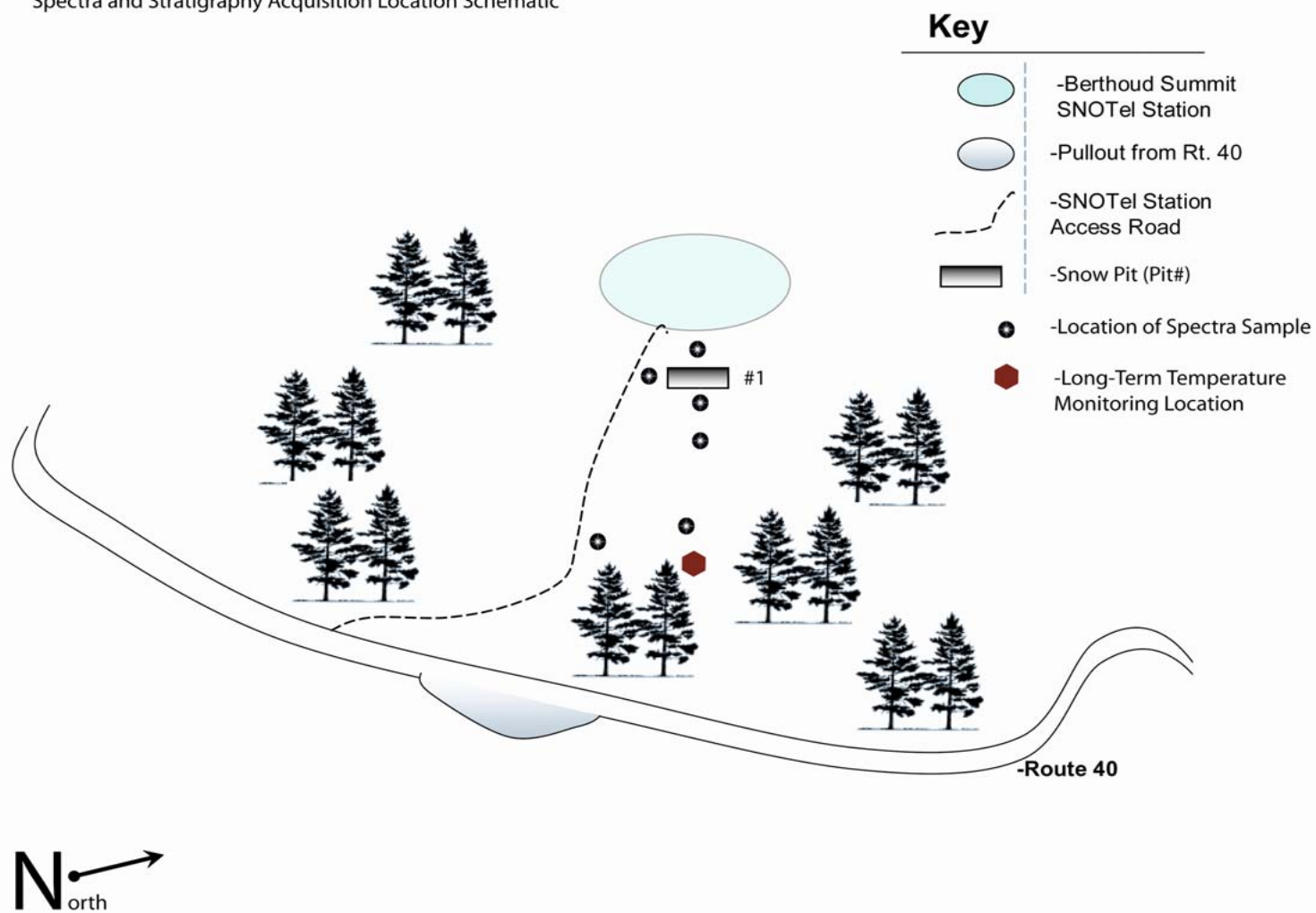
A-Location of ground spectra samples for Sites S1 and S2 for each day.

- These plates depict the location relative of snow pits and spectra collected at both Fraser sites daily. The snow pit locations are persistent for each day (i.e. each pit location acquired on that specific day appears and is depicted in subsequent days). The location of spectra are specific to the particular day.

B-Sites S1 and S2 stratigraphy plates.

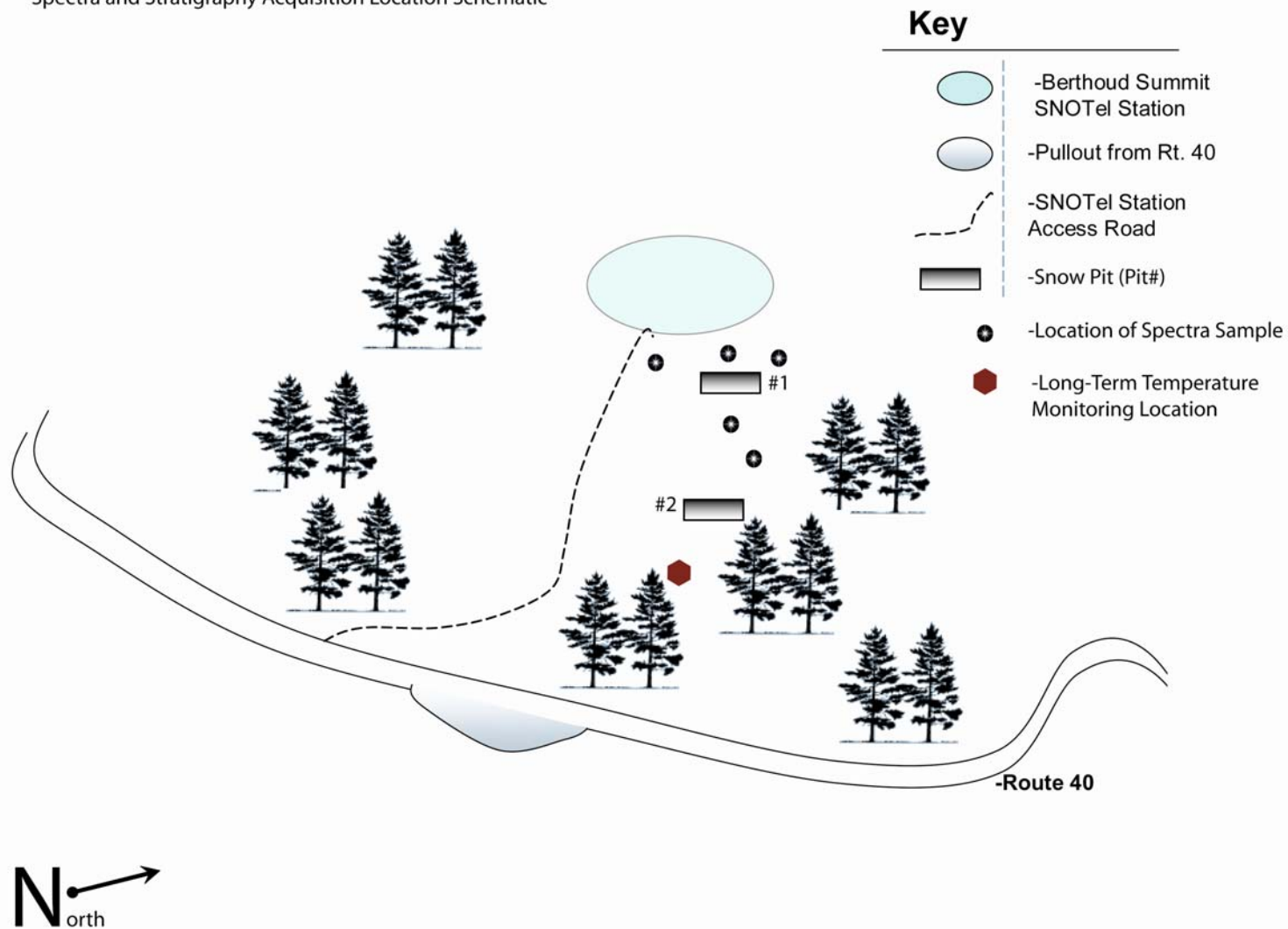
Berthoud Pass (S1): March 22, 2004

Spectra and Stratigraphy Acquisition Location Schematic



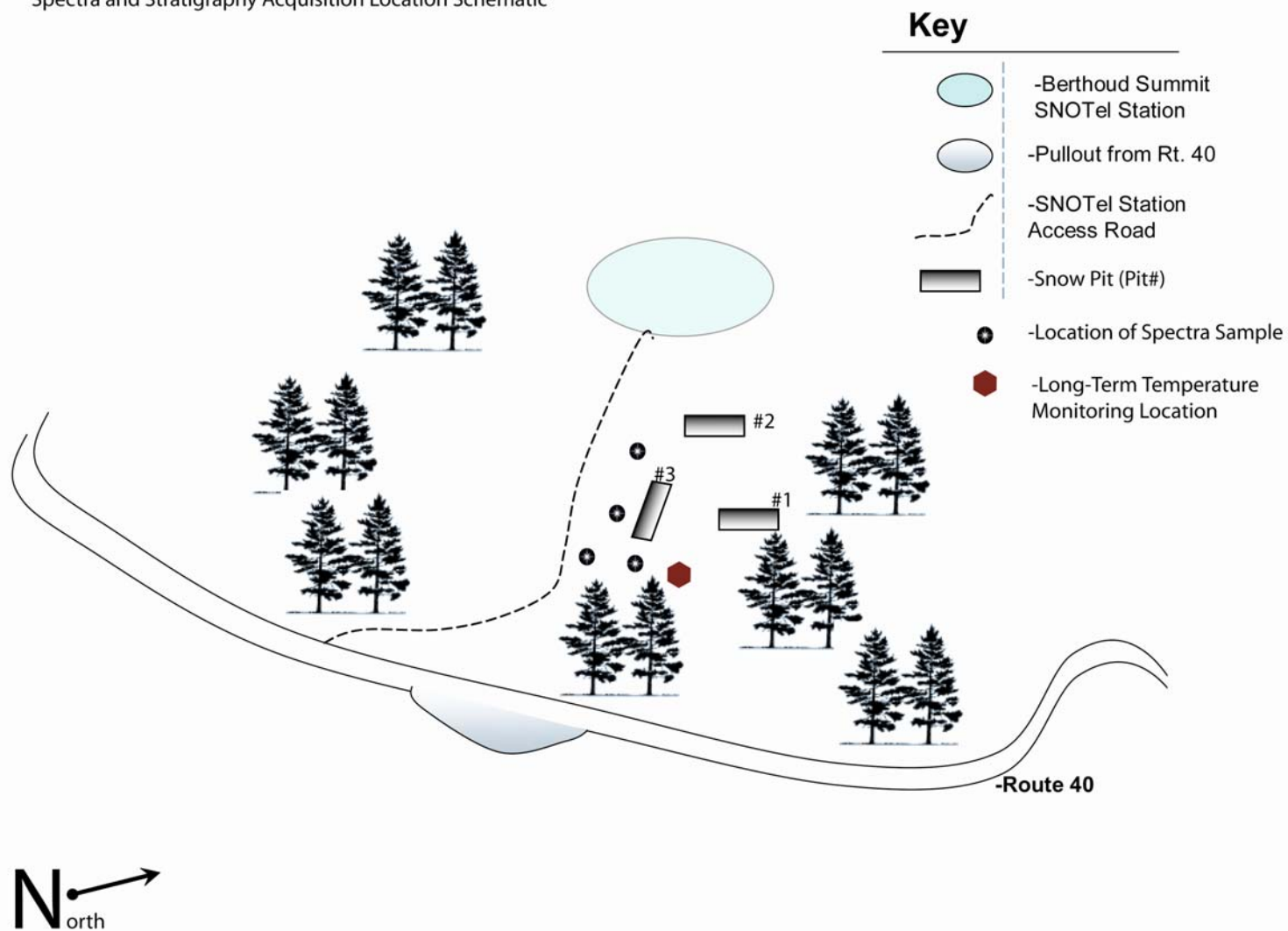
Berthoud Pass (S1): March 23, 2004

Spectra and Stratigraphy Acquisition Location Schematic



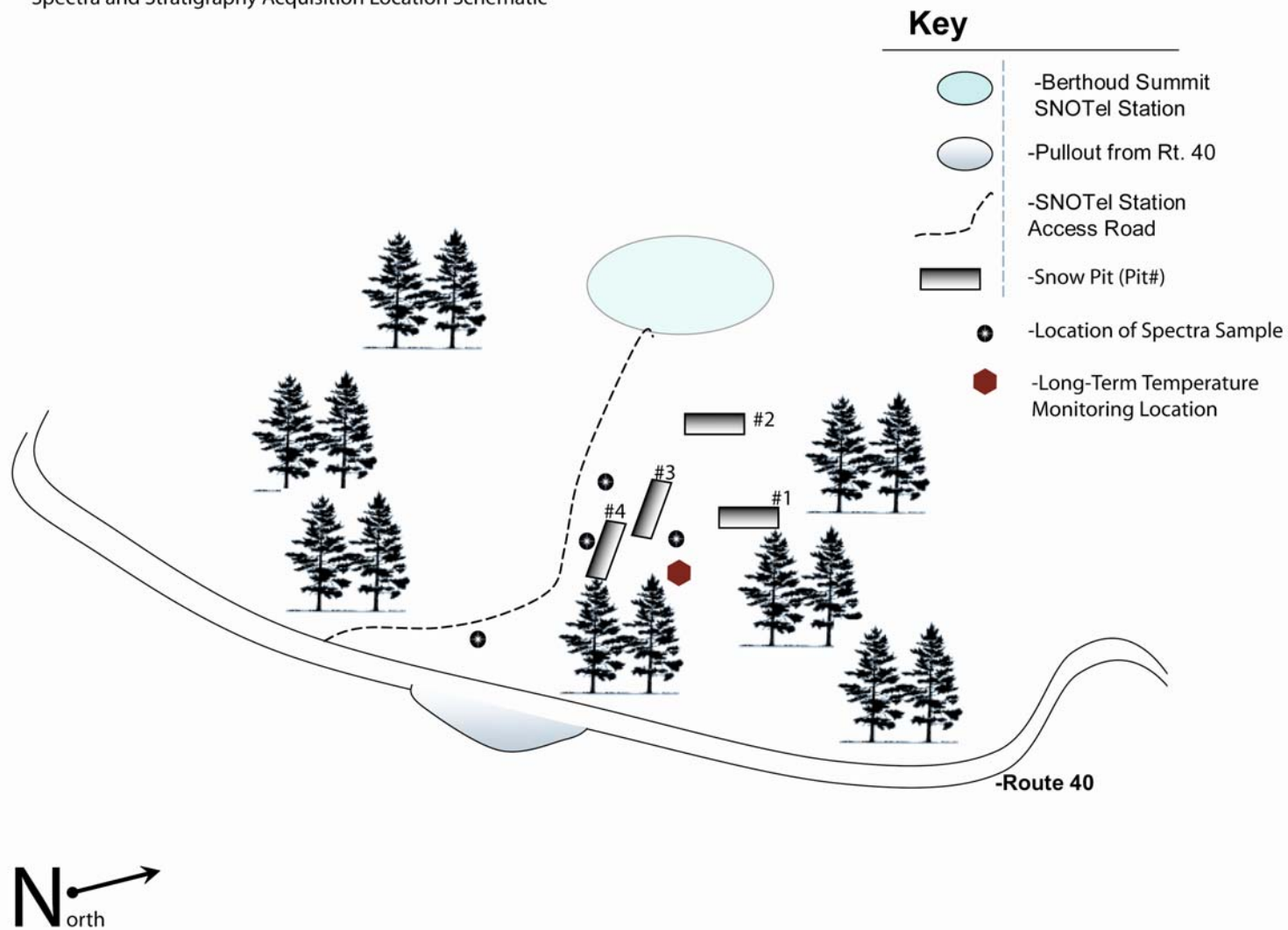
Berthoud Pass (S1): March 25, 2004

Spectra and Stratigraphy Acquisition Location Schematic



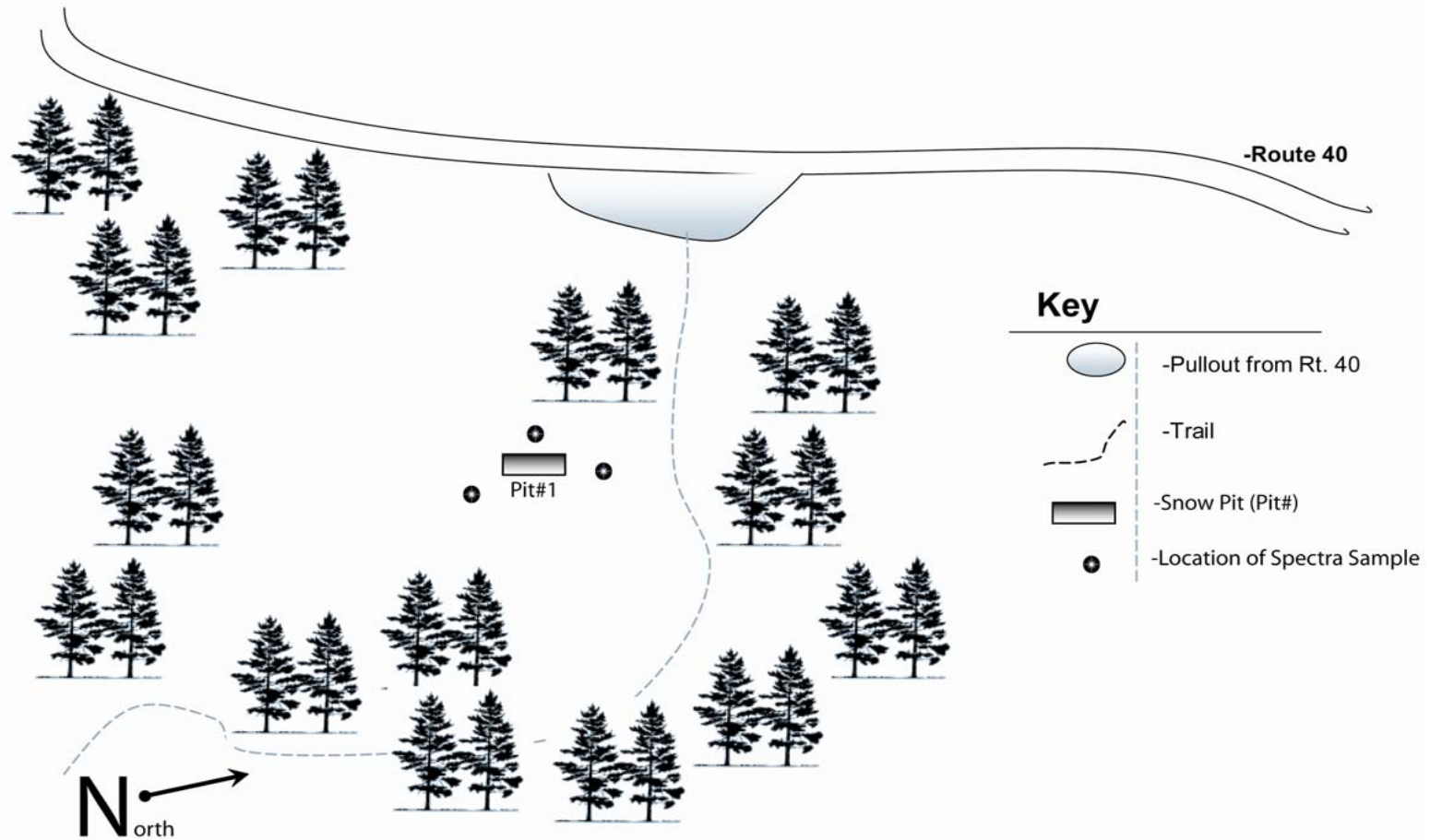
Berthoud Pass (S1): March 26, 2004

Spectra and Stratigraphy Acquisition Location Schematic



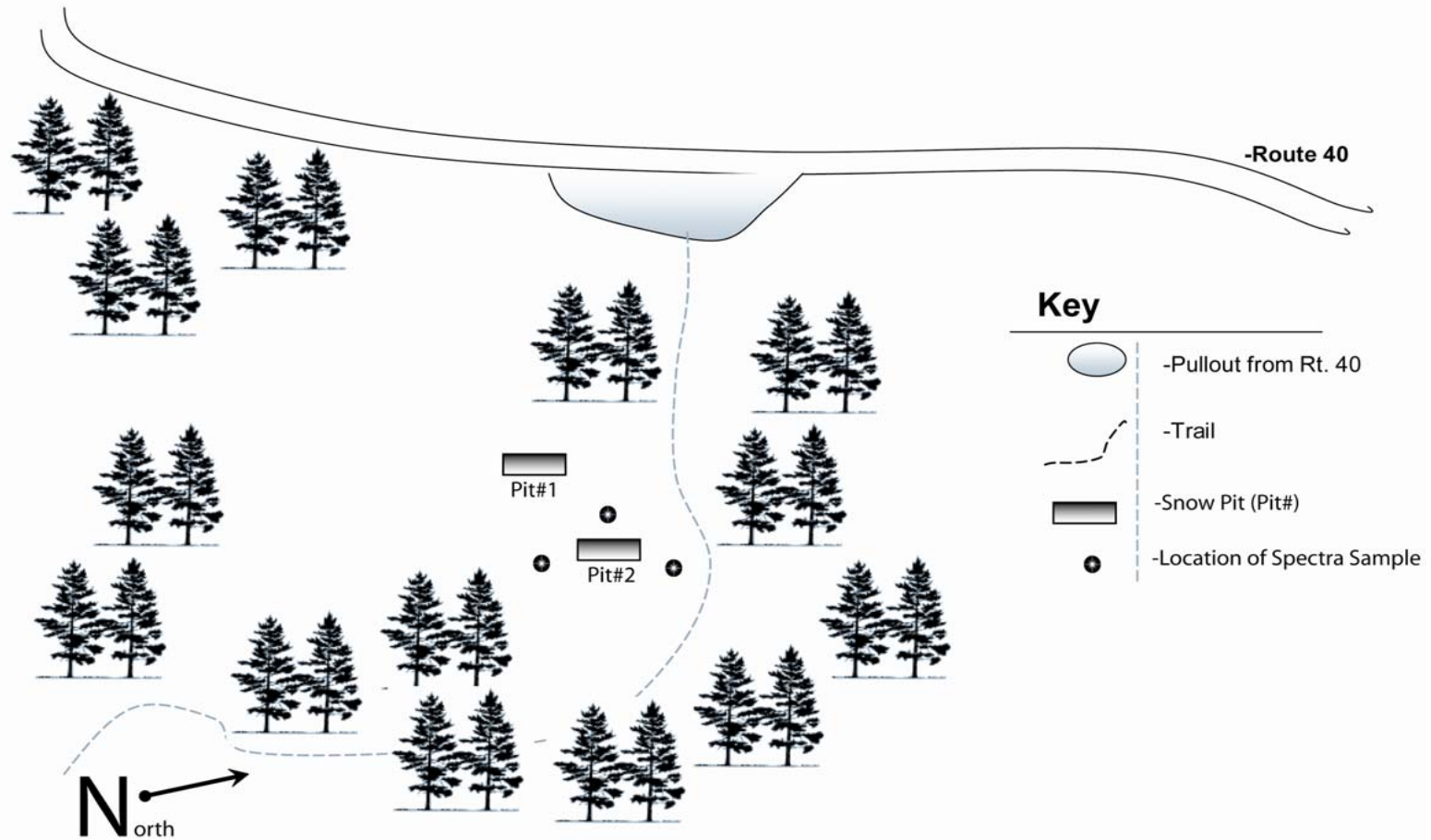
Robber's Roost Trailhead (S2): March 22, 2004

Spectra and Stratigraphy Acquisition Location Schematic



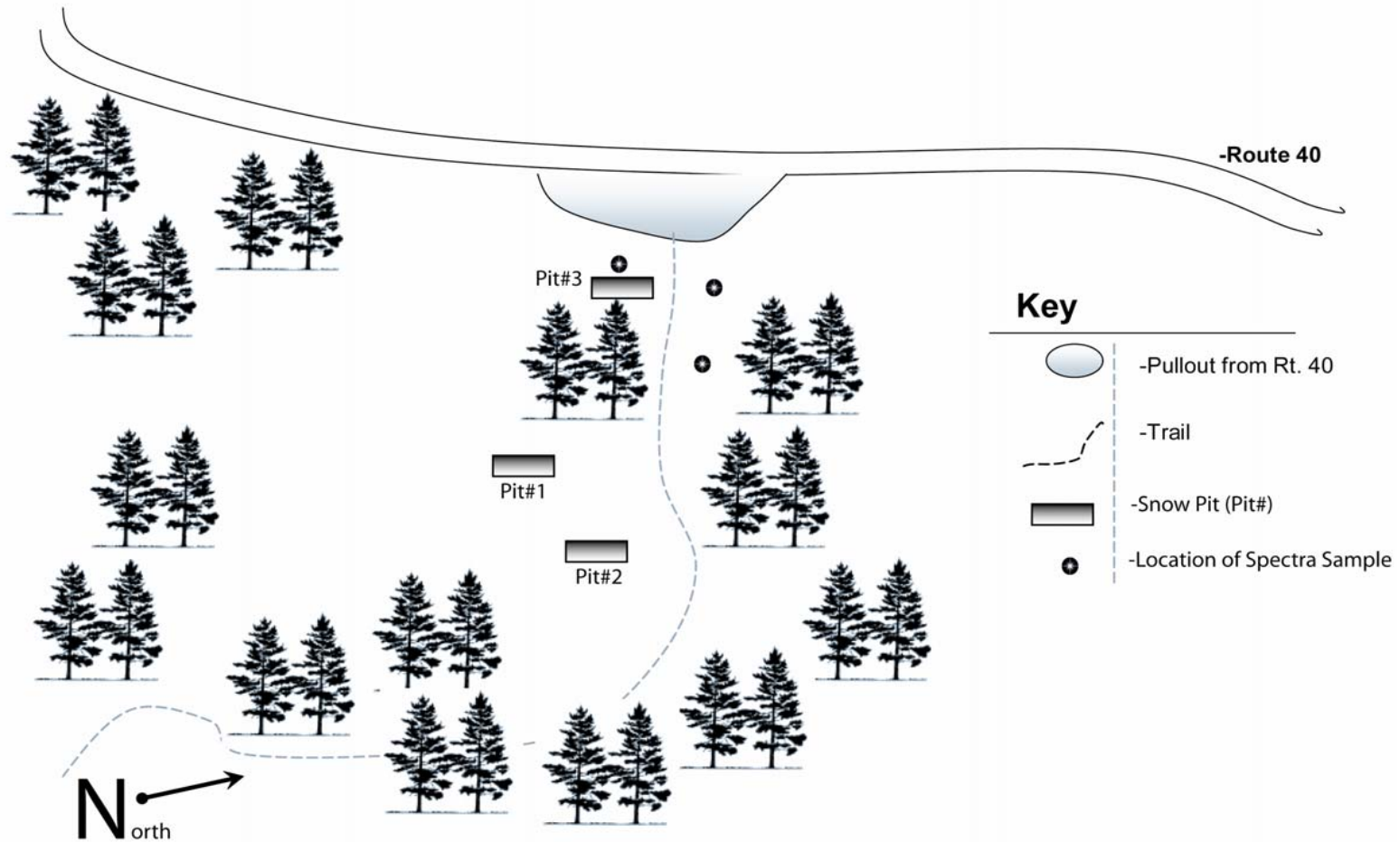
Robber's Roost Trailhead (S2): March 23, 2004

Spectra and Stratigraphy Acquisition Location Schematic



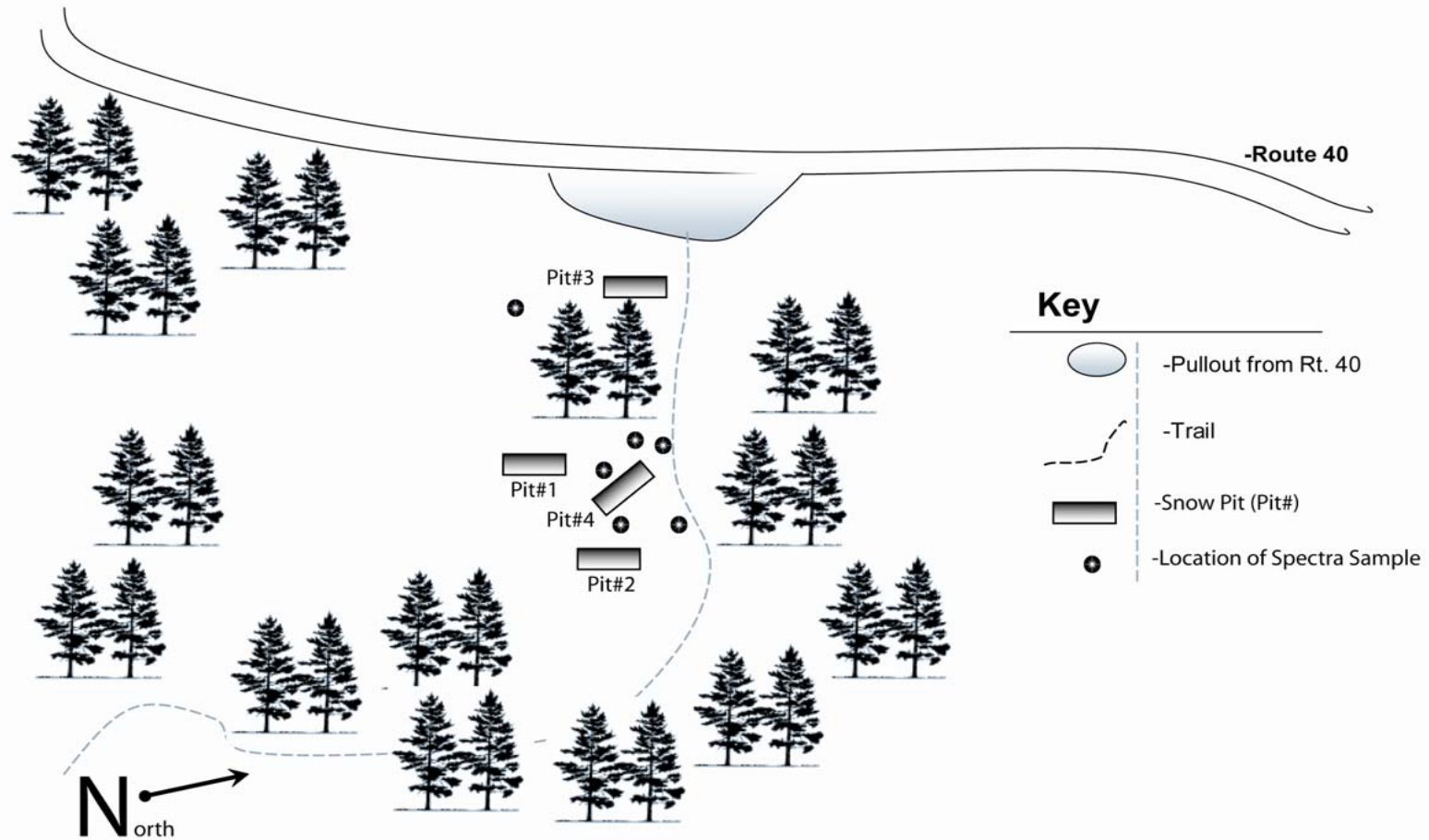
Robber's Roost Trailhead (S2): March 25, 2004

Spectra and Stratigraphy Acquisition Location Schematic



Robber's Roost Trailhead (S2): March 26, 2004

Spectra and Stratigraphy Acquisition Location Schematic



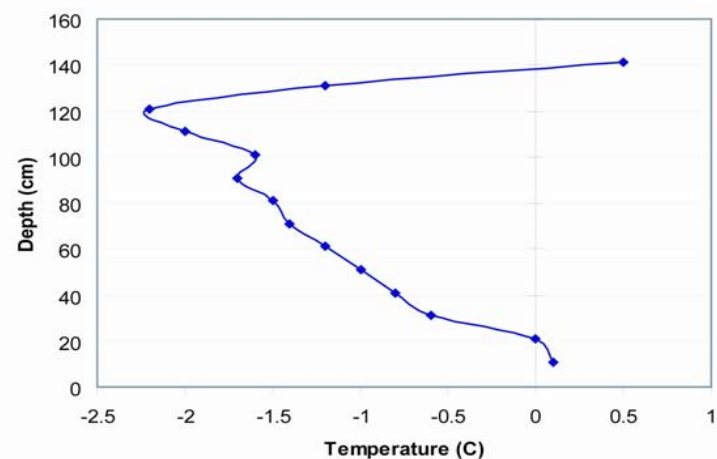
Appendix B

Berthoud Pass (S1): March 22, 2004

Depth Range (cm)	Stratigraphy	Description
141-140	Surface-melt/freeze crust	
140		
137	Ice Crust (1cm)-loose	
131	Ice Crust (2cm)-loose	
124	Ice Crust (1cm)-loose	
121	Ice Crust (1cm)-loose	
119	Ice Crust (1cm)	Round Sintered Clusters
114	Ice Crust (1cm)-loose	Densely Packed (~0.1-0.3mm)
104	Ice Crust (1cm)-loose	
89		
87	Ice Crust (1cm)-loose	
82	Ice Crust (1cm)-loose	
		Facet Depth Hoar Loosely Consolidated Clusters (~1-2mm)
61	Ice Crust (2cm)-loose	
58	Ice Crust (2cm)-loose	
42	Ice Crust (2cm)-loose	
40	Ice Crust (2cm)-loose	
30		
20	Ice Crust (2cm)-loose	Smaller Hoar fragments, some sintering, very unconsolidated loose depth hoar
	Ice Crust	(~0.5-1mm)
0		

Time: 12:00 noon
Location: Berthoud Pass-SNOTEL Site
Surface Temperature(C): 0.1
Maximum Depth (cm): 141
Weather: clear, sunny

Surface Wetness: very wet
Surface Grain Size: large grain clusters approx 1-1.5mm, well sintered

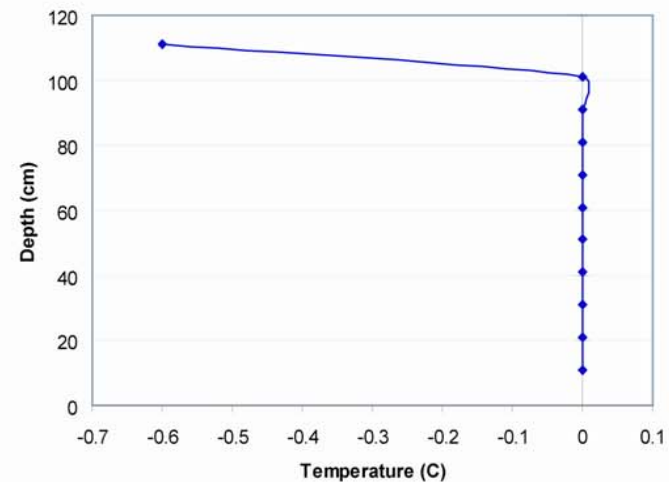


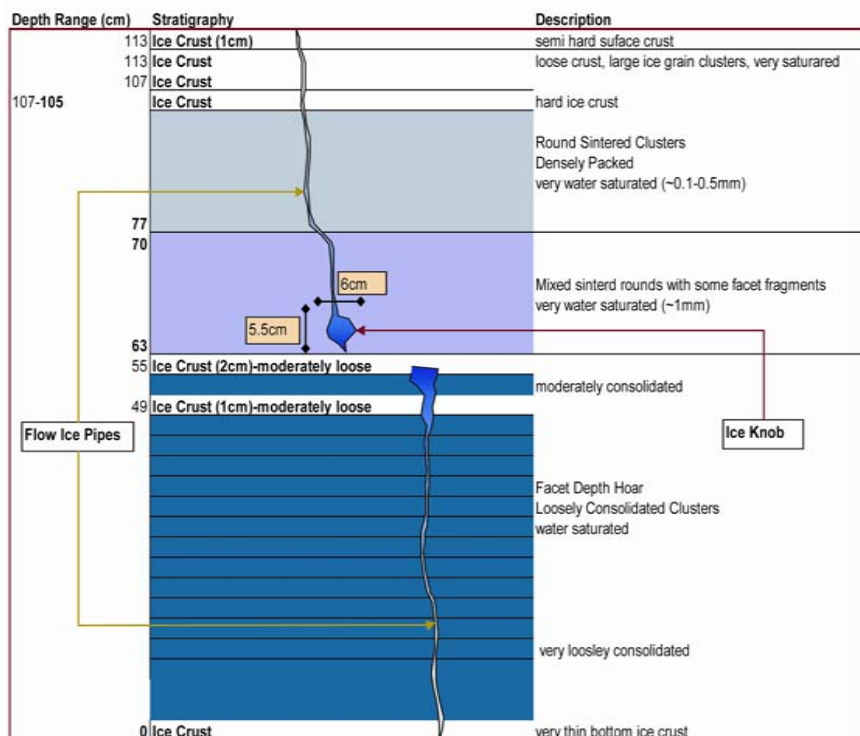
Berthoud Pass (S1): March 23, 2004

Depth Range (cm)	Stratigraphy	Description
111-101	111 NewSnow-early/Larde Grains Later in day Ice Crust just below new snow	
	101 Ice Crust (1cm)	101- Round Sintered Clusters Densely Packed (~0.1-0.3mm)
		91- Round Sintered Clusters Densely Packed (~0.1-0.2mm)
73-70	Ice Crust	
		Mixed faceted and rounds
60		moderately consolidated
		Facet Depth Hoar Loosely Consolidated Clusters
0		very loosley consolidated

Time: 9:00am
 Location: Berthoud Pass-SNOTEL Site
 Surface Temperature(C): -1.5
 Maximum Depth (cm): 111
 Weather: partly cloudy, snow flurries intermitten early during the day

Surface Wetness: moist
 Surface Grain Size: new snow early, but melted later displaying very large grains ~1.5-2mm

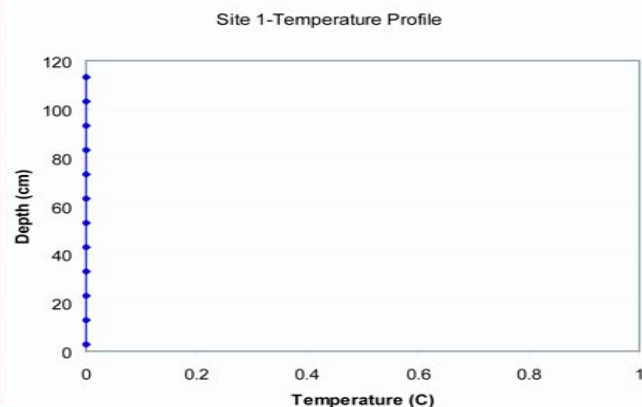




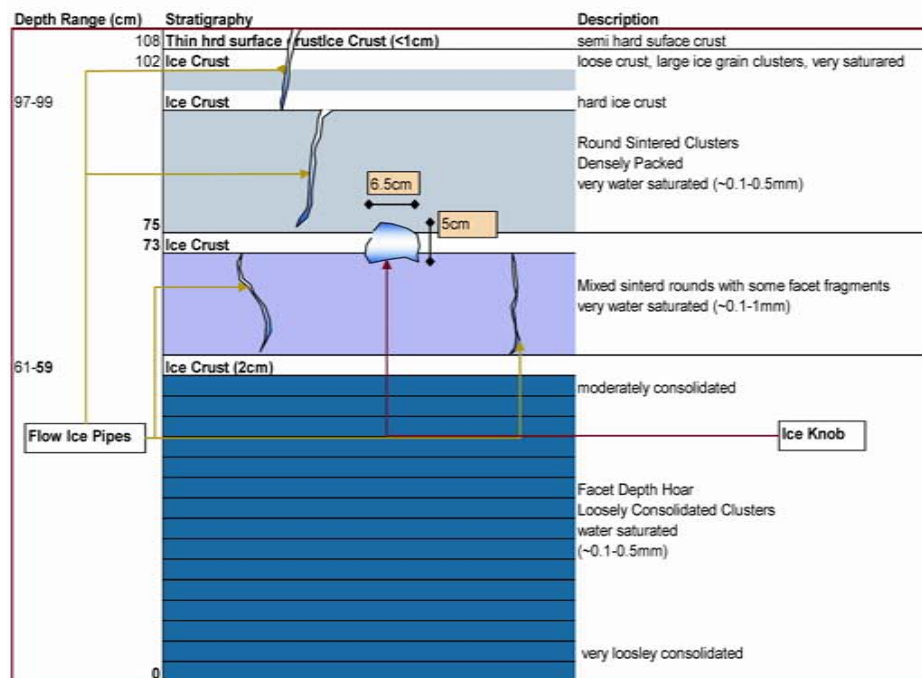
Berthoud Pass (S1): March 25, 2004

Time: 4:00pm
Location: Berthoud Pass-SNOTEL Site
Surface Temperature(C): 0.3
Maximum Depth (cm): 113
Weather: some clouds, mostly clear

Surface Wetness: very wet, saturated
Surface Grain Size: sintered clusters, saturated, with grains clusters ~1-2mm

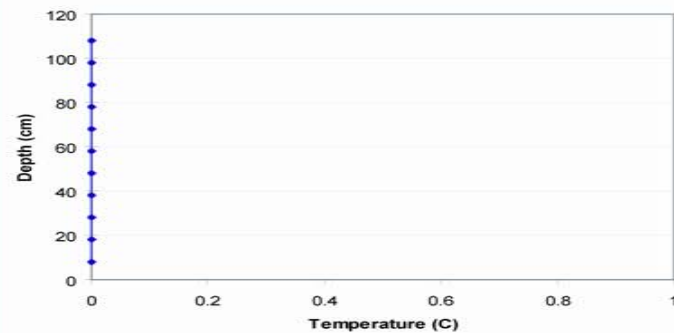


Berthoud Pass (S1): March 26, 2004



Time: 3:20pm
Location: Berthoud Pass-SNOTEL Site
Surface Temperature(C): 0.3
Maximum Depth (cm): 108
Weather: overcast, thin clouds

Surface Wetness: very wet, saturated
Surface Grain Size: sintered clusters, saturated, with grains clusters ~1.5-2mm



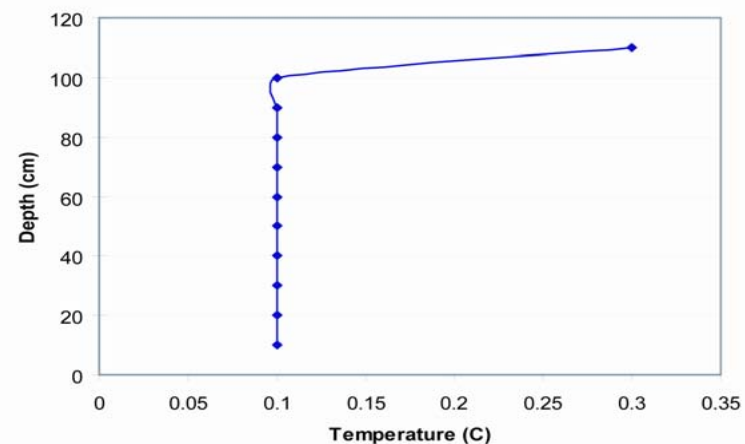
Berthoud Pass (S2): March 22, 2004

Depth Range (cm)	Stratigraphy	Description
110-100	Surface-melt/freeze crust	
100		
82	Ice Crust (1cm)	Round Sintered Clusters
80	Ice Crust (1cm)	Densely Packed (~0.1-0.2mm)
76-73	Ice Crust	
50		Mixed rounds and hoar facets sintered cluster rounds higher in the column (~1-1.5mm)
		Depth Hoar facets, with some sintering very unconsolidated loose depth hoar (~0.5-1mm)
		very loosely consolidated
0		

Time: 3:30pm
Location: Robbers Roost Pullout-Site2
Surface Temperature(C): 0.1
Maximum Depth (cm): 110
Weather: clear, sunny

Surface Wetness: wet-very wet
Surface Grain Size: very large melt clusters, sintered, very hard crust grain clusters approx 2-2.5mm

Site 2-Temperature Profile



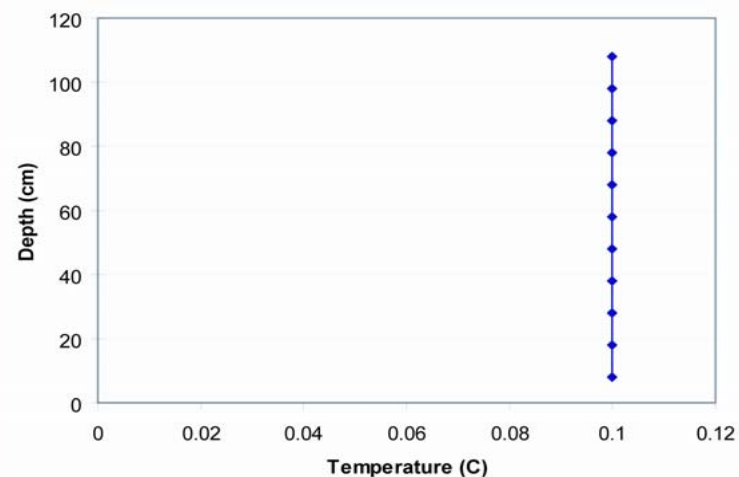
Berthoud Pass (S2): March 25, 2004

Depth Range (cm)	Stratigraphy	Description
105-102	108 Surface-melt/freeze crust	less consolidated, very water saturated and loose
		more consolidated, cryptocrystalline
87-84	92 Ice Crust (1cm)	Densely Packed, slushy and very water saturated (~1-1.5mm)
	81 Ice Crust	
60		dense
		Mixed rounds and hoar facets
		loose, (~1-1.5mm)
25-21		Depth Hoar facets, very wet, water saturated (~1-1.5mm)
	Ice Crust	
		very loosely consolidated semi-sintered facet clusters
	0 Ice Crust	thin bottom ice crust, maybe formed from melt and refreeze?

Time: 1:45pm
Location: Robbers Roost Pullout-Site2
Surface Temperature(C): 0.3
Maximum Depth (cm): 108
Weather: few clouds, mostly clear

Surface Wetness: very wet
Surface Grain Size: very large melt clusters clusters approx 1.5-3mm

Site 2-Temperature Profile



Berthoud Pass (S2): March 26, 2004

Depth Range (cm)	Stratigraphy	Description
94	Surface-melt/freeze crust	less consolidated, very water saturated and loose
84		more consolidated, cryptocrystalline
73	Ice crust-loose (1cm)	Round Sintered Clusters Densely Packed, slushy and very water saturated (~1-2mm)
43		
34		Mixed rounds and hoar facets loose, (~1-1.5mm)
		Depth Hoar facets, very wet, water saturated (~1-1.5mm)
14	Ice Crust (1cm)-loose	very loosely consolidated semi-sintered facet clusters
0		

Time: 1:15pm
 Location: Robbers Roost Pullout-Site2
 Surface Temperature(C): 0.3
 Maximum Depth (cm): 94
 Weather: mostly clear, thin cirrus

Surface Wetness: very wet/saturated
 Surface Grain Size: very large melt clusters clusters approx 1.5-2.5mm

Site 2-Temperature Profile

